The Pennsylvania State University
The Graduate School

DESIGN AND ANALYSIS OF A MAGNETIC LEVITATION SYSTEM FOR CONTROL SYSTEMS COURSES

A Thesis in
Electrical Engineering
by
Jason R. Dalenberg

Submitted in Partial Fulfillment
of the Requirements
for the Degree of

Master of Science

December 2011

The thesis of Jason R. Dalenberg was reviewed and approved* by the following:

Jeffrey L. Schiano
Associate Professor of Electrical Engineering
Thesis Advisor

Ji-Woong Lee
Assistant Professor of Electrical Engineering

Kultegin Aydin
Professor of Electrical Engineering
Department Head of Electrical Engineering

*Signatures are on file in the Graduate School.

Abstract

The objective of this thesis is to develop a low-cost electromagnetic levitation test bed that can be used to demonstrate concepts of feedback control systems as applied to linearized models of non-linear systems. This test bed is particularly interesting because it can be used to demonstrate both repulsive and attractive levitation. From a control standpoint, these correspond to stable and unstable equilibrium points of a non-linear system. An inexpensive commercial system, using attractive levitation, is analyzed and later compared to the developed test bed as an educational tool. Parametric modeling and system identification techniques are used to determine the linearized models of both systems around an operating point. These models are used in the design of feedback controllers, which are implemented and verified experimentally. Experimental results suggest that heating due to power dissipation in the electromagnet varies the system model over time, resulting in degradation of the transient response characteristics. Overall, the developed electromagnetic levitation test bed proves to be a cost-effective educational tool for both undergraduate and graduate level studies of control systems topics.

Table of Contents

List of Figures

List of Tables

Chapter 1

Magnetic Levitation in Control Systems Education

The objective of this thesis is to develop a low-cost magnetic levitation test bed that can be used to demonstrate concepts of feedback control systems as applied to linearized models of non-linear systems. This test bed is particularly interesting because it can be used to demonstrate both repulsive and attractive levitation. From a control standpoint, these correspond to stable and unstable equilibrium points of a non-linear system. An inexpensive commercial system, using attractive levitation, is analyzed and later compared to the developed test bed as an educational tool. Parametric modeling and system identification techniques are used to determine the linearized models of both systems around an operating point. These models are used in the design of feedback controllers, which are implemented and verified experimentally.

There are many reasons why a control systems laboratory may want to develop its own experimental equipment. As test beds age, they will either need to be repaired or replaced in order for the laboratory to remain effective. While repairing equipment is a possibility, there will come a time when the necessary components become scarce and prohibitively expensive to procure. Alternatively, replacing a laboratory with a full complement of commercial test beds is expensive. A cost effective solution is to develop a test bed that can be assembled with

inexpensive off-the-shelf components and can demonstrate multiple concepts. A laboratory equipped with several different low cost test beds can further help demonstrate unique principles that a single system cannot cover alone.

Chapter 1 describes several magnetic levitation test beds and their subsystems. The general underlying principles are addressed to present the challenges associated with these systems. A survey of magnetic levitation research is used to show relevance and to provide incentive for this thesis. Desirable attributes of control systems test beds are listed and compared to the attributes of the developed test bed. Chapter 1 culminates with a listing of the thesis contributions and organization.

1.1 Magnetic Levitation Test Beds

Magnetic levitation can be categorized as either attractive levitation or repulsive levitation depending on the type of forces being generated [1]. In attractive levitation, the levitated object is drawn towards the electromagnet, whereas the object is driven away from the electromagnet with repulsive levitation. In order to position the levitated mass at a fixed position, the force of electric origin, f^e, is typically balanced by the force of gravity, f_g. A second electromagnet, set diametrically opposite of the primary electromagnet, can be used to aide or hinder the force of electric origin of the primary electromagnet. This thesis focuses on the repulsive and attractive levitation of a magnetic object using a single electromagnet.

Figure 1.1 shows a block diagram of an attractive levitation system, where the levitated mass, M, is ferromagnetic. The force of electric origin, f^e, is proportional to the square of the current through the electromagnet and inversely proportional to the square of the separation distance, y. While this force will help define the separation distance, y, a stable equilibrium point exists only when the force of electric origin, f^e, pulling the mass up is exactly balanced by the force of gravity, f_g, pulling the ball down. By Earnshaw's Theorem [2], this equilibrium state, y_e, is fundamentally unstable. To understand why this system is unstable, imagine a disturbance acting in either direction on the mass at equilibrium. For example, if a disturbance moves the mass towards the electromagnet, the force of electric origin will dominate. The mass will move further towards the electromagnet where the force of electric origin is even stronger.

A fixed optical sensor and light source, located at the equilibrium position, are used to determine the position of the mass, y. A voltage, v_s, is generated by the optical sensor based upon the amount of light that is sensed from the light source. As the mass moves away from the equilibrium position, a proportional change in the sensor output voltage will occur. This system is stabilized by introducing a feedback controller whose input is the sensor voltage output, v_s, and output is the voltage input to the amplifier, u. Finally, a transconductance amplifier is used to provide power to the electromagnet in the form of the current, i_L.

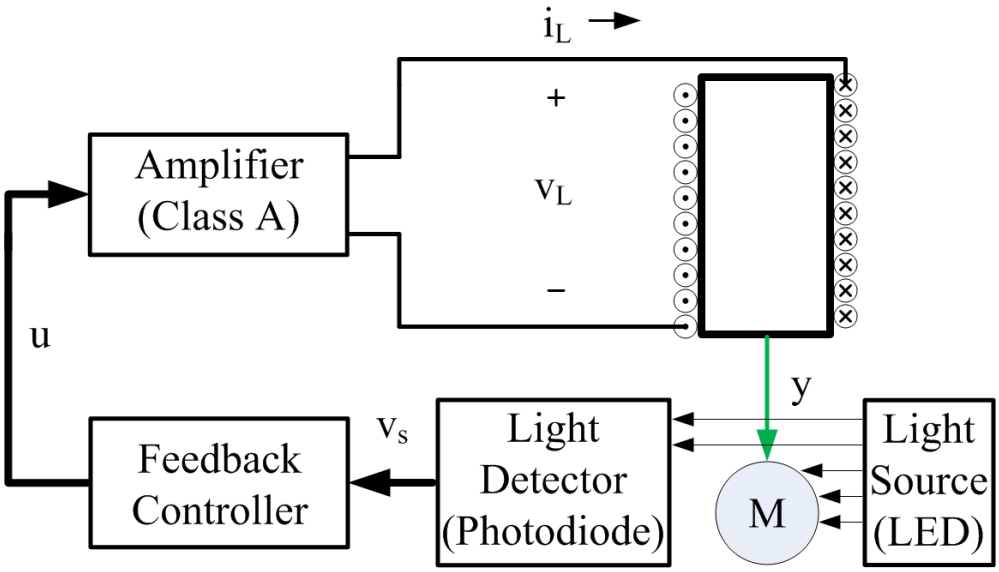

Figure 1.1. Magnetic Levitation Model using Attractive Levitation with a Ferromagnetic Mass

It would be interesting to be able to create a repulsive levitation system because it would exhibit operation at a stable equilibrium point. Unfortunately, a repulsive levitation system cannot be made by simply turning the apparatus in Figure 1.1 upside down. No balance of forces can be reached in this configuration, as the force of electric origin acting on a ferromagnetic mass will always act towards the the electromagnet. An attractive levitation system can be transformed into a repulsive levitation system if it is designed similarly to the system detailed in Figure 1.2.

Figure 1.2 shows a diagram of an attractive levitation system, where the levitated mass, M, is a permanent magnet. The force of electric origin is proportional to the current through the electromagnet and inversely proportional to the square of the separation distance, y. Therefore, changing the direction of the current through the electromagnet, i_L will allow a change in the direction of the force of electric origin, f^e. Figure 1.3 demonstrates a repulsive

levitation system by turning over the apparatus in Figure 1.2 and changing the direction of the current through the electromagnet. This allows a stable equilibrium position, y_e, to reached by balancing the force of electric origin, f^e with the force of gravity, f_g.

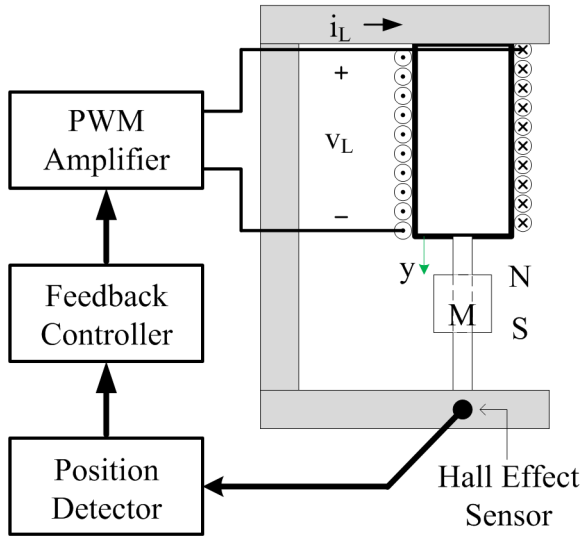

Figure 1.2. Magnetic Levitation Model using Attractive Levitation with a Magnetic Mass

In addition to levitating a permanent magnet, the system detailed in Figures 1.2 and 1.3 also features a pulse width modulation (PWM) amplifier scheme, a Hall effect sensor, and a guide rail for the mass. The first three modifications were made based on an attractive levitation system designed in 2003 by Guy Marsden [3]. These features provide a superior

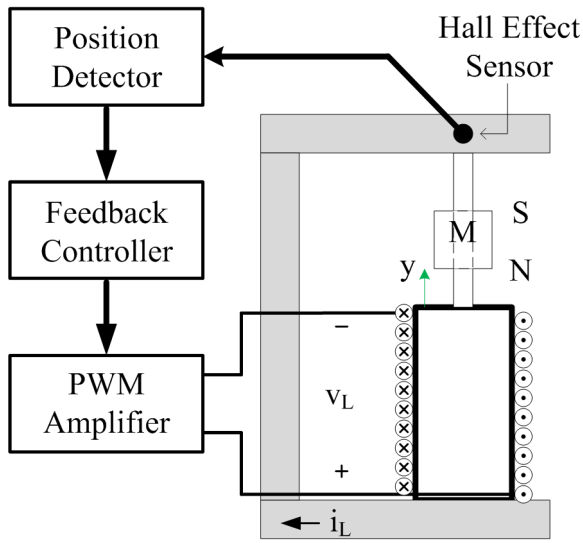

Figure 1.3. Magnetic Levitation Model using Repulsive Levitation with a Magnetic Mass

performance as compared to the components used in the system in Figure 1.1.

Using a magnetic mass not only allows the system to demonstrate repulsive levitation, but also reduces the magnitude of the current that is needed to levitate the mass, thus decreasing power dissipation as compared to what is necessary to levitate a ferromagnetic mass of the same weight. Conversely, given the same maximum current and electromagnet, the system with the magnetic mass would be able control a larger range of equilibrium positions. Compared to the system in Figure 1.1, which uses a class A amplifier, a PWM amplifier scheme reduces the power dissipated in the electromagnet by increasing the efficiency of the amplifier.

The optical sensor and light source used in the attractive levitation system shown in Figure 1.1 is fixed at a particular equilibrium position, limiting its range of equilibrium positions. A Hall effect sensor is used to sense the change in the magnetic field due to a change in position of the magnetic mass, therefore the equilibrium position is not limited to the sensors location. This results in the system in Figures 1.2 and 1.3 having a much larger dynamic range. The guide rail is used to restrict motion to the y-axis and to keep the mass from rotating during experimentation. The guide rail also conveniently stores the electromagnet between experiments.

1.2 Survey of Magnetic Levitation Research

Magnetic levitation technology has been researched for well over a hundred years. The first U.S. patent for a Maglev system was awarded to Emile Bachelet in 1912 [4]. Bachelet's working model was demonstrated in London in 1914 where notables such as Winston Churchill were present [5]. Researchers such as Hermann Kemper in the 1930's and Prof. Eric Laithwaite and Prof. Jayawant in the 1970's have provided many advances in this field. Figure 1.4 shows a test vehicle and track developed by the University of Sussex in the 1970's. Though many test tracks have been created over the last 30 years, there is only one operating commercial track located in Shanghai, China [6].

While magnetic levitation has been nearly synonymous with Maglev systems, there are many other applications besides mass transportation. Magnetic bearings are devices which allow a rotating shaft to be magnetically supported. The primary benefit to traditional

bearings is that the system becomes nearly frictionless. Controls systems are needed to regulate the electromagnets in the bearing in order to dampen the mechanical vibrations of the shaft and to keep the shaft from touching the bearing walls. Magnetic bearings have been primarily relegated to high speed and cryogenic applications although advances in technology are allowing these devices to show up in other applications such as flywheels and blood pumps [7, 8].

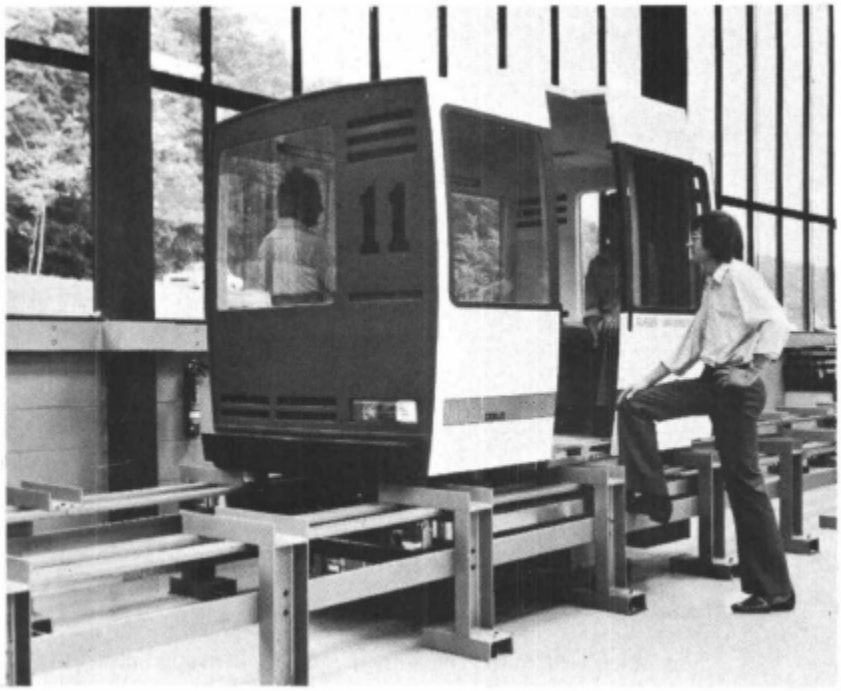

Figure 1.4. 1 Ton Magnetically Suspended Vehicle [9]

Magnetic suspension has also been extensively used in aerodynamic modeling in wind tunnels. Active magnetic control is used to control the degrees-of-freedom (DOF) of a model in test [10]. Active suspension techniques have also been used in 6-DOF alignment systems for lithography systems and injection molded parts systems [11, 12]. Figure 1.5 details the exploded view of eight sets of electromagnetic actuators used in a 6-DOF positioning system.

There have been many papers written about magnetic levitation systems detailing methods of control and applications of this technology. The majority of these papers deal with suspension of ferromagnetic or mixed ferromagnetic-magnetic masses. Of note, Jayawant and Hurley have written a number of papers dealing with attractive levitation of ferromagnetic masses [1, 9, 13, 14, 15, 16]. The clear minority of these papers deal with repulsion of

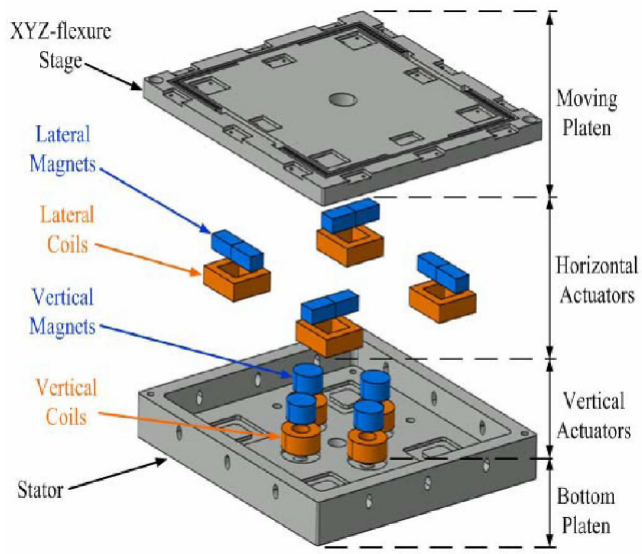

Figure 1.5. Exploded View of a 6-DOF Positioning System [12]

magnetic masses. Tsui in 1972 and Berkelman in 2008 and 2010 considered repulsion systems [17, 18, 19].

A number of educational publications on magnetic levitation have been written. Wong in 1986 and Watkins in 2003 both have written papers on control of magnetic levitation systems for undergraduate studies [20, 21]. Though both use attractive levitation with a ferromagnetic mass, Wong uses a optical sensor while Watkins uses an inductive sensor. In 2004, Lilienkamp and Lundberg both publish papers detailing a magnetic levitation lab module at MIT which was based on the 2003 design by Guy Marsden [3, 22, 23].

One impetus for this thesis was that a detailed system analysis was missing from both Lilienkamp's and Lundberg's papers. It was initially proposed to use Marsden's design as a laboratory test bed but some inconsistencies were noticed in the system. The mass frequently moved out of plane, skewing the Hall effect sensors output, causing the system to become unstable. Finding an appropriate mass for levitation was also determined to be difficult. An equilibrium point could be reached, but small perturbations frequently caused the mass to oscillate uncontrollably.

1.3 Thesis Contributions and Organization

Balchen states that when buying or developing a test bed, ten requirements should be taken into account [24].

(i) The process and the controls under study must reflect an important problem in practical life.

(ii) The experiment must demonstrate an important theoretical result.

(iii) The apparatus must be realistic even if it is simplified relative to practical life.

(iv) The bandwidth of the control process must not be so high that the student finds it unrealistic and not so low that the student finds it boring.

(v) The student must be able to introduce himself to the problem, start up the process, and complete all experiments within a reasonable amount of time.

(vi) The process must give a visual sensation.

(vii) The process must give an acoustic sensation.

(viii) The process must be non-hazardous.

(ix) The apparatus must be inexpensive to manufacture.

(x) The experiment must not require expensive raw materials.

Item (i) addresses the need for the process and controls to have some practical relevance to a control systems engineer. Clear examples of uses of the process and controls will also help engage the student. In Section 1.2, magnetic levitation was shown to be used in many essential industrial devices and applications. Future technological advances will provide even more opportunities for the use of magnetic levitation control. Even if not encountered in industry, hands-on experience with a non-linear system can provide insight into other controls problems. For example, the black box model identified for the test bed developed in this thesis includes a non-minimum phase zero. This test bed can provide fruitful insight as many test beds do not have non-minimum phase zeros.

Item (ii) maintains that the experiment must demonstrate important theoretical results. Control systems concepts such as system linearization, stability conditions, time-domain characteristics, and response trade-offs can be investigated. If a model of the system is given, a course in classic control topics can demonstrate root locus techniques through the design of a feedback controller. A digital control systems course can use this test bed to showcase discrete design techniques and effects of discretization. A graduate course in control systems can use this test bed to demonstrate modern control techniques such as non-linear or adaptive control as well as a variety of system identification techniques.

Item (iii) warns the test bed developer that over simplification of the apparatus will reduce the effectiveness of the experiment or mislead the student about the nature of the process and controls under study. The test bed developed in this thesis is simplified, such that it is restricted to movement along the y-axis normal to the electromagnet. While many real life applications do not have this restriction, the fundamental physics does not change. Therefore, the effectiveness of studying the process and controls of magnetic levitation will not be diminished when using this test bed.

Item (iv) states that the time frame in which the control process is being studied must be reasonable. The difficulty of each experiment can be tailored to the experience level of the student and should be able to provide a reasonable challenge. While full analysis of this system would be a rigorous exercise for the student, theoretical knowledge of the system can be given to the student prior to the laboratory exercise. Sub-dividing the full experiment into multiple sessions will allow several reasonable goals to be accomplished, each in a modest time span.

Items (vi-vii) addresses the need for visual and acoustic sensations in order to engage the student in the experiment. Visually, the mass' position can be controlled through a moderate dynamic range. Acoustically, noise is sometimes created between the mass and casing when it is impelled to either extreme of its range. The electromagnet can also generate a moderate buzzing sound depending on the frequency and duty cycle being commanded.

Item (viii) reminds the test bed developer to remove any source of serious injury in the apparatus. Besides having the traditional hazards associated with electrical devices, the electromagnet can heat to an uncomfortable temperature and the mass can potentially pinch a finger. With reasonable precautions, this system should be considered non-hazardous to

the operator.

Lastly, items (iv-v) deal with the expense of developing the system, its operation, and upkeep. While the development of this test bed was more expensive than the low end commercial system analysed in chapter 2, it is much less expensive to develop than to buy high end systems. As the developed system does not require any expensive raw materials in which to operate, only minor upkeep expenses are expected.

This thesis contributes the following:

1. Development of an inexpensive magnetic levitation test bed for use in a control systems laboratory.
2. Parametric modeling and system identification of a small-signal linearized model of both the stable and unstable equilibrium states.
3. Controller designs for position control of the mass for both equilibrium states.

The thesis is organized as follows. In Chapter 2, a generic attractive levitation system using optical sensing is described. An inexpensive commercially available optical-sensing system is modeled using first principles. This model is compared to an identified state-space model, determined using closed-loop system identification and model reduction techniques. Verification of the identified model is substantiated through controller design and experimentation.

Chapter 3 introduces the design objectives and design of a magnetic levitation test-bed using Hall effect sensing. First, a magnetic levitation system designed by Marsden[3], which uses Hall effect sensing, is discussed as a basis for the design presented in this thesis. The design objectives for this system are presented prior to a discussion of the challenges, constraints, and trade-offs to using Hall effect sensing. Afterwards, the remaining electrical and mechanical design choices are detailed. Chapter 3 concludes with the experimental measurements necessary to implement position sensing, current sensing, and equilibrium point determination.

Chapter 4 analyzes the developed system model for the Hall effect sensing system in its stable equilibrium state. Repulsive levitation of a permanent magnet, held stable in the x-y plane, is shown to be open-loop stable. Parametric open-loop identification is performed

around an operating point, showing the presence of a non-minimum phase zero. Finally, a controller is developed using complementary root locus techniques for use in a position regulation scheme that achieves zero steady-state error.

Chapter 5 analyzes the same system in its unstable equilibrium state. Attractive levitation of a permanent magnet held stable in the x-y plane is shown to be open-loop unstable. A phase-lead controller is used provide basic closed-loop stability. Closed-loop system identification is then performed around an operating point. A re-designed controller is used to show that there are design trade-offs between steady-state accuracy, overshoot, rise-time, and settling-time.

Chapter 6 revisits the trade-offs between test-bed system complexity and cost as well as the trade-offs between closed-loop response characteristics. The Appendix contains sample MATLAB code used for data collection, system identification, and controller designs.

Chapter 2

Attractive Levitation using Optical Sensing

Chapter 2 develops the general dynamic and linearized models of a magnetic levitation system using attractive levitation and optical sensing of a ferromagnetic mass. These models are used in the analysis and control of a commercially available magnetic levitation system. Section 2.1 introduces an inexpensive levitation kit and details modifications necessary for practical use in a control systems laboratory. Section 2.2 discusses a conceptual model based on the commercial system. A dynamic model is developed and linearized around an operating point. In Section 2.3, modeling is performed and compared to results from closed-loop system identification experiments. Section 2.4 details a controller design and experimental results are presented to verify the controller design.

2.1 Commercial System

While laboratory-ready magnetic levitation test-beds can be found for purchase, they are usually expensive. One such system is the Educational Control Products (ECP) MagLev Apparatus [25]. This system ranges from $9,750 for the plant to $12,650 for the full system. If a laboratory is already equipped with a data acquisition (DAQ) system, less costly systems can be found and adapted for use. One such cost-effective alternative is the LNS Technologies

Levitator Kit [26] shown in Figure 2.1. This lab is easily integrated into a control systems laboratory by modifying it such that the sensor output and actuator input are available to the experimenter.

Figure 2.1. Photograph of the LNS Technologies Levitator Kit

The LNS levitation system is represented using the block diagram in Figure 1.1. A schematic showing detail of the system's circuitry is provided in Figure 2.2. An infra-red LED (IRLED) is used as a light source in conjunction with an infra-red photo-diode (IRDET) to determine the position of a hollow ferromagnetic sphere. IRLED and IRDET are fixed near a desired equilibrium position with the mass levitating between the two. As the position of the mass changes, an increase or decrease in infra-red light will be sensed.

A voltage is created at the emitter of IRDET that is proportional to the amount of IR light that is sensed and to the value of the potentiomater (VR1). If VR1 is adjusted, a change will be made to the equilibrium point and to the gain of the sensor. Adjusting too far in either direction will lead to instabilities in the system. An operational amplifier (U_{1B}) decouples the sensor circuitry (IRDET and VR1) from the control circuit (R_{12}, R_7, and C_4) and provides a small gain to the voltage signal across VR1. The sensor voltage output, v_S, is

located at pin 7 of U_{1B} to eliminate the possibility of loading down the optical sensor circuit.

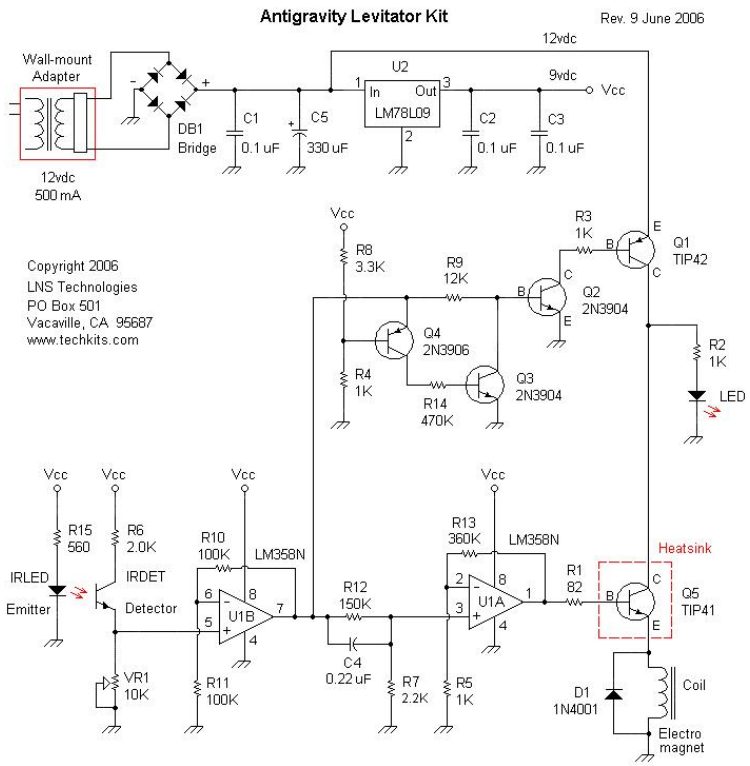

Figure 2.2. LNS Technologies Levitator Kit Circuit Schematic [27]

The output signal of the control circuit v_C, found at pin 3 of the operational amplifier U_{1A}, which can also be considered to be the actuator input u. Transfer function analysis of the analog control circuitry, from v_S to v_C, reveals the circuit to be a phase-lead controller design with transfer function,

$$\frac{v_C}{v_S} = \frac{s + 30.3}{s + 2096}. \tag{2.1}$$

Operational amplifier (U_{1A}) is used to provide a large gain to the actuator input signal, u, and to decouple the control circuit from the class A amplifier (Q_5). Q_1 to Q_4 act together as a safety circuit using the sensor voltage, v_S, as the input. If the ferromagnetic mass falls or is pulled up against the electromagnet, the safety circuit will activate and the current through Q_1 will cut-off, thus cutting-off the current through the electromagnet.

2.1.1 Adaptation for Control Test-bed

While this system has some charm as a demonstration system, it initially has little usefulness in a teaching laboratory. The only exercise that can be accomplished, out of the box, is to tune the sensitivity and equilibrium point of the device. Even so, a variety of experiments can be performed if the the device is modified. First, the circuit path between the controller and actuator is opened, separating the controller output v_C from the actuator input u. Test points are provided to access the sensor v_S, control output v_C, actuator input u, and ground signals. A small circuit board, shown in Figure 2.3 is attached to the rear of the device in order to easily route access to these test points. Circuit modifications to the system are shown in Figure 2.4.

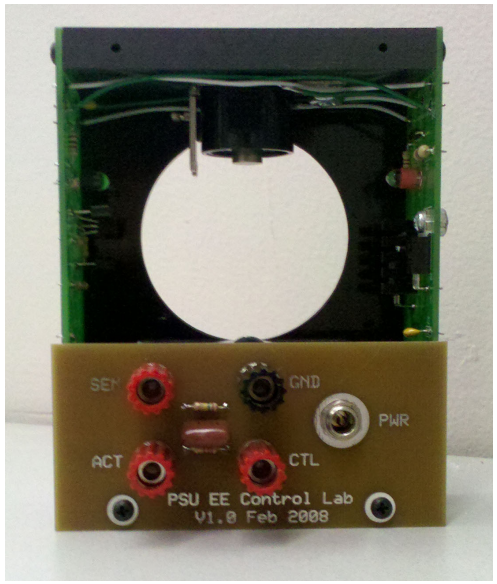

Figure 2.3. Photo of the Modfied LNS Technologies Levitator

These modifications allow many practical exercise to be accomplished. Circuit analysis of the analog control circuitry leads to an s-domain transfer function equivalent representation. A digital controller can be developed based on the analog controller, shown in Equation 2.1, or designed using the system. These digital controllers can be instituted by bypassing the analog controller. A DAQ system such as dSPACE and a simulation platform such as Simulink would be necessary to finish the implementation. Comparing and contrasting the analog and digital controllers can give a student first hand knowledge of the effects of sampling and the zero order hold (ZOH) digital to analog conversion. An ambitious student

could use this test bed to perform closed-loop system identification and compare results to a linearized parametric model.

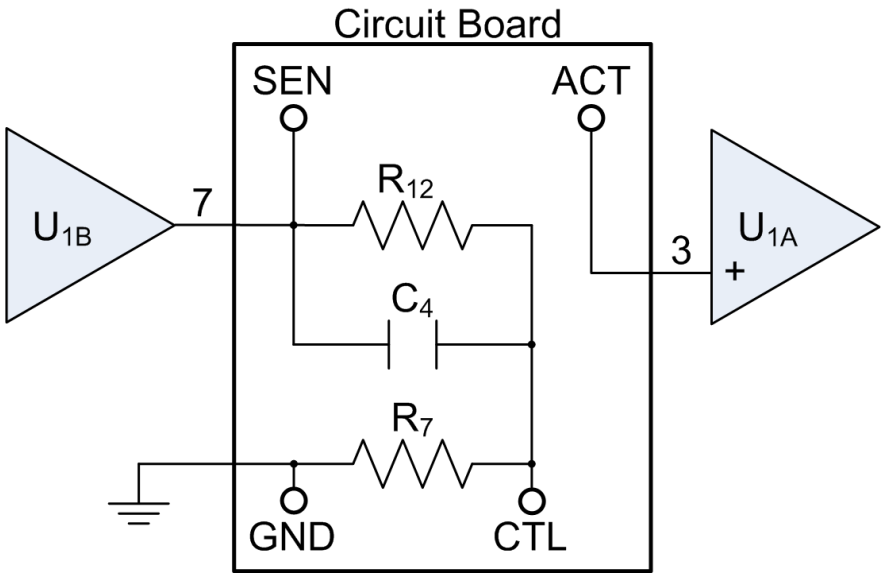

Figure 2.4. Modfied LNS Technologies Levitator Kit Circuit Schematic

2.2 Conceptual Model

Section 2.2.1 presents a first principle derivation of a non-linear dynamic model of the LNS levitation system. The input to this model is the actuator voltage, u, and the output of this model is the position of levitation, y, as shown in Figure 1.1. Section 2.2.2 linearizes the non-linear model developed in Section 2.2.1.

2.2.1 Non-linear Model

As with any electromagnetic system, the dynamics are composed of three parts. The first is a mechanical equation given by Newton's second law that describes the relationship between the position of the mass to the forces acting on the mass. The second is an electromechanical equation that describes the relationship between the current through the electromagnet to the force of electric origin acting on the ferromagnetic mass. The third equation is an electrical

equation that describes the relationship between the actuator input to the current through the electromagnet.

Applying Newton's second law to the free body diagram in Figure 2.5 provides,

$$M\ddot{y} = f_g + f^e(y, i_L), \tag{2.2}$$

where M is the mass of the ferromagnetic object, f_g is the force of gravity, and $f^e(y, i_L)$ is the force of electric origin. By convention, the sign of the force of electric origin is denoted such that an increase in $f^e(y, i_L)$ causes an increase in y.

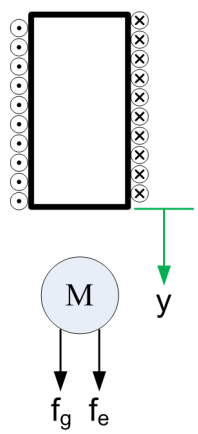

Figure 2.5. Free Body Diagram

Following the analysis in Woodson and Melcher, the force of electric origin is defined using conservation of energy techniques [28]. This force is a function of y whose dependency is introduced through the inductance of the electromagnet,

$$\begin{aligned} L(y) &= L_i + \frac{L_o}{1 + \frac{y}{a}} \\ &= \frac{L_i(a + y) + aL_o}{(a + y)}, \end{aligned} \tag{2.3}$$

where L_i is the self inductance of the electromagnet, L_o is the mutual inductance, and a is a parameter that helps describe how the inductance changes with position of the mass. Given the equation of the inductance, Woodson and Melcher show that the force of electric origin is

given by ,

$$f^e(y, i_L) = -\frac{i_L^2 L_o}{2a\left(1+\frac{y}{a}\right)^2}$$
$$= -\frac{i_L^2 a L_o}{2(a+y)^2}. \tag{2.4}$$

Substituting Equation 2.4 into Equation 2.2 yields,

$$M\ddot{y} = Mg - \frac{i_L^2 a L_o}{2(a+y)^2}. \tag{2.5}$$

For a well designed levitation system, the electrical dynamics are typically much faster than the mechanical dynamics and therefore can be neglected. As this is not always the case, the electrical dynamics will be derived using a partial small-signal model of the LNS system shown in Figure 2.6. In particular, a dynamic model that relates the actuator input, u, to the electromagnet current, i_L, is now determined. The emitter resistance, internal to transistor Q_5, is defined as r_{e5}. The current gain associated with transistor Q_5 is defined as β_5.

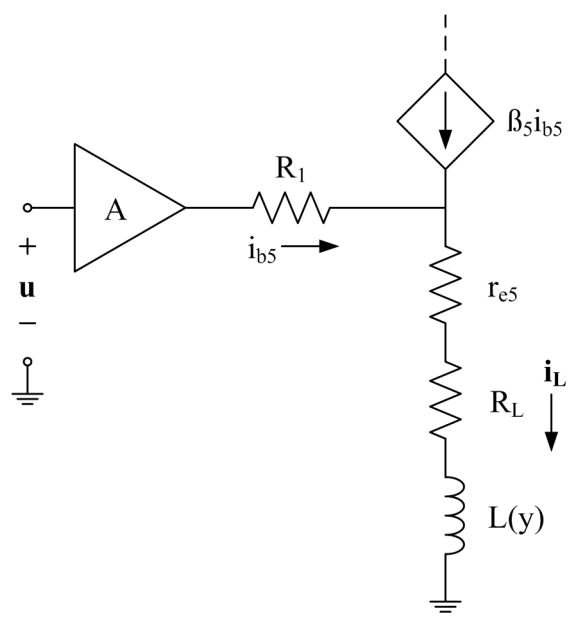

Figure 2.6. Small-Signal Model of the Plant's Electrical Subsystem

Using Kirchhoff's voltage law (KVL),

$$Au = \left(\frac{R_1}{\beta_5 + 1} + r_{e5} + R_L\right) i_L + \frac{dL(y)i_L}{dt}. \tag{2.6}$$

Using the fact that the electromagnetic inductance depends on a time dependent position,

$$\frac{dL(y)i_L}{dt} = i_L \frac{dL(y)}{dy}\frac{dy}{dt} + L(y)\frac{di_L}{dt}. \tag{2.7}$$

Substituting Equation 2.7 into Equation 2.6 and solving for $\frac{di_L}{dt}$ yields,

$$\frac{di_L}{dt} = \frac{1}{L(y)}\left[Au - \left(\frac{R_1}{\beta_5 + 1} + r_{e5} + R_L\right) i_L - i_L \frac{dL(y)}{dy}\frac{dy}{dt}\right]. \tag{2.8}$$

Assuming that β_5 is large and r_{e5} is small compared to R_L,

$$\frac{R_1}{\beta_5 + 1} + r_{e5} + R_L \approx R_L. \tag{2.9}$$

Substituting Equation 2.3 and 2.9 into Equation 2.8 leads to,

$$\frac{di_L}{dt} = \frac{(a+y)}{L_i(a+y) + aL_o}\left[uA - R_L i_L + i_L \frac{aL_o}{(a+y)^2}\dot{y}\right]. \tag{2.10}$$

A non-linear state-space model representation is obtained by using the state variables $x_1 = y$, $x_2 = \dot{y}$, and $x_3 = i_L$ to define the state-space equations,

$$\dot{x}_1 = f_1(x_1, x_2, x_3, u) = x_2 \tag{2.11}$$

$$\dot{x}_2 = f_2(x_1, x_2, x_3, u) = g - \frac{x_3^2 a L_o}{2M(a + x_1)^2} \tag{2.12}$$

$$\dot{x}_3 = f_3(x_1, x_2, x_3, u) = \frac{(a + x_1)}{L_i(a + x_1) + aL_o}\left[uA - x_3 R_L + x_3 \frac{aL_o}{(a + x_1)^2} x_2\right] \tag{2.13}$$

$$y = g(x_1, x_2, x_3, u) \ = x_1. \tag{2.14}$$

2.2.2 Linearized Model

Classical controller design assumes that the system under control is linear-time-invariant (LTI). Therefore it is impossible to implement a classical controller across the full range of any magnetic levitation system. A non-linear system can be "linearized" if the system can be operated in a linear region around an equilibrium point. A classical controller design can then be implemented if the disturbances or reference input are kept small enough to remain in this region.

For a constant input, u_e, the static equilibrium state satisfies,

$$f_1(x_1^e, x_2^e, x_3^e, u_e) = x_2^e = 0 \tag{2.15}$$

$$f_2(x_1^e, x_2^e, x_3^e, u_e) = g - \frac{(x_3^e)^2 a L_o}{2M(a + x_1^e)^2} = 0 \tag{2.16}$$

$$f_3(x_1^e, x_2^e, x_3^e, u_e) = \frac{(a + x_1^e)}{L_i(a + x_1^e) + aL_o}\left[u_e A - x_3^e R_L + x_3^e \frac{aL_o}{(a + x_1^e)^2} x_2^e\right] = 0. \tag{2.17}$$

Solving for the static equilibrium state leads to a linear relationship between x_1^e, x_3^e, and u_e. These relationships can be simplified based on the restriction that the static equilibrium position, x_1^e, must be non-negative. The solutions for the equilibrium state values are,

$$x_1^e = \sqrt{\frac{aL_o}{2Mg}}\frac{A}{R_L}u_e - a \tag{2.18}$$

$$x_2^e = 0 \tag{2.19}$$

$$x_3^e = \sqrt{\frac{2Mg}{aL_o}}(a + x_1^e) = u_e \frac{A}{R_L}. \tag{2.20}$$

The value of the equilibrium input, u_e, can be defined in terms of the value of the equilibrium position, x_1^e, as

$$u_e = \sqrt{\frac{2Mg}{aL_o}}\frac{R_L}{A}(a + x_1^e). \tag{2.21}$$

It is also convenient to define the inductance of the electromagnet when the mass is located

at the equilibrium position,

$$L_e = \frac{L_i(a + x_1^e) + aL_o}{(a + x_1^e)}. \tag{2.22}$$

The linearized state-space A-matrix can be found by taking the Jacobian of the state equations with respect to the state variables and evaluating the result with the static equilibrium states. Similarly, taking the Jacobian of the state equations with respect to the actuator input, u, leads to the B-matrix. The resulting linearized state space model is,

$$\begin{bmatrix} \delta\dot{x}_1 \\ \delta\dot{x}_2 \\ \delta\dot{x}_3 \end{bmatrix} = \begin{bmatrix} 0 & 1 & 0 \\ \dfrac{2g}{a + x_1^e} & 0 & -\dfrac{\sqrt{2aL_oMg}}{M(a + x_1^e)} \\ 0 & \dfrac{\sqrt{2aL_oMg}}{(a + x_1^e)L_e} & -\dfrac{R_L}{L_e} \end{bmatrix} \begin{bmatrix} \delta x_1 \\ \delta x_2 \\ \delta x_3 \end{bmatrix} + \begin{bmatrix} 0 \\ 0 \\ \dfrac{A}{L_e} \end{bmatrix} \delta u \tag{2.23}$$

$$\delta y = \begin{bmatrix} 1 & 0 & 0 \end{bmatrix} \begin{bmatrix} \delta x_1 \\ \delta x_2 \\ \delta x_3 \end{bmatrix}, \tag{2.24}$$

where,

$$x_i(t) = x_i^e + \delta x_i \quad i = 1, 2, 3 \tag{2.25}$$

$$y(t) = y^e + \delta y \tag{2.26}$$

$$u(t) = u_e + \delta u. \tag{2.27}$$

A transfer function representation from the small signal input, δu, to the small signal signal displacement, δy, is

$$G_p(s) = \frac{-\dfrac{\sqrt{2aL_oMg}}{M(a + x_1^e)} \dfrac{A}{L_e}}{s^3 + \dfrac{R_L}{L_e} s^2 - \dfrac{2g}{a + x_1^e} \left(1 - \dfrac{aL_o}{(a + x_1^e)L_e}\right) s - \dfrac{2g}{a + x_1^e} \dfrac{R_L}{L_e}}. \tag{2.28}$$

The characteristic polynomial of the system has the form

$$D(s) = s^3 + a_2 s^2 + a_1 s + a_0, \tag{2.29}$$

where the subscripts of the coefficients refer to the power of the s-term in which they describe. It is expected that the mechanical dynamics of the attractive magnetic levitation system admit two real-valued poles, $\pm p_m$, that are symmetric about the imaginary axis and a single real electrical pole, p_e. Under this assumption, the characteristic polynomial factors as

$$\begin{aligned} D(s) &= (s + p_e)(s^2 - p_m^2) \\ &= s^3 + p_e s^2 - p_m^2 s - p_e p_m^2. \end{aligned} \tag{2.30}$$

Comparing the theoretical transfer function in Equation 2.28 to the expected characteristic equation in Equation 2.30 leads to an expression for the electrical and mechanical pole locations in terms of the values of the static equilibrium states and associated system parameters. The electrical pole location can be determined from the s^2 term as,

$$p_e = -\frac{R_L}{L_e} = -\frac{1}{\tau_e^e}. \tag{2.31}$$

Where τ_e^e is defined as the electrical time constant of the electromagnet at equilibrium. The mechanical pole locations can be found using the s^0 term after factoring out the electrical pole as

$$p_m^2 = \frac{2g}{a + x_1^e}, \tag{2.32}$$

and from the a_1 term as,

$$p_m^2 = \frac{2g}{a + x_1^e}\left(1 - \frac{aL_o}{(a + x_1^e)L_e}\right). \tag{2.33}$$

The fact that Equation 2.32 and Equation 2.33 do not yield identical expressions for p_m^2 shows that the decomposition in Equation 2.30 is not exact. However, it is now shown that Equations 2.32 and 2.33 are approximately equal. Substitute Equation 2.22 into Equation 2.33 shows,

$$p_m^2 = \frac{2g}{a + x_1^e}\left(1 - \frac{aL_o}{L_i(a + x_1^e) + aL_o}\right). \tag{2.34}$$

As $L_i(a + x_1^e) \gg aL_o$,

$$1 - \frac{aL_o}{L_i(a + x_1^e) + aL_o} \approx 1. \tag{2.35}$$

Therefore it is appropriate to approximate the pole locations using

$$p_e = -\frac{R_L}{L_e} \tag{2.36}$$

$$p_{m1,2} = \pm\sqrt{\frac{2g}{a + x_1^e}}. \tag{2.37}$$

Section 2.3.1 verifies this approximation.

The full linearized system model is represented by the block diagram in Figure 2.7, along with a simple feed-forward controller. The small signal parameters, δy and δv_s represent the displacement and sensor voltage, respectively. The small signal δr_s represents the reference input to the linearized closed-loop model and is taken as zero as the controller regulates the system to the equilibrium state. The feed-forward gain term, zero, and pole location of the controller are represented by the parameters k_c, z_c, and p_c, respectively. The sensor gain is represented by the parameter k_s and the gain $-K$ is the numerator of the transfer function in Equation 2.28, where,

$$K = \frac{\sqrt{2aL_oMg}}{M(a + x_1^e)}\frac{A}{L_e}. \tag{2.38}$$

In experiments, the value of the mechanical and electrical poles were found to change slowly with time. It is conjectured that their drift is due to a change in R_L, due to the gradual heating of the electromagnet. The shift in the mechanical pole location can be seen by replacing x_1^e in Equation 2.37 in terms of Equation 2.18,

$$p_{m1,2} = \pm\sqrt{\frac{2gR_L}{\sqrt{\frac{aL_o}{2Mg}}Au_e}}. \tag{2.39}$$

The shift in the electrical pole location can be seen by first replacing x_1^e in Equation 2.22 in terms of Equation 2.18 to show that the equilibrium inductance , L_e, depends on the value of

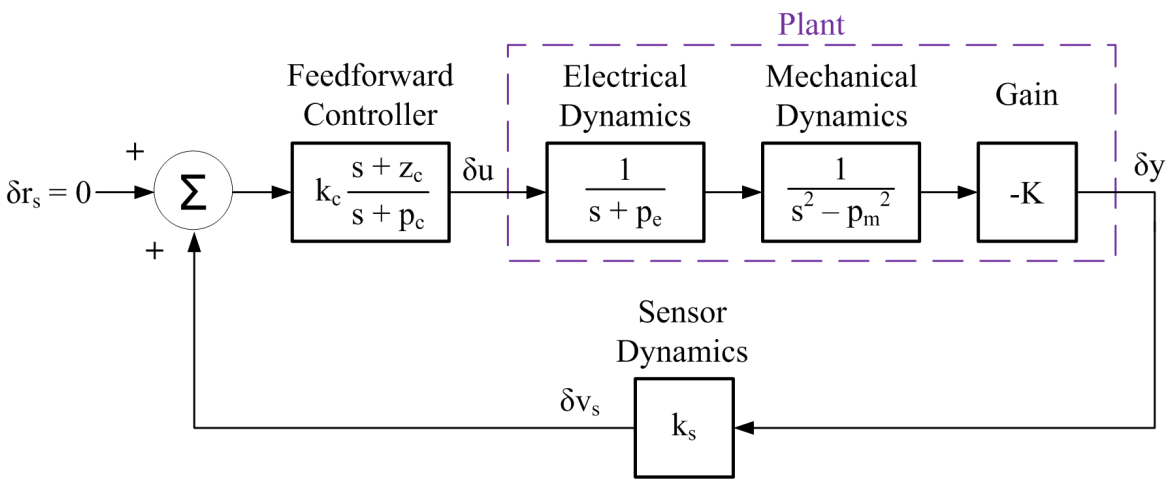

Figure 2.7. LNS Small-Signal Block Diagram

R_L as ,

$$L_e = L_i + \frac{\sqrt{2aL_oMg}}{Au_e}R_L. \tag{2.40}$$

Substituting Equation 2.40 into Equation 2.36 leads to,

$$p_e = -\frac{\frac{R_L}{L_i}}{1 + \frac{\sqrt{2aL_oMg}}{Au_e}\frac{R_L}{L_i}} \tag{2.41}$$

$$\approx -\frac{R_L}{L_i}. \tag{2.42}$$

Section 2.3.1 verifies this approximation.

2.3 System Identification

In order to design the feedback compensator appearing in Figure 2.13, it is first necessary to obtain numeric values for the parameters in the linearized state space model given by Equations 2.23 and 2.24 as well as the sensor gain, k_s, first appearing in Figure 2.7. These parameters are obtained using a two-step process. As a first step, Section 2.3.1 describes the open-loop experiments designed to estimate the value of the parameters a, L_i, L_o, R_L, and

M. The second step is described in Section 2.3.2 where the small-signal plant model given in Equation 2.28 is estimated from closed-loop system identification data. The identified model is used to obtain the value of the sensor gain, k_s, as well as to verify the parameter estimates found from the open-loop experiments.

2.3.1 Open-Loop Measurements of Model Parameters

This section describes a series of open-loop measurements to determine the values of the parameters a, L_i, L_o, R_L, and M that appear in the linearized model described in Equations 2.23 and 2.24. These parameters are then used to verify assumptions made in Section 2.2.2. The easiest parameter to obtain is the mass of the ferromagnetic mass which is essentially a hollow metal sphere. The diameter of the sphere is approximately 1in while its mass is approximately 3.246g. The diameter of the sphere is designed to be slightly larger than the pole of the electromagnet. This is done so that the sphere tends to remain centered on the axis of the electromagnet in order to maximize the self inductance.

The inductance of an electromagnet is inferred by measuring the time constant of a sample RL circuit comprised of the electromagnet and a series resistor. It is well known that for a first-order system with no finite zeros that the 10 - 90% rise time is related to the system time constant by,

$$t_r = \tau \ln 9 = \frac{L}{R} \ln 9. \tag{2.43}$$

By measuring the rise time of the signal across the series resistor, it is possible to determine the value of L. From Section 2.2.1, it is known that the inductance of the electromagnet is a function of y. Therefore, multiple experiments must be performed where the mass is positioned at known distances from electromagnet. The inductance parameters of the system were determined using a similar electromagnet from another LNS levitator kit. This particular electromagnet was used because it had not yet been assembled, therefore, it was easy to create a simple RL circuit and to flip it upside down to create a stable base in which to accurately position the mass.

The resistance of the function generator, series resistor, and DC resistance of the electromagnet were measured prior to the experiment to find the total resistance of the circuit,

$R_{total} = 135.52\Omega$. In terms of the measured rise-time and measured resistance R_{total}, the inductance is determined as,

$$L = \frac{t_r R_{total}}{\ln 9}. \tag{2.44}$$

For each experiment, a $6V_{pp}$ square wave voltage signal with frequency of 25Hz was applied to the circuit. The frequency was chosen sufficiently small so that the full rise and fall time of the waveform could be observed. The signal amplitude was chosen such that the voltage drop across the electromagnet is $3V$. A similar voltage drop was measured across the electromagnet in the system under test while operating at an equilibrium point.

Two experiments are performed to measure L_i and L_o. The self inductance parameter, L_i, is measured by removing the ferromagnetic mass, equivalent to setting $y = \infty$. In the second experiment, the mass is placed directly on top of the core of the electromagnet, equivalent to setting $y = 0$. The resulting inductance is equal to $L_i + L_o$. Subtracting these two inductance values will result in the experimental value for L_o. The measured values for L_i and L_o are 97.3mH and 79.5mH, respectively. Four other experiments were performed, using calibrated plastic spacers to change the position of the mass in relation to the electromagnet. Table 2.1 shows the recorded rise-time values and related calculated inductance values.

A least-squares estimate of the parameter a is obtained by measuring the inductance as a function of y. From Equation 2.3,

$$\frac{L_o}{L(y) - L_i} = 1 + \frac{1}{a}y. \tag{2.45}$$

Using Equation 2.45, a least-squares estimate of a is found using the data in Table 2.1. Figure 2.8 shows experimental and simulated inductance versus distance. Table 2.2 lists the experimentally calculated and measured data necessary to determine the pole locations of the theoretical linearized plant model in terms of equilibrium position.

y [cm]	t_R [ms]	L [mH]
0	2.87	176.8
2.44	1.67	102.9
4.06	1.63	100.4
5.69	1.62	99.8
7.32	1.58	97.3
∞	1.58	97.3

Table 2.1. Experimental Data Used to Calculate Inductance Parameters

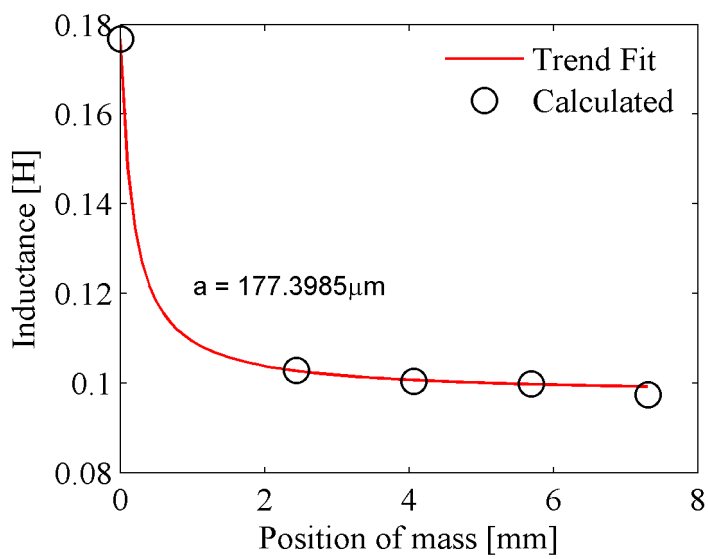

Figure 2.8. Inductance of the Electromagnet versus Position of Mass

Variable	Description	Measured Value
M	Mass of Levitated Object	$3.246[g]$
R_L	DC Resistance of the Electromagnet	$32.58[\Omega]$
L_i	Self Inductance	$97.3[mH]$
L_o	Mutual Inductance	$79.5[mH]$
a	Parameter of L(y)	$177.4[\mu m]$

Table 2.2. Measured and Calculated Parameter Values for the LNS System

2.3.1.1 Verification of Small-Signal Model Assumptions

Section 2.2.2 discussed several approximations describing the linearized systems' pole locations. Bounds for the accuracy of these approximations can now be determined using the data from Table 2.2. The approximate electrical and mechanical pole locations, described by Equations 2.36 and 2.37, were evaluated using the data from Table 2.2 over a range of potential equilibrium positions. The same data set was used to determine the actual pole locations by numerically determining the pole locations of Equation 2.28. Figures 2.9 and 2.10 show a comparison of the approximate electrical and mechanical locations against the pole locations obtained from the transfer function of Equation 2.28. It can be seen that the mechanical pole approximations remain close to the theoretical locations while the electrical poles vary when the equilibrium position becomes small, ($x_1^e < 2$mm). When the equilibrium position becomes very small, ($x_1^e < 1$mm), the left hand plane poles become complex, therefore the approximations are no longer applicable. As the equilibrium position measured in Section 2.3.2 is 3.2mm, the approximations shown in Equations 2.36 and 2.37 can be considered to be accurate.

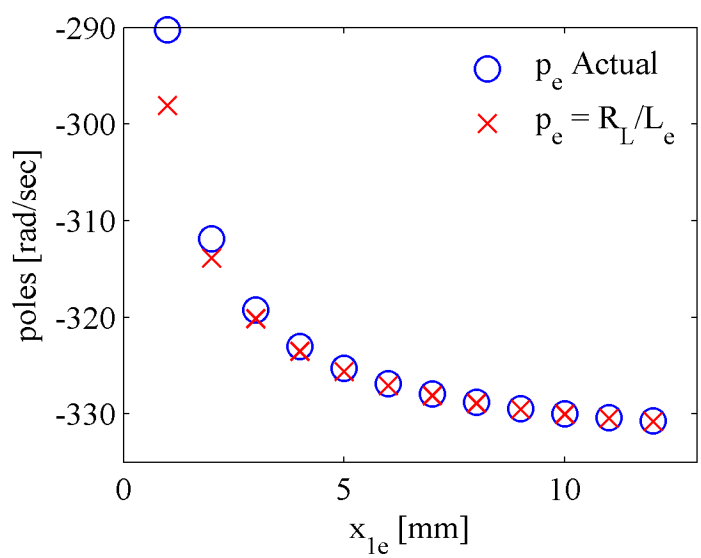

Figure 2.9. Theoretical Electrical Pole Locations Versus Equilibrium Position

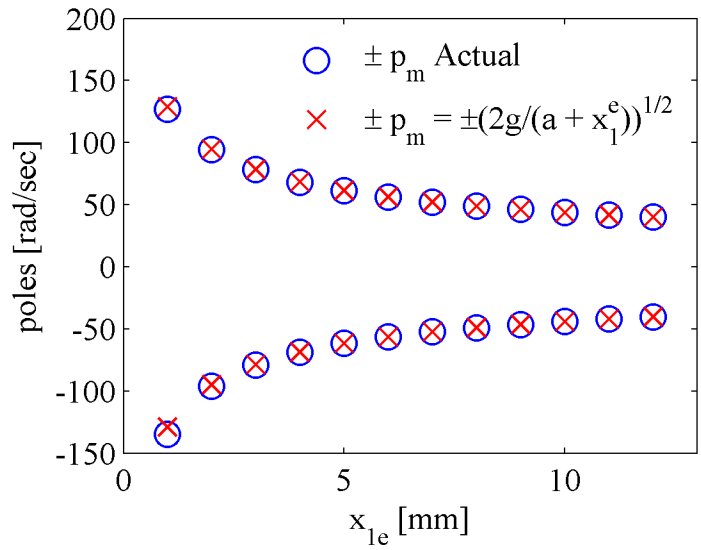

Figure 2.10. Calculated Mechanical Pole Locations Versus Equilibrium Position

When discussing the potential effects of the change of the inductor resistance, R_L, on the electrical pole location, p_e, the following approximation was made,

$$p_e \approx -\frac{R_L}{L_i}. \tag{2.46}$$

The validity of this approximation is now verified using the data in Table 2.2. Figure 2.11 shows Equation 2.41 evaluated over a range of inductor resistance values, R_L, and the entire equilibrium input range, u_e, of the LNS levitator system. Figure 2.12 shows the maximum error between Equation 2.41 and its approximation in Equation 2.42, due to inductor resistance, R_L. It is obvious that the electrical pole, p_e, has only a minor dependence on the value of the equilibrium input, u_e, for reasonable values of R_L. Therefore, it is reasonable to approximate the electrical pole using equation 2.42.

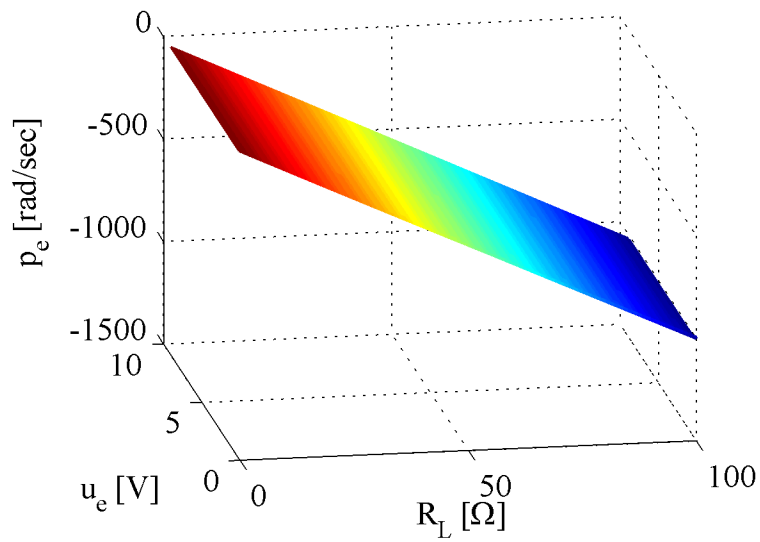

Figure 2.11. Calculated Electrical Pole Locations Due to Equilibrium Input and Electromagnet Resistance

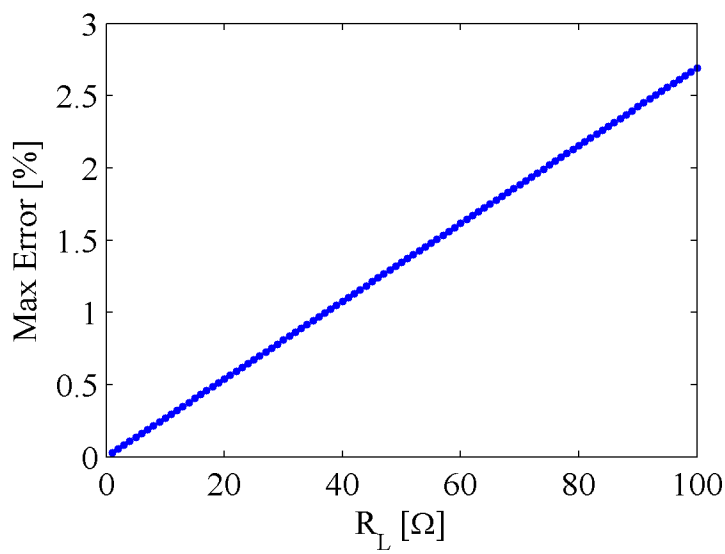

Figure 2.12. Maximum Error of the Electrical Pole Approximation Due to Electromagnet Resistance

2.3.2 Identification of a Small-Signal Plant Model

This section describes a series of closed-loop system identification experiments for determining the parameters of the linearized transfer function given by Equation 2.28. These measurements are necessary for three reasons. First, the results of these system identification experiments, found in Section 2.3.3, will be used to verify the open-loop estimation obtain in Section 2.3.1. Second, these measurements will also determine the linear region of operation. In specific, the smallest value of the small-signal input, δr_e, that causes a deviation from linear model behavior is noted. Third, it is necessary to obtain an estimate of the small-signal sensor gain, k_s while the ferromagnetic mass is near the equilibrium point. The identified plant model, $\bar{G}_p$, identified in Section 2.3.3 will differ from the transfer function G_p in Equation 2.28 by the sensor gain, k_s.

A series of two closed-loop system identification experiments were performed. In the first experiment, the existing phase-lead analog controller was replaced by its zero-order hold (ZOH) discrete time equivalent. As will be discussed, this implementation led to an undesirable oscillation of the small-signal output, δv_s. In the second experiment, the original analog controller was modified and used to perform system identification experiments. The undesirable oscillation of the small-signal output, v_s, were not observed during the second experiment.

In the first experiment, a digital controller was designed based upon a zero-order hold (ZOH) discrete transform of the analog controller, represented as,

$$Gc(z) = \frac{z - 0.9873}{z - 0.1229} \qquad T_s = 0.001s. \tag{2.47}$$

This controller was implemented in Simulink and then downloaded and run on a dSPACE CLP1104 DAQ system. The analog controller, detailed in Figure 2.2, was bypassed using the modifications discussed in Section 2.1.1. This implementation provided an accessible means of generating and recording the small-signal excitation signal, δr_e, as well as recording the small-signal sensor output, δv_s.

Placement of the small-signal excitation signal, δr_e, is key to the success of these experiments. The electrical dynamics act as a low-pass filter, therefore, the frequency of the excitation signal must be set slow. The frequency of the excitation signal, f_{re}, was tuned in

dSPACEs ControlDesk program and set to 0.5Hz so that the full rise and fall time response of the sensor output could be observed. In a similar manner, the magnitude of the excitation signal was chosen to be $2mV_{pp}$, such that a small-signal response could be observed on the sensor output but not large enough to observe a non-linear small-signal output, δv_s, response.

The controller acts as a high-pass filter, therefore injecting the low-frequency small-signal excitation signal at the input of the controller will attenuate the signal. Injection of the excitation signal should occur between the controller and the plant in order for these experiments to produce useful results. This has the added effect of changing the structure of the system, original shown in Figure 2.7 to that of Figure 2.13, where the controller is in the feedback path.

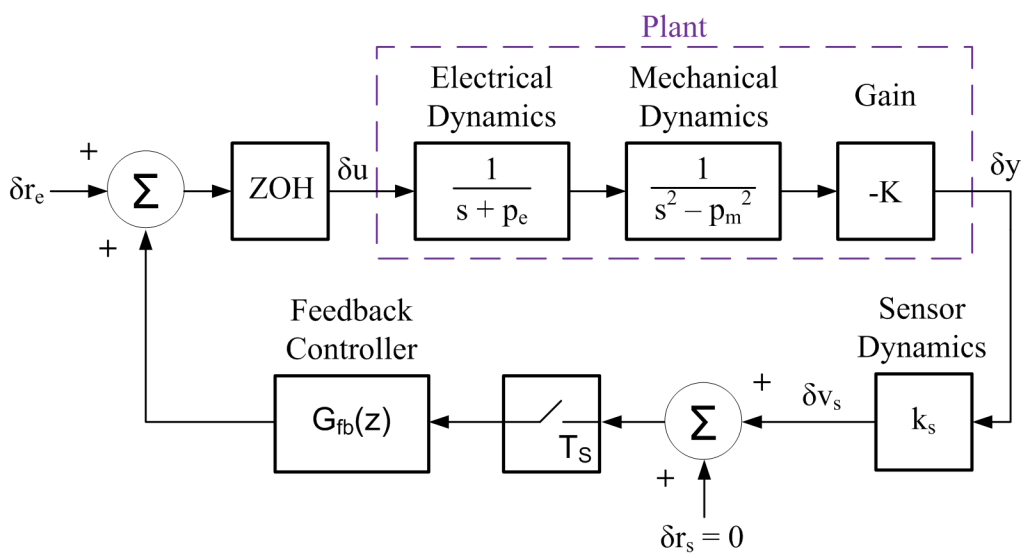

Figure 2.13. LNS Small-Signal Block Diagram Modified With A Digital Controller

During the first experiment, oscillations in the mass's position and small-signal sensor output, δv_s, were observed that were not related to the small-signal excitation signal, δr_e. Using this data caused identification errors in the plant model. As this effect was not observed with the analog controller, it was thought that by increasing the sampling frequency from 1kHz to 10kHz, so that the discrete time transfer function is a better approximation to the analog controller, that the oscillations would decrease in amplitude or vanish. However, it was found that this was not the case.

The second experiment was designed to take advantage of the existing analog controller. The small-signal excitation signal, δr_e, implemented in Simulink, is coupled into the output

of the controller through a resistor, R_C, as shown in Figure 2.14. The small-signal actuator input, δu, can be defined in terms of the small-signal sensor output, δv_s, and the small-signal excitation signal, δr_e as,

$$\delta u = \frac{s + \dfrac{1}{R_{12}C_4}}{s + \dfrac{R_{12}(R_7 + R_C) + R_7 R_C}{R_{12}R_7R_CC_4}}\delta v_s + \frac{\dfrac{1}{R_CC_4}}{s + \dfrac{R_{12}(R_7 + R_C) + R_7 R_C}{R_{12}R_7R_CC_4}}\delta r_e. \tag{2.48}$$

The system is modeled as having both feedback and a feed-forward controllers such that,

$$\delta u = G_{fb}\delta v_s + G_{ff}\delta r_e. \tag{2.49}$$

The controllers are represented in terms of controller parameters k_s, p_c, and z_c the controller gain term, pole location, and zero location, respectively, as,

$$G_{ff} = \frac{k_c}{s + p_c} \tag{2.50}$$

$$G_{fb} = \frac{s + z_c}{s + p_c}. \tag{2.51}$$

A block diagram representation of this system is shown in Figure 2.15. A trade-off can be found from the analysis of Equation 2.48 when selecting the coupling resistor, R_C. If R_C is very large in comparison to $R_7 = 2.2k\Omega$, then the feedback controller, G_{fb}, is equivalent to the original analog controller described in Equation 2.1. Picking R_C large will also attenuate the small-signal excitation signal, δr_e. Therefore the coupling resistor was chosen as $R_C = 24.9k\Omega$ so that it would have minimal effect on the existing controller circuitry yet not dramatically attenuate the excitation signal.

Substituting in for the component values in Equation 2.48 from the circuit schematic in Figure 2.2 leads to,

$$G_{fb} = \frac{s + 30.3}{s + 2279} \tag{2.52}$$

$$G_{ff} = \frac{182.6}{s + 2279}. \tag{2.53}$$

Where the controller parameters are now defined as,

$$k_c = 182.6 \tag{2.54}$$

$$p_c = 2279 \tag{2.55}$$

$$z_c = 30.3. \tag{2.56}$$

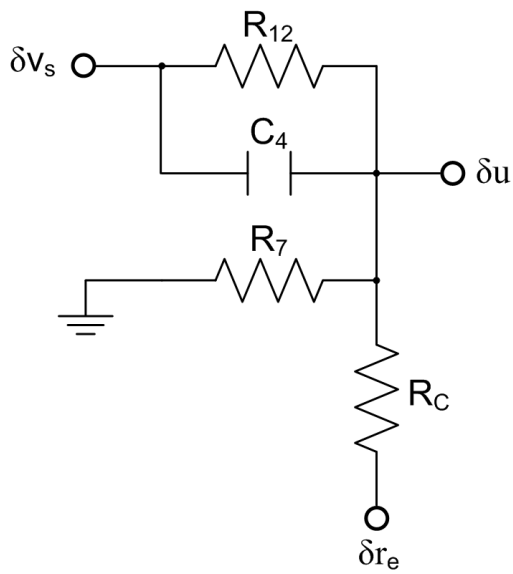

Figure 2.14. Modfied LNS Levitator Analog Controller

The small-signal sensor output, δv_s, was found to be noisy, therefore, to increase the signal to noise ratio (SNR), 100 10-second runs were averaged together. The sensor output data, for each run, was aligned with each of the others by truncating the start of the data to the first rise-time of the associated excitation signal. All runs were then truncated to the length of the smallest run. Each run was then reviewed for significant environmental disturbances and removed if necessary. Figure 2.16 details the 100 run averaged small-signal excitation input. Figure 2.17 details the 100 run averaged small-signal sensor output.

A linear model for the closed loop system, G_{cl}, was identified from the 100 run averaged output, shown in Figure 2.17, using MATLAB's pem function with the continuous-time process model option. While other pem options and a batch least square (BLSE) algorithm were used, the continuous-time process model option provided the best results. It should

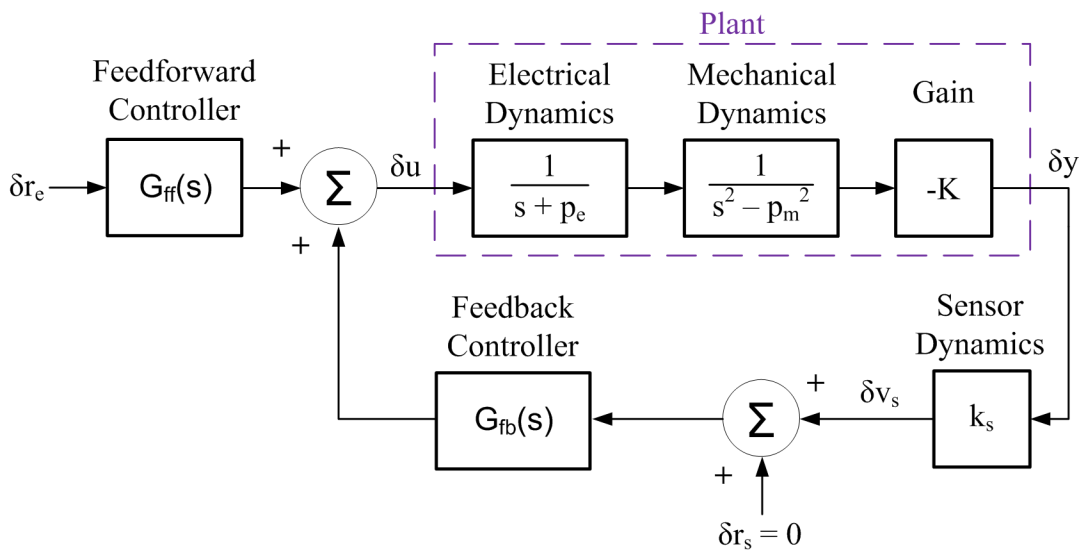

Figure 2.15. LNS Small-Signal Block Diagram Modified For System Identification

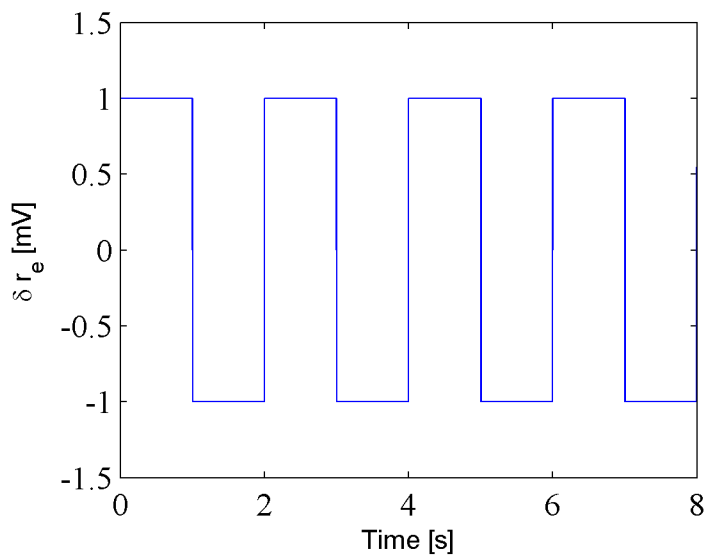

Figure 2.16. 100 Run Average of the Reference Input of the Closed-Loop System

be noted that the continuous-time process model option is inherently limited to identifying processes with a maximum of three poles. While the expected closed-loop model, G_{cl}, contains four poles, Section 2.3.3 will show that the identified plant model, $\bar{G}_p$, can still be identified from a model with three poles.

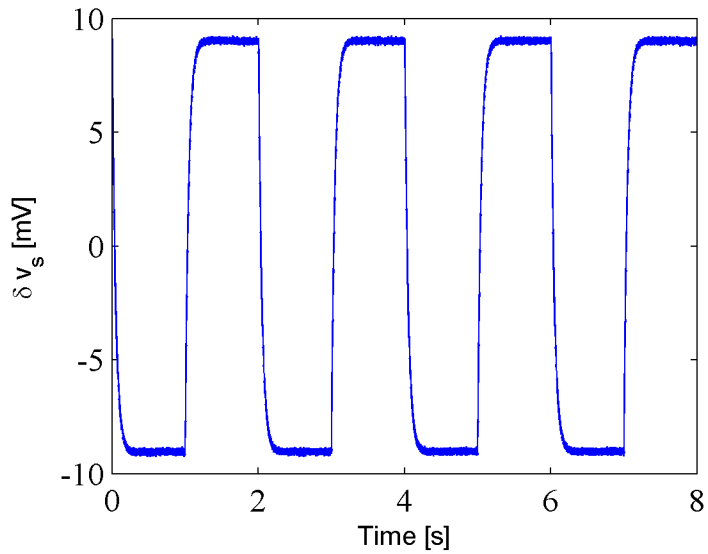

Figure 2.17. 100 Run Average of the Sensor Output of the Closed-Loop System

2.3.3 Summary of Results

This section details the results of the closed-loop system identification process for the plant of the LNS levitator system and compares these results to the theoretical plant model using the parameters found in Section 2.3.1. The small-signal sensor gain, k_s, is calculated using the closed-loop system DC gain and system parameters. Prior to the experimental measurements, the sensitivity knob on the front of the LNS levitator was adjusted until the mass was being levitated in the middle of its dynamic range. This equilibrium position was measured at approximately (0.125in) 3.2mm from the electromagnet. The expected equilibrium inductance was calculated to be, $L_e = 101.5mH$ from Equation 2.22 and the data in Table 2.2. Equations 2.36 and 2.37 were used to approximate the electrical pole location at -321 rad/sec and the mechanical pole locations at ± 76.2 rad/sec.

Using pem, the continuous closed-loop model is identified as,

$$G_{cl}(s) = \frac{-3.17e7}{(s + 21.49)(s^2 + 283.6s + 1.635e5)}. \tag{2.57}$$

Given that the linearized plant model from Equation 2.28 has three poles and the controller has one pole, it is expected that the closed-loop model, G_{cl}, will have four poles. A simulation using the closed-loop model in Equation 2.57 and the averaged small-signal excitation signal,

δr_e, is shown in Figure 2.18. The accuracy of the three pole simulation suggests that the fourth pole was at a high frequency and could be neglected.

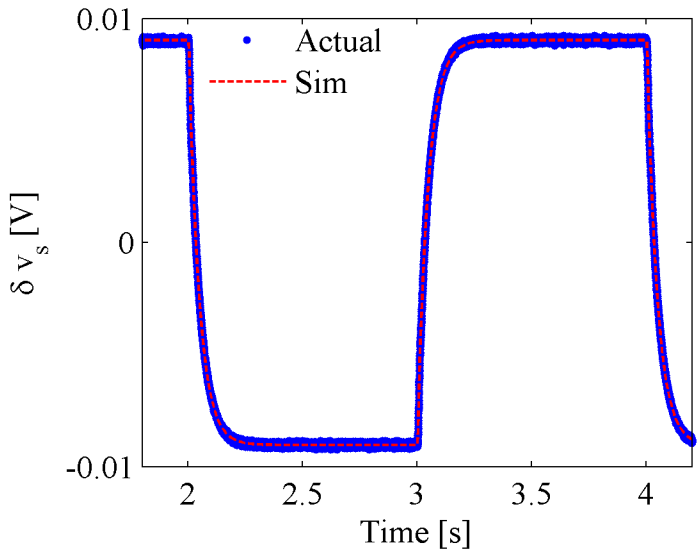

Figure 2.18. Simulation Using the 3rd-Order Approximation of the Closed-Loop System

The closed-loop model, G_{cl}, can be written as a algebraic equation in terms of the component systems from Figure 2.15 as,

$$G_{cl} = \frac{G_{ff} G_p k_s}{1 - G_{fb} G_p k_s}, \tag{2.58}$$

where the identified plant model is,

$$\bar{G}_p = G_p k_s. \tag{2.59}$$

The identified plant model, $\bar{G}_p$, can be identified, in terms of known systems, by manipulating Equation 2.58 as,

$$\bar{G}_p = \frac{G_{cl}}{G_{ff} + G_{cl} G_{fb}}. \tag{2.60}$$

Equation 2.58 is evaluated as,

$$\bar{G}_p(s) = \frac{-1.74e5(s + 2279)}{(s + 299.8)(s + 79.17)(s - 73.9)}. \tag{2.61}$$

The extra zero is expected to have been cancelled out by the missing high frequency pole in the closed-loop model. Therefore, the plant model was modified by removing the unexpected zero, while maintaining the same DC gain, as

$$\bar{G}_p(s) = \frac{-3.96e8}{(s+299.8)(s+79.17)(s-73.9)}. \tag{2.62}$$

Using Equation 2.58, the plant model, in Equation 2.62, was used to recreate the closed-loop model as

$$G_{cl}(s) = \frac{-72.3e9}{(s+2360)(s+21.58)(s^2+202.8s+1.572e5)}. \tag{2.63}$$

As anticipated, this closed-loop model includes a high frequency fourth pole. Final verification of the plant model, $\bar{G}_p$, was accomplished by simulating the recreated closed-loop model, shown in Equation 2.63. The visual accuracy of the results of the simulation, shown in Figure 2.19, verifies the plant model.

Having first verified the plant model, $\bar{G}_p$, the small-signal sensor gain, k_s, can now be found. If Equations 2.50, 2.51, and 2.28 are substituted into Equation 2.58, the closed-loop system gain, $K_{DC,CL} = G_{cl}|_{s=0}$, for the system in Figure 2.15 can be represented as

$$K_{DC,CL} = \frac{-\dfrac{k_c}{z_c}}{1-\sqrt{\dfrac{2Mg}{aL_o}}\dfrac{p_c}{z_c k_s}\dfrac{R_L}{A}}. \tag{2.64}$$

Equation 2.64 can be manipulated to solve for the small-signal sensor gain, k_s, as

$$k_s = \sqrt{\frac{2Mg}{aL_o}}\frac{R_L}{A}\frac{p_c(K_{DC,CL})}{z_c(K_{DC,CL})+k_c}. \tag{2.65}$$

The small-signal sensor gain, k_s, is now be evaluated using the numeric values for the controller parameters in Equations 2.54 - 2.56, the DC gain from Equation 2.63, and the parameters from Table 2.2 in to Equation 2.65 to obtain

$$k_s = 1.37e3\left[\frac{V}{m}\right]. \tag{2.66}$$

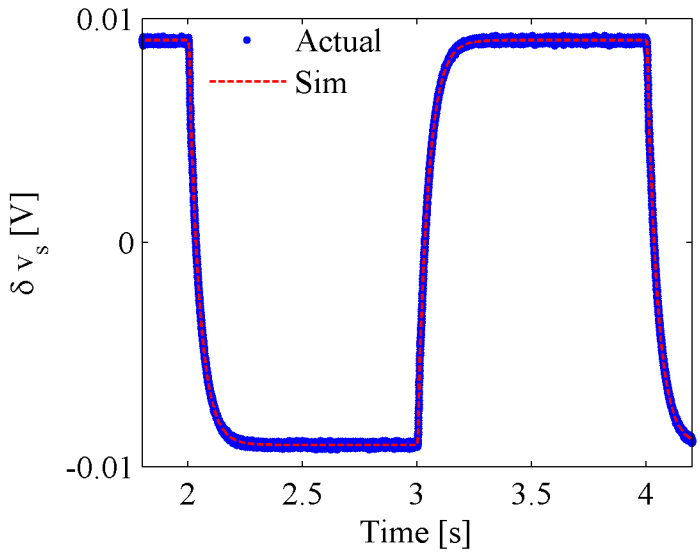

Figure 2.19. Simulation Using the 3rd-Order Approximation of the Plant

The procedure followed in experiment two was preformed three more times and the results of each experimental system identification are listed in Tables 2.3 and 2.4. The identified plant pole locations are compared to the expected pole locations at -321 rad/sec and ±76.2 rad/sec. It can be seen that there is a large error in the pole locations of the identified plant of experiment 2d. This suggests that, for this system configuration, an excitation signal of 4mV$_{pp}$ or larger will push the system out of its linear region at the equilibrium point, $x_1^e =$ 3.2mm. The sensor gain k_s was calculated for all experiments as was done in Equation 2.65. The average of the the sensor gains for experiments 2a-2c are used to approximate the sensor gain as,

$$k_s(avg) = 1.43e3 \left[\frac{V}{m}\right]. \tag{2.67}$$

Table 2.4 is shows the gain values and the error calculations in relation to the average sensor gain value.

As was discussed in Section 2.2.2, it is expected that heating effects change the pole locations, thus run averaging leads to averaging of slightly different systems. Figure 2.20 shows the average sensor value of 400 10-second sequential runs. The 10.6% change in the average sensor value should correlate to a change in the equilibrium position and thus a change in the system dynamics over time. While averaging of systems with close but separate

Exp.	δr_e $[mV_{pp}]$	Pole	Identified	Pole Error
2a	2	p_e	-300 [rad/sec]	-6.5%
		p_{m1}	-79.2 [rad/sec]	+3.9%
		p_{m2}	+73.9 [rad/sec]	-3.0%
2b	2	p_e	-363 [rad/sec]	+13.1%
		p_{m1}	-69.5 [rad/sec]	-8.8%
		p_{m2}	+70.2 [rad/sec]	-7.9%
2c	2	p_e	-276 [rad/sec]	-14.0%
		p_{m1}	-84.8 [rad/sec]	+11.3%
		p_{m2}	+73.9 [rad/sec]	-3.0%
2d	4	p_e	-177 [rad/sec]	-44.9%
		p_{m1}	-142 [rad/sec]	+86.4%
		p_{m2}	+53.6 [rad/sec]	-29.7%

Table 2.3. Error Calculations Between Theoretical and Identified Pole Locations

Exp.	$G_{cl}(s)\|_{(s=0)}$ [V/V]	k_s [V/m]	Error
2a	-9.03	1.37e3	-4.2%
2b	-8.83	1.44e3	+0.7%
2c	-8.70	1.49e3	+4.2%
2d	-8.11	1.78e3	+24.5%

Table 2.4. Error Calculations Between Identified and Average Gains

dynamics could lead to identification of a system that is close to expected (as in experimental results from Table 2.3), it is also possible that they lead to identification of systems with greater inconsistencies.

It should be stated that a source of error could be due to the identification process itself. Closed-loop identification adds a layer of complexity to the analysis as there may be a linear dependence between the identified system and the controller for first-order controllers. While it is assumed that the dependence between the controller and the plant is negligible, this could still cause some discrepancies in the identified plant model.

2.4 Controller Design

Given the identified small-signal model parameters from experiment 2a, a digital controller is now synthesized for a third experiment. Comparing the predicted and measured response of the closed-loop system will confirm the identified system model. The goal of experiment

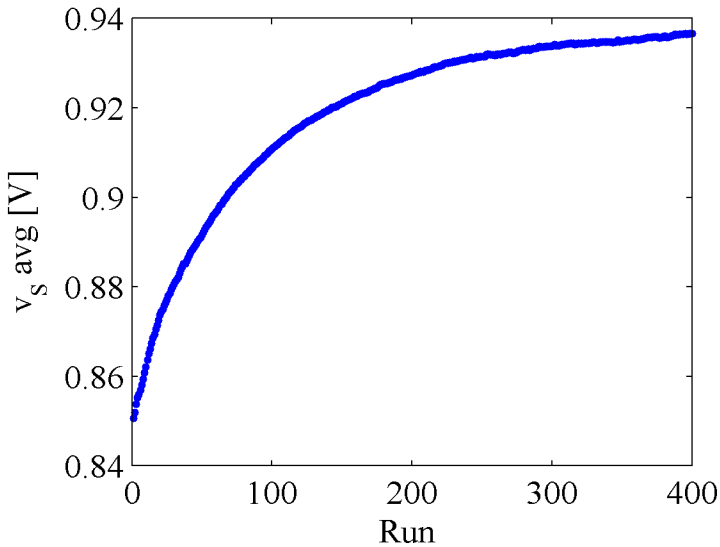

Figure 2.20. Average Value of the Sensor Voltage Over Runs

three is to design and verify a controller that places the dominant closed-loop poles at 125 rad/sec with a damping ratio that establishes a 25% overshoot. It is understood that this designed overshoot will not be achieved due to the interaction of the dominant poles with the other system dynamics. A continuous feedback controller was designed using root locus techniques to place the desired closed-loop poles. The continuous controller is designed as

$$G_c(s) = 0.216\frac{(s+112.9)}{(s+2124)}. \tag{2.68}$$

The controller's zero-order hold discrete-time equivalent model at a sampling frequency of 10kHz is

$$G_c(z) = \frac{0.216z - 0.2138}{z - 0.8086} \quad T_S = 0.0001. \tag{2.69}$$

Figures 2.21 and 2.21 show the rise and fall time of captured data from experiment three, plotted against the simulated response of the expected closed-loop system, derived from the plant model identified in experiment 2a. The small-signal excitation signal was set as in experiment 2a, δr_e is a $2mV_{pp}$ square wave at 0.5Hz. The expected overshoot from simulation of the expected closed-loop system is 18.7% while the measured overshoot is only 11.2%. The expected DC gain of the closed-loop system is -141.8 [V/V] while the measured experimental

DC gain of the system is -109 [V/V].

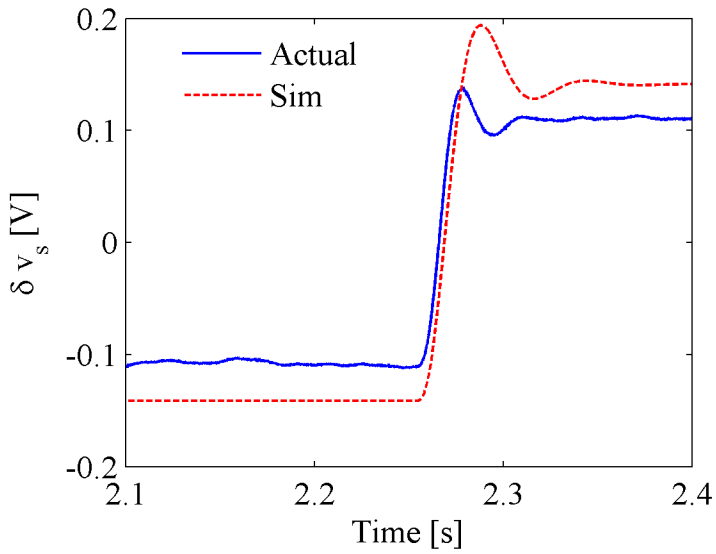

Figure 2.21. Closed-Loop Rise-Time Response due to the Controller Design Vs. Expected Response

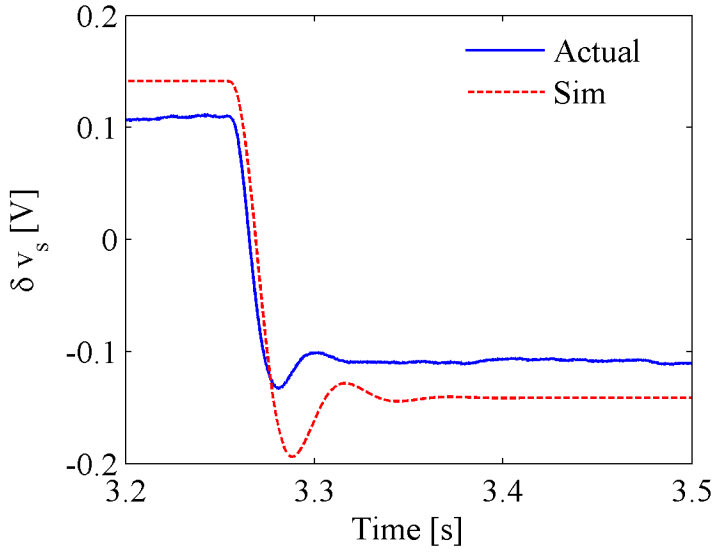

Figure 2.22. Closed-Loop Fall-Time Response due to the Controller Design Vs. Expected Response

Due to the differences between the expected and measured transient and steady state performance, the plant transfer function was re-identified from experiment three data as,

$$\bar{G}_p(s) = \frac{-5.91e8}{(s+312)(s+74.95)(s-58.78)}. \tag{2.70}$$

Figure 2.23 verifies the re-identified plant model in Equation 2.70 through simulation of the closed-loop plant model, using Equation 2.70, and comparison to the actual response. For comparison, the expected plant model from experiment 2a is re-listed as,

$$\bar{G}_p(s) = \frac{-3.96e8}{(s+299.8)(s+79.17)(s-73.9)}. \tag{2.71}$$

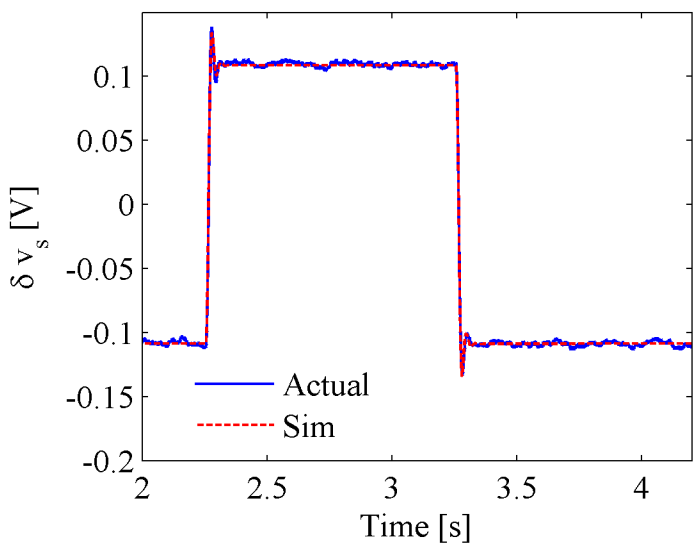

Figure 2.23. Closed-Loop Response due to the Controller Design Vs. Response of Re-Identified Plant

	p_e	p_{m1}	p_{m2}	Mp %	$G_{cl}(s)\|_{(s=0)}$
Expected	-299.8	-79.17	+73.90	18.7	-141.8
Exp. 3	-312.0	-74.95	+58.78	11.2	-109.0
Error	+4.07%	-5.33%	-20.5%	-40.1%	-23.1%

Table 2.5. Error Calculations Between Expected and Actual Response of the System with Designed Controller

The main source of error stems from the value of the right-hand plane pole, p_{m2}, from experiment 3. The error calculations, shown in Table 2.5, are suggestive of the results found in experiment 2d, listed in Tables 2.3 and 2.4, where the system had been driven from the linear region. The amplitude and frequency of the small-signal excitation signal, δr_e, was set the same for both experiments 2a and 3, therefore a direct comparison of the closed-loop DC gain from these experiments can be used to compare the range over which the mass moves.

The DC gain of the closed-loop system found in experiment 2a is found from Equation 2.57 as

$$G_{cl}(s)|_{(s=0)} = -9.02[V/V]. \tag{2.72}$$

The DC gain of the expected system is listed in Table 2.5 as -141.8 [V/V]. The ratio of these gains show that the expected movement of the mass in response to δr_e is 15.7 times larger for experiment 3 than experiment 2a. It is thought that the large percent difference for the value of p_{m2} and Mp% in Table 2.5 is the result that the large displacement in experiment 3 drives the system outside of the linear operational range.

Experiment 3 was repeated at a later date when the room temperature was much cooler. The closed-loop system dynamics were observed to have changed from an under-damped response to an over-damped response for both the original small-signal excitation signal, δr_e, and for one with an amplitude of $100\mu V_{pp}$. The device has also been observed to be very responsive to environmental disturbances such as the heating, ventilation, and air conditioning (HVAC) system turning on in the room. It is concluded that there too many environmental factors to accurately predict the response of the system on a real time basis. Accuracy of the system's response to a designed controller will be achieved only when looking at the average of the system's response over time.

Chapter 3

Levitation System using Hall Effect Sensing

Chapter 3 details the design objectives, challenges, and schemes used in the design of a magnetic levitation system that demonstrates both attractive and repulsive levitation and that uses Hall effect sensing to determine position. Section 3.1 introduces a system designed by Marsden [3] in which this test-bed was originally based upon and details the design objectives. In Section 3.2, the design challenges and trade-offs for the Hall sensor based position sensor are discussed. The over-all electrical and mechanical system design choices are discussed in Section 3.3. Section 3.4 examines the experimental measurements necessary to implement position sensing and current sensing, and discusses criteria for the determination of the equilibrium points. Section 3.5 concludes with illustrations of the final system and describes the electrical circuit board layout and the build of the mechanical structure.

3.1 Commercial System and Design Objectives

In this section, a commercially available magnetic levitation system which uses a Hall effect sensor as the feedback element is discussed. The commercial system is analyzed and shown to have several strengths and weaknesses. The design objectives for the magnetic levitation system presented in this thesis are established from the analysis of this commercial system.

In 2003, Guy Marsden published an article in *Nuts and Volts Magazine* detailing a magnetic levitation system which attractively levitates a magnetic mass [3]. His design has three notable features. First, by using a magnetic mass in place of a ferromagnetic mass, the current required to achieve a given levitation position is reduced. Second, Marsden drives the electromagnet using a PWM system rather than a class A amplifier as in the commercial system discussed in Chapter 2. As a result, the power dissipated in the semiconductor device used to generate the magnetic current is significantly reduced. Third, Marsden uses a Hall effect sensor to measure the position of the levitation mass. In comparison to the optical system discussed in Chapter 2, the implementation allows one to regulate the position of the mass over a greater range.

Figure 3.1 shows a conceptual sketch of Marsden's levitation system. The H-bridge can be viewed as a switch that connects the electromagnet directly to the power source. The direction input determines whether the current, i_L, is positive or negative. The input to the direction input is a TTL-level square wave, v_D, created by the PWM chip. When the duty cycle is 50%, the average value of i_L is zero. The frequency of the PWM signal, f_D, is set through an external capacitor, C, and the duty cycle, D, is determined by the voltage, v_S, provided from Hall effect sensor. If the orientation of the Hall effect sensor and connection between the electromagnet and H-bridge are set appropriately, feedback of the reference signal from the Hall effect sensor will allow the system to attractively levitate the mass.

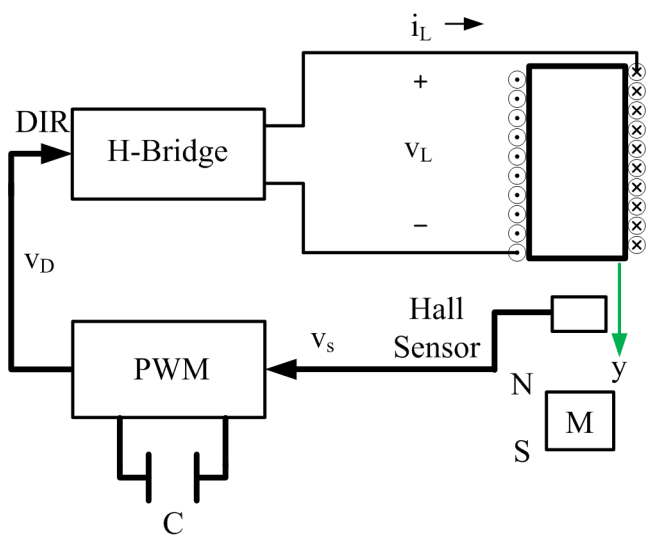

Figure 3.1. Block Diagram Representation of Marsden's System

A prototype of Marsden's system was created at the Pennsylvania State University by three honors students in EE350 during the Fall 2007 semester [29]. Figure 3.2 shows a profile of the electromagnet and Hall sensor assembly and Figure 3.3 shows the circuit board that correlates directly to the remaining components from the block diagram in Figure 3.1. The honors students observed three significant issues regarding the operation of their system. One, dynamic instabilities were observed during operation. Two, they observed that when the mass was levitating, the input voltage to the PWM chip, v_S, was below the stated region of operation. Three, the frequency of oscillation, f_D, was different from what was expected given the external capacitor, C, connected to the PWM chip.

A significant goal of this thesis is to design a magnetic levitation system that provides the three advantages offered by Marsden's design, without the three disadvantages observed by the honors students. In addition, as discussed in Chapter 1 the system above must levitate the mass in both the attractive and repulsive configurations.

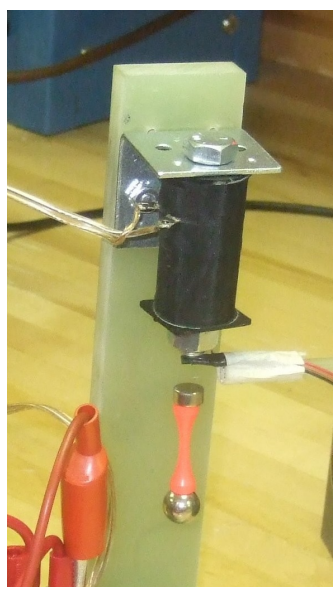

Figure 3.2. Photograph of the Prototype Attractive Levitation System [29]

3.2 Hall Sensor Design

This section will discuss the challenges and constraints associated with using Hall effect sensor technology as it pertains to position sensing of a magnetic mass. Ideally, the Hall

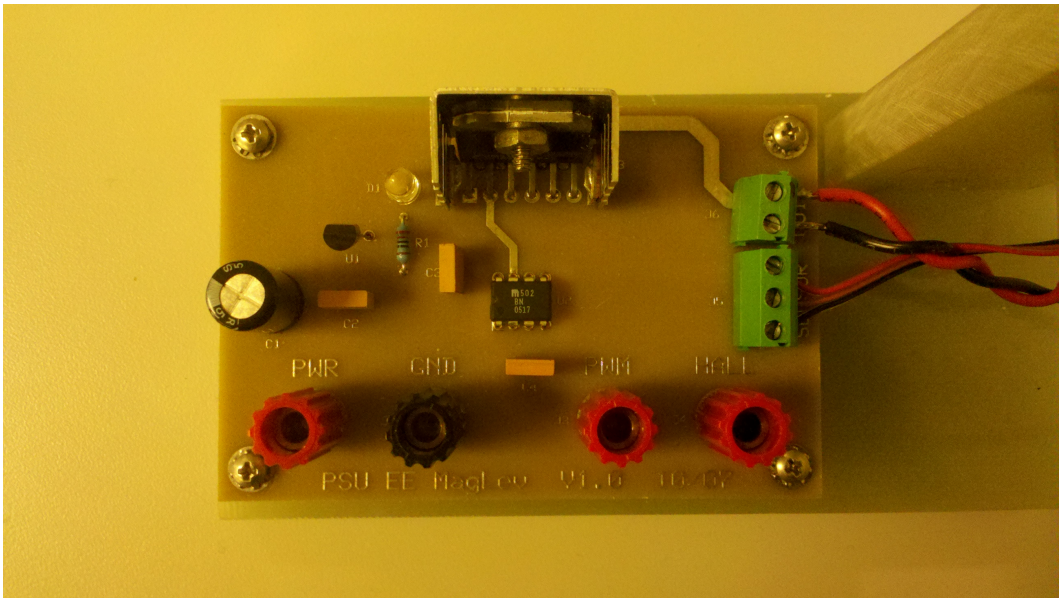

Figure 3.3. Photograph of the Prototype Attractive Levitation System Circuit Board

effect sensor just sees the magnetic field from the permanent magnet, and the output signal can be directly mapped to the position of the mass. However, the Hall effect sensor sees the magnetic field from the permanent magnet and from the electromagnet. Three schemes for overcoming this problem are discussed in Section 3.2.1. This section also discusses the non-linear mapping of the Hall effect sensor signal, v_S, to position of the mass, y. When selecting a Hall effect sensor, it can be seen that there are trade-offs between several of the sensor characteristics. Section 3.2.2 will discuss these trade-offs and discuss the selection of a Hall effect sensor. Section 3.2.3 will discuss sensor glitches that are induced by the dSPACE DAQ system's PWM signal and the sensor conditioning circuitry necessary to minimize their effects.

3.2.1 Candidate Hall Sensor Schemes

While it is desirable to obtain the strength and direction of the magnetic field due only to the position of the magnetic mass, this is not possible. The Hall effect sensor experiences a net magnetic field which is the superposition of the field generated by the electromagnet and the permanent magnet. If the electromagnet field is large in comparison to the permanent magnet field, then the sensor output includes a large error term. The maximum error will

occur when the permanent magnet is furthest away from the sensor and the electromagnet is commanding its largest field. Moving the sensor away from the electromagnet will reduce the error term but will also reduce the sensitivity to the position of the magnetic mass when it is far away from the sensor. Reducing the maximum current through the electromagnet will also reduce the error term but will limit the range of positions in which the mass can be commanded. Another solution is to subtract a corresponding voltage from the Hall effect sensor output based on the expected magnetic field from the electromagnet.

This section details three potential sensor schemes for Hall effect sensor(s) placement in the magnetic levitation system. Figure 3.4 shows all three schemes with approximate Hall sensor locations. Ideal placement of the Hall effect sensor lies along the pole of the magnetic mass. Moving the sensor off-axis will decrease the sensitivity of the sensor to the position of the permanent magnet and will create a non-linear response if the mass has the ability to move through the plane in which the sensor rests. Unfortunately, aligning the Hall effect sensor with the pole of the magnetic mass also aligns the sensor with the pole of the electromagnet. Therefore, there will also be a larger position error due to the field commanded by the electromagnet.

Scheme 1 use two sensors, positioned on opposite ends of the electromagnet. Because the field due to the electromagnet is approximately the same at both of its ends, subtracting the two Hall sensor voltages effectively eliminates the contribution of the electromagnet. That is, the difference signal is primarily due to the position of the permanent magnet. This scheme is the most accurate scheme of the three in which to sense position.

Because the field due to the electromagnet at Hall sensor 1 and 2 are not exactly identical, and the fact that the Hall sensors have different gains and DC offsets, it is necessary to level shift and scale the output of sensor 1. The calibration procedure for Scheme 1 entails first removing the permanent magnet from the system and cycling through the duty cycle of the PWM reference signal. This will allow a comparison between the two sensor output signals. A linear function can be found that maps the output of sensor one to that of sensor two. These two signals can then be scaled and subtracted using either an analog circuit or numerically after both have been sampled. The resulting voltage corresponds to the magnetic field due only to the position of the mass. While this scheme is highly accurate, it incorporates twice the circuitry as needed for one sensor.

Scheme 2 is a one sensor scheme in which the Hall sensor is placed adjacent to the electromagnet and between the electromagnet and the permanent magnet. Unfortunately, this scheme will incorporate a large error term from the field commanded by the electromagnetic. The large position error encountered in this scheme makes this the least viable method available. There is a case where the polarity of the fields from both the mass and the electromagnet will add together when the mass is close to the electromagnet. The sensor will saturate if it is not rated for a range greater than the summation of both of these fields. This will then lead to instabilities due to the feedback of an incorrect position.

Scheme 3 places the sensor directly beyond the largest controllable equilibrium position. This will minimize the error term by moving the sensor as far away as possible from the electromagnet and reduce the likeliness of sensor saturation. Scheme 3 is more accurate than Scheme 2 and more cost-effective than Scheme 1, therefore Scheme 3 has been selected for this use in this magnetic levitation system. Error calibration of Schemes 2 and 3 entail first removing the mass from the system and cycling through the duty cycle of the PWM reference signal, as in Scheme 1. This will generate a data set based on commanded duty cycle that can be used in a lookup table to subtract from the sampled sensor data.

For all of the schemes mentioned, calibration was discussed as pertaining to the removal of the error term from the sensor signal. Position calibration can be executed in order to translate the sensor voltage, v_S, to a position value, y. First the mass is reintroducing to the system and the electromagnet is turned off. Calibrated plastic spacers are then be used to vary the position of the mass while recording the sensor output. As will be shown in Section 3.4.1, this data must entered into a lookup table because of the non-linear mapping between sensor voltage and position.

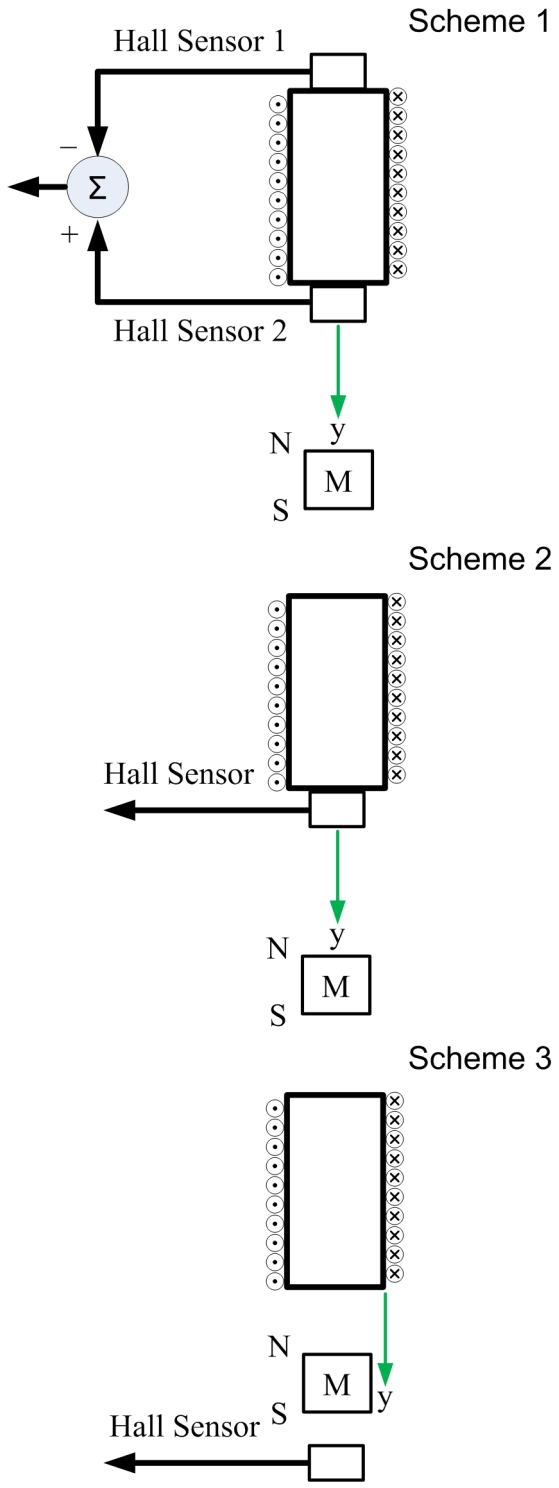

Figure 3.4. Conceptual Models Showing Hall Sensor Schemes

3.2.2 Hall Effect Sensor Selection

Determination of the proper Hall effect sensor to be used in this design should be based upon criteria such as sensor range, sensitivity, the ability to sense the polarity of the field, and the trade-offs between these criteria.

First, a Hall effect sensor should be selected based on the expected maximum magnetic field that will be encountered. Using Scheme 3, the maximum magnetic field will occur when the mass is closest to the sensor and the polarity of the field generated by the electromagnet aligns with that of the permanent magnet. If this maximum field is greater than the sensor range of the device, the Hall effect sensor will saturate and the position of the mass will not be properly reported. Second, a Hall effect sensor should be selected, based on the sensitivity of the device. When the position of the permanent magnet is far away from the sensor, the change in magnetic field due to a change in position will be very small. If the Hall effect sensor has a low sensitivity, positions far from the sensor will not be properly reported. Third, a Hall effect sensor should be selected based on its ability to sense the polarity of the magnetic field. Without the ability to sense the polarity of the magnetic field, the error calibration, discussed in Section 3.2.1, cannot be carried out. Therefore, an error term will be included with the position, based on the field being generated by the electromagnet.

The first trade-off occurs when comparing the sensor range to the sensitivity of the device. The sensitivity of the device is defined as the change in the sensor's output voltage, v_S, due to a change in the magnetic field, β, and can be approximated in terms of the sensor's output voltage range, $v_{S(range)}$, and the sensor range, $\beta_{(range)}$, as

$$\frac{\delta v_S}{\delta \beta} \approx \frac{v_{S(range)}}{\beta_{(range)}}. \tag{3.1}$$

It can be seen that for a fixed output voltage range, an increase in sensing range can be achieved at a cost to the sensitivity of the device. Therefore, selecting a sensor with a large sensor range will reduce the maximum position in which the permanent magnet can be sensed. This trade-off should be considered in order to maximize the range of sensible positions.

The second trade-off occurs when comparing the ability to sense the polarity of the magnetic field to the sensor range of the device. The maximum sensor range of a bipolar sensing device is halved from that of a corresponding unipolar sensor. Therefore, there

is a trade-off between having the ability to correct for errors in the position due to the electromagnet and the ability to sense positions near the sensor.

The surface fields of the permanent magnets detailed in Section 3.3.1 are very large and can saturate many of the available Hall effect sensors on the market. Table 3.1 lists a number of available Hall effect sensors. Of the listed Hall effect sensors, only the MLX90360 has the available sensor range to fully sense the surface field from the permanent magnet. The MLX90360 Hall effect sensor was not chosen for use because it is a surface mount device, it needs to be programmed using a specific programming board before it can be used, and the high cost per device. As an operational note, the sensitivity of the MLX90360 is listed as 12-bits because it can be programmed with up to 5 separate sensing regions and associated gains across the full range of the device.

While the A1360LKTTN is not a surface mount device, it also needs to be programmed, incorporating unnecessary complexity into the system. The SS94A1F and SS494B have excellent sensitivity but their typical sensor range will not work for the magnitude of fields that will be seen. The SS94A1F hall effect sensor is also exorbitantly expensive. Therefore, the SS49E Hall effect sensor was selected for use in this system. The difference between the listed sensor range and the high surface field strength is alleviated by moving the sensor slightly beyond the largest controllable position.

Sensor Model	Chip Type	Output	Typ. Range	Typ. Sens.	Cost
SS94A1F	3-SIP	Analog	±100G	25mV/G	$21.18
SS494B	3-SIP	Analog	±375G	5mV/G	$3.16
SS49E	3-SIP	Analog	±1000G	1.4mV/G	$2.21
A1360LKTTN	4-SIP	Analog	±1575 - ±3150G	0.7- 1.4mV/G	$3.94
MLX90360	8-SOIC	PWM/Analog	±1T	12-bits	$10.92

Table 3.1. Listing of Potential Hall Sensors

3.2.3 Hall Effect Signal Conditioning

A challenge to position sensing, particular to this system, is that the dSPACE DAQ system experiences crosstalk between the PWM output and its analog-to-digital converter (ADC) inputs. A glitch can be seen in the sensor data that corresponds to switching from the PWM signal. The amplitude and frequency of these glitches do not correlate to changes in the

sensor signal and can still be observed on the ADC channel when the sensor is not attached to the DAQ. Fundamentally, this is a signal-to-noise (SNR) issue. If the signal is amplified after being sampled, the amplification will apply to the glitch as well as the signal thereby keeping the SNR value the same as before it was amplified. Therefore, amplification must be accomplished before the sensor signal is sampled. Voltage shifting and amplifying the sensor signal prior to being sampled will maximize the SNR. Figure 3.5 shows the Hall sensor conditioning circuit.

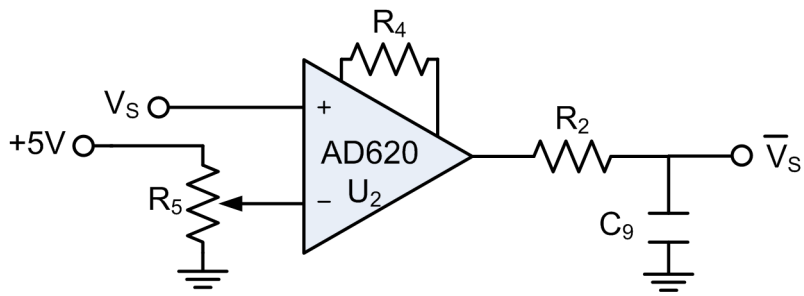

Figure 3.5. Hall Sensor Conditioning Circuit

An AD620 instrumentation amplifier, U_2, is used to provide amplification, where the gain of the amplifier is calculated based upon the sensor's output range and the ADC's input range. The ADC's input range is given by dSPACE as $\pm 10V$. The polarity of the permanent magnet, H-bridge connection to the electromagnet, and the orientation of the Hall effect sensor can potentially change the outcome of the following experiments. Therefore, a few test case are suggested to make sure that the appropriate minimum and maximum values of the Hall effect sensor are found. The sensor's output range can be measured by running the system at both 0% and 100% duty cycle with and without the permanent magnet. When the permanent magnet is in the system, it should be held at both extremes of its range for both duty cycles. The minimum and maximum sensor output values from these experiments will determine the range of the Hall sensor output for all potential cases.

The offset voltage can be found by taking the average of the minimum and maximum output values as

$$v_{s(offset)} = \frac{v_{s(max)} + v_{s(min)}}{2}. \tag{3.2}$$

The offset voltage can then be set by adjusting the potentiometer, R_5. The gain of the instrumentation amplifier can be found by dividing the range of the ADC's input, listed as

±10V, by the experimental range of the Hall sensor. This gain should be reduced to ensure that the instrumentation amplifier never saturates the ADC inputs. Therefore it is more appropriate to determine gain of the instrumentation amplifier as

$$G_2 = \frac{+9V - -9V}{v_{s(max)} - v_{s(min)}}. \tag{3.3}$$

The gain resistor, R_4, is then calculated using the following equation, supplied in the AD620 data sheet, as

$$G_2 = \frac{49.4k\Omega}{R_4} + 1. \tag{3.4}$$

After the amplification, a simple RC low-pass filter is implemented, where the cut-off frequency is set to approximately 1kHz. The mechanical dynamics should be much slower than the 1kHz cut-off frequency therefore this circuit should only filter high frequency noise and act as an anti-aliasing filter before the signal is sampled by the ADC. The conditioned sensor signal, $\bar{v}_S$, is used to generate the position mapping look-table described in Section 3.4.1.

3.3 Overall System Design

In addition to the position sensor, the magnetic levitation system has other subsystems that must be designed. Section 3.3.1 describes the need for the guide rail, the selection of the permanent magnet, and the selection of the guide rail materials and geometry. Section 3.3.2 discusses the selection of the electromagnet and its core material. Finally, Section 3.3.3 discusses the design of the electronic circuitry for the interface to the dSPACE DAQ system.

3.3.1 Guide Rail and Permanent Magnet Selection

In this section, the need for a guide rail and permanent magnet and their selection will be discussed. If the mass moves in-plane, off of the axis in which the Hall effect sensor is measuring, the net magnetic field that is sensed will change. This will translate as a change in position to the control system and can cause instabilities during operation. Other potential

undesirable movements also include in-plane rotational movement and rocking movement about the desired operating point. Both of these movements will cause a change in the net magnetic field.

A solution to this problem is to mechanically limit the range of motion of the magnetic mass by using a guide rail. The selection of the guide rail is of interest because the guide rail constrains and stabilizes the mass and introduces a damping element into the system dynamics through friction. As the guide rail selection is primarily influenced by the choice of a permanent magnet, the criteria for the selection of a permanent magnet are first considered. Once the magnet has been chosen, the criteria for the guide rail will be considered.

The first criteria for the selection of a permanent magnet is that it must be able to be levitated by the electromagnet in both the attractive and repulsive configurations. The second criteria is that it must be able to be sensed by the Hall effect sensor along the complete range of its controllable positions. The third criteria is that it must be able to slide on a guide rail in order to maintain its axial position. The first and second criteria can be met through a light weight magnetic mass that has a high surface magnetic field strength. The third selection criteria can be met by choosing an axially-magnetized ring magnet to ride around the guide rail.

Table 3.2 lists the ring magnets that were chosen for experimentation from K & J Magnetics. All of the listed magnets are neodymium, plated in a three layer Nickel-Copper-Nickel coating. The pull force is defined as the force generated between the magnet and a "properly sized" steel plate in laboratory conditions. The "proper size" of a plate depends on the field strength and geometry of the magnet, therefore this value should only be used for a general comparison of similar sized magnets. The manufacturer does not list surface field strengths for ring magnets, but an approximation can be found by considering the field strengths of their solid cylindrical versions and the differences between their pull force ratings shown in Table 3.3.

Ring Magnet	O.D.	I.D.	Thickness	Pull Force
R848	0.50"	0.250"	0.50"	11.33 lbs
RC48	0.75"	0.250"	0.50"	25.88 lbs
RC44	0.75"	0.250"	0.25"	17.61 lbs
RX068	1.00"	0.375"	0.50"	39.62 lbs

Table 3.2. Listing of Experimental Ring Magnets

Solid Version	Surface Field	Pull Force
D88	5903 Gauss	14.60 lbs
DC8	5280 Gauss	27.60 lbs
DC4	3661 Gauss	18.82 lbs
DX08	4667 Gauss	44.00 lbs

Table 3.3. Listing of Corresponding Cylindrical Magnets

The magnets in Table 3.2 were chosen primarily upon the available inner diameter (I.D.) and the thickness characteristics. The guide rail needs to be anchored into the electromagnet in order to properly align the magnet, therefore the inner diameter of the magnet must be smaller or equal to the diameter of the core of the electromagnet. It was determined that 3/8in was the maximum size that K & J Magnetic carried that would work, given this condition. The thickness of the magnet helps determine how far the magnetic field is projected but can also take away from the visual sensation of movement along the guide rail. A thickness of 1/2in was selected as a maximum value considering these criteria.

The maximum controllable range observed while running the system open-loop in a repulsive levitation configuration was the determining factor for the selection of the magnet to be used from those in Table 3.2. The RX068 was primarily disqualified due to its large field strength. Though the RX068 had a very large maximum controllable position, whenever the mass came close to the surface of the electromagnet, it would be unable to move away due to its interaction with the ferromagnetic core, reducing its viable range. The RC44 was disqualified due to having the smallest controllable range. While both the RC48 and R848 had similar maximum controllable positions, the electromagnet was able to push the R848 away from its surface with less effort. Therefore, the R848 was chosen as the best case permanent magnet to be used in this system.

Having selected the mass, the selection of the guide rail can now be considered. The first criteria for selection of the guide rail is to keep the movement of the mass restricted to the y-axis, in-line with the Hall effect sensor and the electromagnet. The second criteria is to allow the mass to move freely on the y-axis as commanded by the system. The third criteria is to keep the mass from flipping or rocking. Various guide rail geometries, sizes, and materials are examined using these three criteria.

Only square and cylindrical rail geometries are available for consideration for a magnet with a 1/4in inner diameter. Square rail dimensions are defined along the face of the

rail, therefore the inner diameter of the R848 is too small for a 1/4in square rail to fit through. Choosing a square rail with a smaller dimension allows the magnet to rock and bind intermittently against the rail. This behaviour precludes the use of a square guide rail, leaving only a cylindrical geometry.

While the R848 is specified as having 1/4in inner diameter, imperfections in the coating decrease this value slightly. Gentle sanding and polishing of any 1/4in diameter guide rail is necessary for the proper installation of the magnet. Choosing the next smaller sized diameter cylindrical guide rail allows the magnet to rock and intermittently bind as found with the smaller square guide rails. Therefore, only 1/4in diameter guide rails can be chosen. It should be noted that polishing is necessary as a rough guide rail surface will increase friction and can also cause the magnet to bind.

Materials plays a very important role in the selection of the guide rail as the coefficient of friction is a material property. If the magnet encounters too much friction, it will bind when the net force acting on the mass becomes small. How small this force has to be before binding occurs is directly related to the coefficient of friction. Copper, oil impregnated brass, G10, and teflon were all tested as viable materials for the guide rail. Teflon is the best choice as it has the smallest coefficient of friction of the available test materials. At 1/4in in diameter, a teflon cylindrical rod is firm enough to keep the magnet centered. Visual observation of the performance of these materials confirms that the teflon guide rail is indeed the best material.

It should be noted that the 1/4in teflon guide rail still needs to be sanded and polished to fit inside the ring magnet. Steel wool can be used to polish the teflon rail before use, but care must be taken to remove all of the steel particles as they will cause the magnet to bind. The process of sanding causes physical irregularities in the surface of the teflon rail, which are reduced but still present after polishing. These irregularities induce a non-linear change in friction over the length of the rail which can be modelled as static friction. This effect is observed as small incremental steps in the sensor output when the mass slows near a reference position that it is tracking or binding of the mass near that desired reference position.

3.3.2 Electromagnet Selection

In this section, the selection of an electromagnet coil and its core are discussed. This selection is of interest because the coil and core material directly affects the controllable range of the permanent magnet and helps set the mechanical and electrical dynamics of the system. The design objectives of the electromagnet's coil are first used as criteria in the selection process. The design objectives of the electromagnet's core are then discussed and used to determine the proper material, geometry, and positioning for use in this system.

Before addressing the selection criteria, a short discussion should be held on whether is better to build or buy an electromagnetic coil. Building a simple coil can be easily accomplished, but it takes time and perseverance to build a compact coil with a large number of turns. If the goal is to build a number of magnetic levitation systems, it is easier to buy an off-the-shelf product. Many of the commercially available electromagnets on the market are expensive or their design is of limited usefulness due to having very specific power restrictions. An alternative solution is to buy a solenoid. Solenoids are electromechanical switching devices that use an electromagnetic coil to magnetize and move an armature inside the solenoid. Solenoid manufacturers usually have many available models with different power ratings in which to choose from. Therefore searching for a solenoid is an ideal approach to finding an appropriate electromagnet.

There are two criteria to be considered for the selection of the coil. First, the coil must be selected such that the power dissipated is less than or equal to the power rating of the coil. The first criteria can be satisfied by considering the maximum voltage in which the electromagnet will be driven, v_{Lmax}, and the DC resistance of the coil, R_L. For reason of safety and reliability, a coil should be selected that has a larger power rating than what will be dissipated. Of these solenoids, selecting a solenoid with the smallest DC resistance will ensure that the selected coil is one that has the maximum possible coil current, i_L, of those available. As the force of electric origin, f^e, is directly proportional to the current through the coil, i_L, selecting a coil that allows more current to flow will increase the range in which mass can be controlled.

The second criteria is that the coil must be able to be run for long periods of time. Selecting a device using only the first criteria may still lead to the device breaking down over time as many solenoids are only rated for intermittent or pulsed operation. The power

ratings for these devices only apply for the short operation time, after which they need to turned off before being used again. Constant use of these solenoids will cause them to break down over time and should not be considered for use in an electromagnetic levitation system. Therefore, a solenoid should only be selected if it is rated for continuous use. If a solenoid is selected with a smaller power rating than what is being dissipated or if it is not rated for continuous use, then the electromagnet will over-heat, potentially melting the insulation and short circuiting the electromagnet. The casing in which the device is mounted may also break down over time due to over-heating.

Initially the system design incorporated a 12V DC solenoid manufactured by KGS. After two years of use, the plastic casing failed and the electromagnet unwound. As the model number was not registered on the KGS website, a comparison was made between the DC resistance of the solenoid, ($R_L \approx 15\Omega$), and its counterparts in the KGS catalog. It was seen that all of the 12V DC solenoids with a DC resistance of 14.4Ω were pulsed operation solenoids. It was concluded that a new coil would have to be selected.

The coil chosen for this design was purchased from McMaster-Carr and is manufactured by an OEM manufacturer, Magnet Schultz of America. Model S-06683 is a 12V DC continuous solenoid with a power rating of 11Watts and a DC resistance of 13.1Ω. The H-bridge drives the S-06683 with 12V, therefore the 11Watt power rating is boundary-line acceptable. Later a large aluminium heat sink is attached to help dissipate the heat generated during operation. Magnet Schultz of America manufactures several other solenoids with increased power ratings, but were unavailable at the time of purchase.

There are four criteria for the selection of the core. First, the core material must be able to focus the electromagnetic field generated by the coil. In order to focus the field, the core material must have a high permeability, which is found in ferromagnetic materials. Second, the core material must not permanently magnetize after being in the field of the coil. If the core can partially magnetize in a field, it will keep the polarity of the magnetic field in which it was formed, even after the polarity of the field generated by the electromagnet changes direction. This can complicate the system as an additional force acting on the mass must then be modeled. The first two criteria led to soft-iron being chosen as the material to be used for the core of the electromagnet. Soft-iron is frequently used in electromagnet applications as it is ferromagnetic, has a high relative permeability, and can easily changes magnetic polarity. Therefore it will not polarize if left in a magnetic field for long periods of

time and will focus the magnetic field generated by the coil.

The third criteria is that the electromagnet must be able to control the mass when it nears the electromagnet. Therefore, the force between the core and the permanent magnet must be smaller than the force of electric origin. It was found that the force between the core and the permanent magnet was larger than what the electromagnet could oppose if the core was positioned flush with face of the electromagnet. Recessing the core a 1/4in into the electromagnet decreased this force such that the electromagnet could regain full control over the mass. The fourth criteria is that the core must be able to anchor the guide rail. This criteria was achieved by having a machinist drill a 1/4in diameter hole centered on the core, 1/4in deep into the core material. The teflon guide rail was then able to fit snugly into electromagnet.

3.3.3 Data Acquisition Interface

In this section the data acquisition interface and the current sensor circuitry will be discussed. The dSPACE CLP1104 DAQ system is used to sample the conditioned sensor data as well as to provide a PWM reference signal to the H-bridge. Two 16-bit multiplexed ADC's are used to sample the sensor data at a 10kHz sampling rate. These multiplexed ADC's have a $2\mu s$ conversion time, therefore there is a only a short delay between sampling of the Hall effect sensor and of the current sensor. Several 12-bit parallel ADC's are also available but were not used due to the decrease in the number of bits that could be used to sense the position of the mass and of the current. Figure 3.6 shows the block diagram model of the ADC inputs which have approximately 1MΩ of input resistance, thereby minimizing loading effects. The PWM signal is generated from a slave DSP subsystem that uses a Texas Instruments TMS320F240 DSP chip and is directly applied to the direction input of the H-bridge. The ADC's and the PWM output are set-up through Simulink before they are compiled and loaded onto the dSPACE system. The PWM output can be set with a frequency separate from the sampling frequency of the ADC's as long as the period of the PWM signal is an integer multiple of the sampling period.

Current sensing circuitry has been implemented in order to allow the student to design a controller using full-state feedback. Shown in Figure 3.7, a small 0.1Ω resistor, R_6, specifically designed for current sensing, is placed in series with the electromagnet. This resistor was

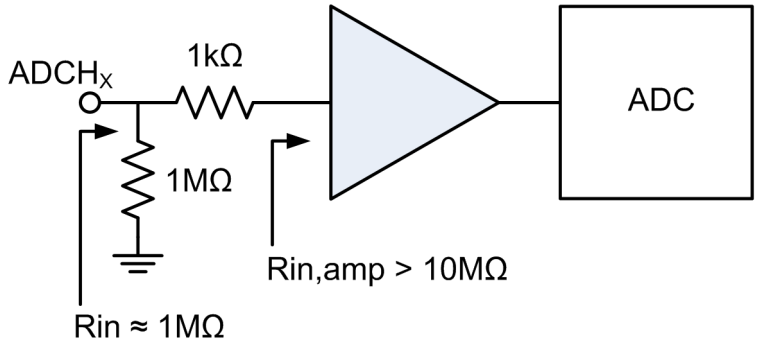

Figure 3.6. dSPACE ADC Circuit

chosen small so that it would have minimal effect on the maximum current. The expected error in the current from the addition of the current resistor can be calculated using the DC resistance of the coil, $R_L = 13.1\Omega$, as

$$\begin{aligned} Err &= 100\% \frac{\frac{12V}{R_L + R_5} - \frac{12V}{R_L}}{\frac{12V}{R_L}} \\ &= -0.7576\%. \end{aligned} \tag{3.5}$$

The current resistor is connected to the differential input of an AD620 instrumentation amplifier, U_1, which then amplifies the value of the voltage drop across the resistor, R_6. The gain of the instrumentation amplifier is calculated based on the input range of the ADC, $\pm 10V$, and the expected maximum voltage drop across the current resistor. The maximum expected voltage drop across the current resistor, R_6, is calculated as

$$\begin{aligned} V_{R5(max)} &= \pm \frac{R_5}{R_L + R_5} 12V \\ &= \pm 0.0909V. \end{aligned} \tag{3.6}$$

The gain was chosen as, $G_1 = 100V/V$, such that the maximum output of the AD620 instrumentation amplifier, U_1, is within the ability of the ADC to sample without saturating. The gain resistor, R_3, can be calculated used the following equation, supplied in the data

sheet as

$$G_1 = \frac{49.4k\Omega}{R_3} + 1. \tag{3.7}$$

Solving for R_3,

$$R_3 = 499\Omega. \tag{3.8}$$

It should be noted that the instrumentation amplifiers cannot use the +12V supply that the electromagnet uses, due to the input range of the AD620. As one side of the current sensing resistor is tied to the H-bridge, it will switch periodically between 0 and +12V. The AD620 instrumentation amplifiers' typical input range is rated as

$$V_{in} = -V_{supply} + 1.9V \text{ to } + V_{supply} - 1.2V. \tag{3.9}$$

Therefore the instrumentation amplifier must have, at minimum, a supply voltage of $\pm 13.2V$ as it cannot be run single-ended. Separate ±15V power supplies power both instrumentation amplifiers.

Figure 3.7 shows that the amplified current signal is passed through a simple RC low-pass filter, (R_1 and C_4), used for anti-aliasing and noise attenuation. This filter has been added to the circuit board layout but has not yet been implemented. The value of the cut-off frequency should be chosen such that the electrical dynamics are not attenuated. This is discussed further in Chapter 5.

3.4 Experimental Measurements

In this section, experimental measurements necessary for position sensing and current will be discussed. Section 3.4.1 details the experimental position sensor measurements that are necessary for generating the error calibration and position look-up tables detailed in Section 3.2.1. Section 3.4.2 discusses the experimental measurements necessary for the mapping of the current sensor output to the actual current value.

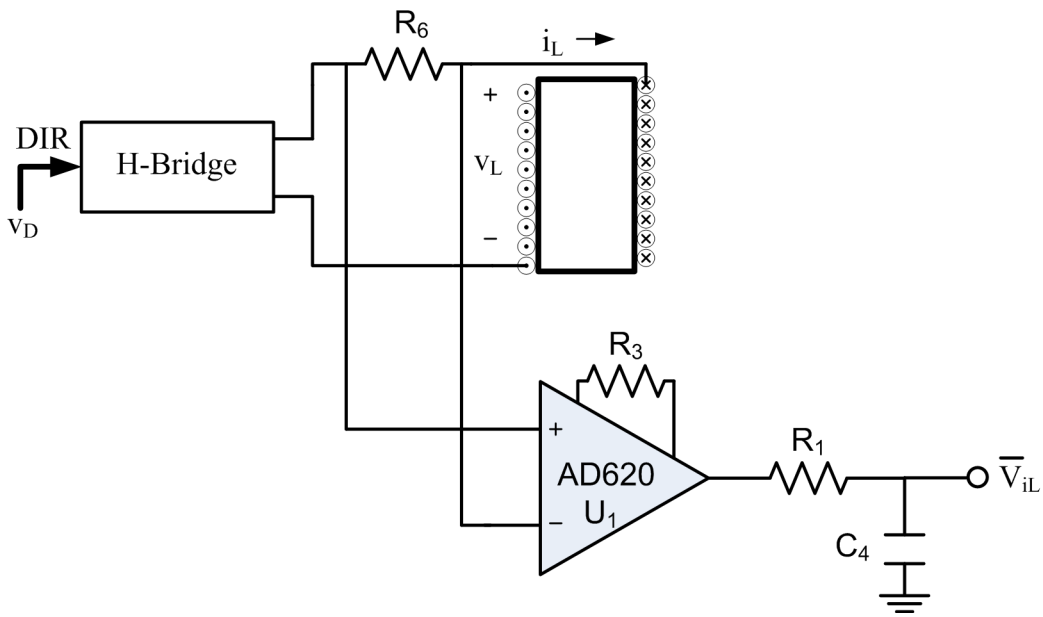

Figure 3.7. Current Sensing Circuit

3.4.1 Position Sensor Calibration

In this section, the error calibration and position look-up table experiments that were discussed in Section 3.2.1 are investigated in detail. The error calibration and position look-up tables can be made independently of each other. Both data sets are composed of time-averaged conditioned Hall sensor data where the magnetic field sensed from the electromagnet is dependent on duty cycle, $\beta_E(D)$, and the magnetic field sensed from the permanent magnet is dependent on position, $\beta_M(y)$. When the system is operating the net magnetic field superimposes linearly such that

$$\beta_{net} = \beta_E(D) + \beta_M(y). \tag{3.10}$$

The Hall sensor maps this net magnetic field to voltage as a linear function

$$\begin{aligned} v_S &= m\beta_{net} + b, \\ &= m\beta_E(D) + m\beta_M(y) + b. \end{aligned} \tag{3.11}$$

The voltage representing position can be written as

$$v_{pos} = m\beta_M(y) + b, \tag{3.12}$$

where $\beta_M(y)$ is a non-linear function of y. The voltage that represents the error term can be written as

$$v_{err} = m\beta_E(D), \tag{3.13}$$

where $\beta_E(D)$ is a linear function of D. Equation 3.11 can be re-written in terms of the error term and the position term as,

$$v_S = v_{err} + v_{pos}. \tag{3.14}$$

In order to create the error calibration look-up table, the magnetic mass must first be removed from the system. A Simulink model is created that incorporates the PWM driver and the ADC input from the conditioned Hall sensor output, $\bar{v}_S$. In this instance, a MATLAB M file was written to save five seconds of conditioned Hall sensor data, then automatically incremented the duty cycle in 1% increments from 0% to 100%. The error term can only be evaluated if the mean of the signal is removed, therefore the data from the error calibration table is de-trended by a constant.

This data set is of the form

$$\delta v_S(D) = \bar{m}D + \bar{b}, \tag{3.15}$$

where $\delta v_S(D)$ represents the de-trended measured voltage as a function of duty cycle, D, and $\bar{m}$ and $\bar{b}$ are unknown parameters to be determined. The data from this process is shown in Figure 3.8, where $\bar{m} = 9.25 * 10^{-3}$ and $\bar{b} = -0.473$. This mapping is linear, therefore a look-up table is not necessary in which to implement this function.

In order to create the position look-up table, the electromagnet is turned off and the permanent magnet is placed into the system. Calibrated plastic spacers are used to accurately vary the position of the mass, y, while recording the sensor output value, $v_S(y)$. This data

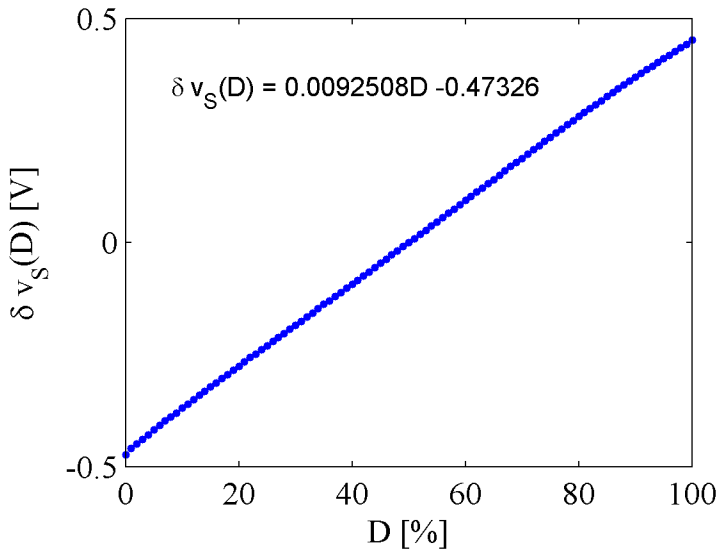

Figure 3.8. Hall Sensor Error Term Versus Duty Cycle

set is of the form

$$v_S(y) = m\beta_M(y) + b. \tag{3.16}$$

The data from this process is shown in Figure 3.9. It can be seen that this data is highly non-linear thus it needs a look-up table in order to effectively map the voltage, $v_S(y)$, to a position, y.

While the error calibration and position look-up tables are extremely useful, they come at a cost of increasing the number of instructions that must evaluated each sampling period, effectively reducing the maximum sampling frequency. It should be noted that using the current value of the duty cycle will create an algebraic loop in the instruction set, therefore only the previous value of the duty cycle can be used to evaluate the error calibration look-up table. If the sampling period of the control system is very fast in comparison to the dynamics of plant, then this should not be a problem.

3.4.2 Current Sensor Calibration

In this section the proper procedure for current sensor calibration will be discussed. While this experiment was not completed, it is relatively straight forward procedure. A Simulink model

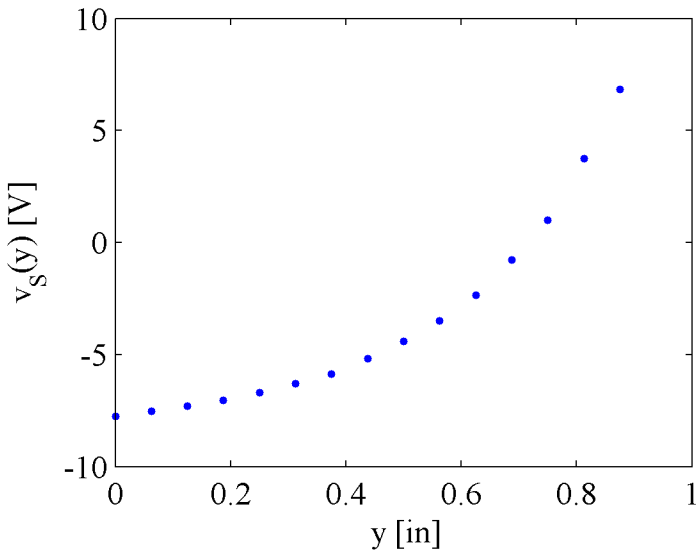

Figure 3.9. Hall Sensor Output Versus Position

must be made that incorporates the PWM driver and the ADC input from the conditioned current sensor output, $\bar{v}_{iL}$. Two other 16-bit ADC channels should be used take a differential voltage reading across the current resistor, R_6. The duty cycle should then be incremented from 0% to 100%, each step recording several seconds of time data for each signal.

Off-line, the mean of each of the data sets should be taken in order to remove some of the noise from the data. The time-averaged differential voltage value can then be divided by the value of the resistor, R_6, to determine the current for each step in duty cycle. A comparison can then be made between the calculated current value, i_L, and the current sensor output, v_{iL}. A linear relationship can be found such that

$$i_L = m_i v_{iL} + b_i. \tag{3.17}$$

Chapter 4

Levitation using Hall Sensing

This chapter details the design of feedback compensators for regulating the position of the permanent magnet in the test-bed descibed in Chapter 3. Section 4.1 discusses the overall functional block diagram representation of the system that applies for both the repulsive and attractive models. Structural similarities include the PWM and H-Bridge subsystem, Hall effect sensor subsystem, and the digital voltage-to-position mapping subsystem. The conceptual system structure is then used to derive a small-signal block diagram of the system. Section 4.2 shows that the non-linear system equations for the test-bed operating in attractive and repulsive suspension modes are similar. As such, their linearized state-space models are derived side-by-side. Sections 4.3 and 4.4 detail the system identification, compensator design, and experimental verification of the repulsive and attractive suspension system, respectively.

4.1 General System Structure and Model

This section discusses system characteristics that apply to both the repulsive and attractive suspension modes. First, the generalized representation of the closed-loop system from the actuator input, $u(t)$, to the estimated value for the position, $\bar{y}$ will be discussed and modeled. Second, this section presents the overall functional system representation. Finally, a small-signal block diagram is presented based on the functional system representation.

The magnetic suspension test-bed is modeled as a SISO system whose input $u(t)$ deter-

mines the average current in the electromagnet while y represents the distance between the electromagnet and the permanent magnet. The actuator input, $u(t)$, is bounded between -1 and +1. It is necessary to first map the value of the input to the duty cycle, D, of the PWM system to determine the average current in the electromagnet. Figure 4.1 shows the functional block diagram of the transformation of the actuator input, $u(t)$, to duty cycle, D. The input $u = -1$ maps to a duty cycle of 0(0%), while the input $u = +1$ maps to a duty cycle of 1(100%). A controller can potentially be designed that destabilizes the system, therefore the limiter is placed to ensure that the commanded duty cycle will always remain between 0% to 100%.

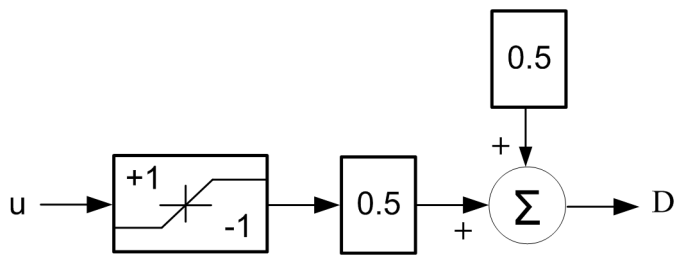

Figure 4.1. Functional Representation of the Transformation of the Actuator Input to Duty Cycle

As a second step, recall that the H-bridge sets the voltage across the electromagnet to either $+V_{Lmax}$ or $-V_{Lmax}$, where $V_{Lmax} = 12$VDC is the supply voltage. The average voltage across the electromagnet is

$$\begin{aligned} v_{Lavg} &= V_{Lmax}D - V_{Lmax}(1 - D) \\ &= 2V_{Lmax}D - V_{Lmax}, \end{aligned} \tag{4.1}$$

where the duty cycle, D, varies from 0(0%) to 1(100%). Figure 4.2 shows the PWM and H-bridge functional block diagram as a gain and an offset.

As was discussed in Chapter 3 Section 3.4.1, the net magnetic field β_{net}, seen by the Hall effect sensor, can be represented as the summation of two separate magnetic fields. The first field is due to the electromagnet and can be represented as a linear function of duty cycle, $\beta_E(D)$. The second field is due to the permanent magnet and is a non-linear function of the position of the magnetic mass, $\beta_M(y)$. The block diagram shown in Figure 4.3 represents the summation of these two fields and is used to define the input to the Hall sensor subsystem.

As discussed in Section 3.4.1, the Hall sensor linearly maps the net magnetic field, β_{net},

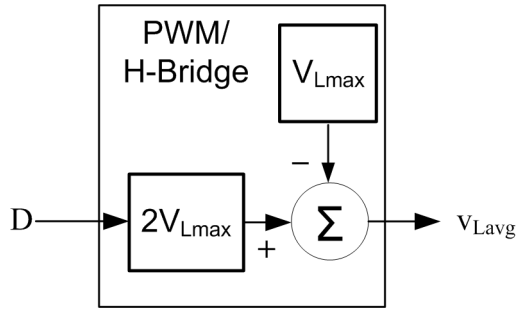

Figure 4.2. Functional Representation of the PWM to H-Bridge Subsystem

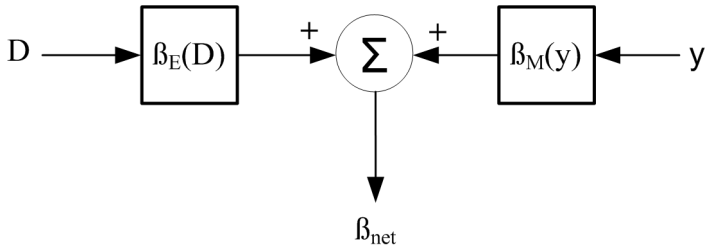

Figure 4.3. Functional Representation of the Net Magnetic Field

to a voltage, v_S. This equation incorporates the voltage offset and gain intrinsic to the Hall sensor with the voltage offset and gain of the signal conditioning circuitry that was discussed in Section 3.2.3. Figure 4.4 shows the linear mapping of the net magnetic field, β_{net}, to the conditioned sensor voltage, $\bar{v}_S$, as represented by an overall sensor gain term, m, an overall offset voltage value, b, and a low-pass filter block.

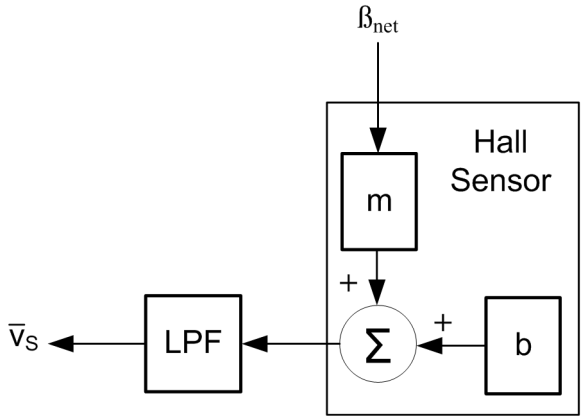

Figure 4.4. Functional Representation of the Hall Sensor System

Following the error calibration and position look-up procedures detailed in Section 3.2.1, the corresponding data sets are entered into two look-up tables. The value of the duty cycle,

D, that is used to look up the error voltage term, v_{err}, is delayed for one sampling period to avoid an algebraic loop. The error voltage term, v_{err}, is then subtracted from the sampled Hall sensor data, $\bar{v}_S$, to define the position voltage term, v_{pos}. The position voltage term is mapped to position using the non-linear position look-up table. Figure 4.5 details the topology of the calibration and look-up estimation system.

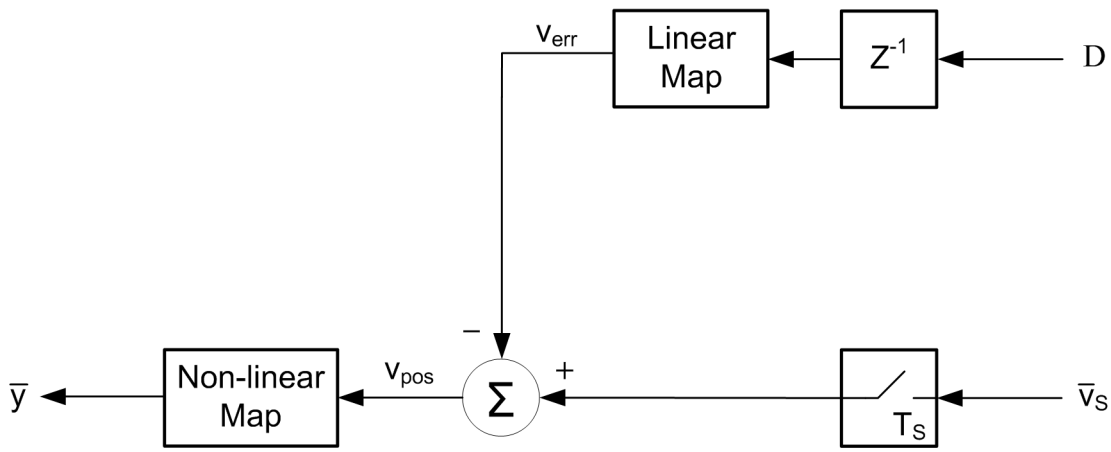

Figure 4.5. Functional Representation of the Position Estimation System

The full functional closed-loop system representation, shown in Figure 4.6, includes a compensator block, G_C, and the plant, G_P. If the position estimation system is treated as close to ideal, an estimation block with a gain of 1 is used to represent the feedback dynamics between the actual position and the approximate value. Figure 4.7 details the small-signal block diagram based on treating the estimation block as ideal.

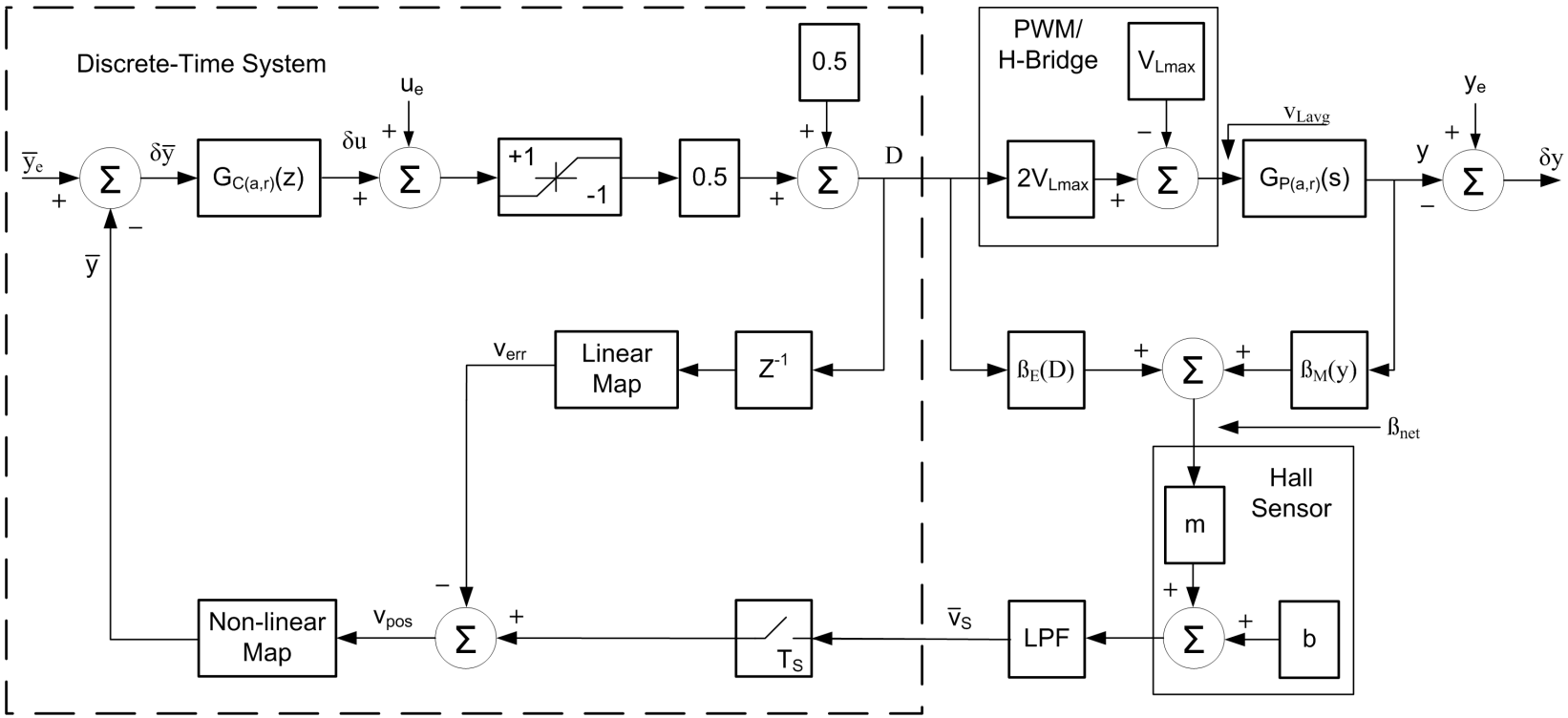

Figure 4.6. Functional System Representation for Either Repulsive or Attractive Operation

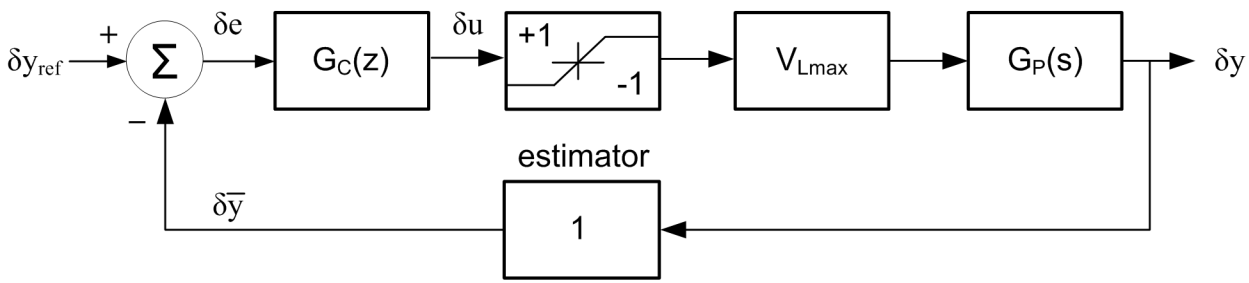

Figure 4.7. Small-Signal Model for Either Repulsive or Attractive Operation with Controller

4.2 System Dynamics

In this section the non-linear dynamics and linearized state-space models will be derived for the test-bed operating in repulsive and attractive suspension modes. It will be shown that the linearized models differ only by a sign in two of the entries to their state-space A-matrices. This analysis is based upon several assumptions. First, that the force of electric origin, f^e, is similar to one developed by the ECP Model 730 MagLev Apparatus which uses a disk magnet and a pancake coil. Second, the equation that defines the inductance of the electromagnet is the same as was in Equation 2.3. Third, the interaction between the permanent magnet and the core of the electromagnet will be small enough to neglect at the operating point.

As with the electromagnetic system analysed in Chapter 2, the dynamics of the system developed in Chapter 3 are composed of three parts. The first is a mechanical equation given by Newton's second law that describes the relationship between the position of the permanent magnet to the forces acting on the magnetic mass. The second is an electromechanical equation that describes the relationship between the current through the electromagnet to the force of electric origin acting on the permanent magnet. The third equation is an electrical equation that describes the relationship between the actuator input to the current through the electromagnet.

Applying Newton's second law to the free body diagram shown in Figure 4.8 for the repulsive configuration, shows that

$$M\ddot{y} = -f_g + f^e(y, i_L) - c\dot{y}, \tag{4.2}$$

where M is the mass of the permanent magnet, f_g is the force of gravity, $f^e(y, i_L)$ is the force of electric origin, and c is the damping coefficient between the permanent magnet and the guide rail. Another force can be considered due to the interaction of the permanent magnet and the ferromagnetic core, f_{mc}, but this is ignored as the operating point will later be chosen away from the surface of the electromagnet. Applying Newton's second law to the free body diagram shown in Figure 4.9 for the attractive configuration, shows that

$$M\ddot{y} = f_g - f^e(y, i_L) - c\dot{y}. \tag{4.3}$$

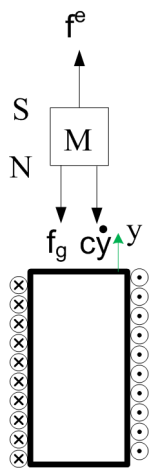

Figure 4.8. Free Body Diagram of the Designed System Operating in the Repulsive Configuration

The equation for the force of electric origin between the electromagnet and the permanent magnet for this system is not known, though an approximation is found using the data sheet from the ECP Model 730 MagLev Apparatus which uses a disk magnet and a pancake coil. The force of electric origin is represented as,

$$f^e(y, i_L) = \frac{i_L k}{(a+y)^N}, \tag{4.4}$$

where $N \approx 4$ for the ECP system.

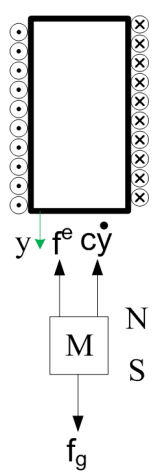

Figure 4.9. Free Body Diagram of the Designed System Operating in the Attractive Configuration

It is seen that substituting Equation 4.4 into Equations 4.2 and 4.3 yields

$$M\ddot{y} = -Mg + \frac{i_L k}{(a+y)^N} - c\dot{y} \tag{4.5}$$

and

$$M\ddot{y} = Mg - \frac{i_L k}{(a+y)^N} - c\dot{y}, \tag{4.6}$$

respectively.

The relationship between the actuator input, u, and the average electromagnet voltage, v_{Lavg}, is defined as,

$$v_{Lavg} = V_{Lmax} u, \tag{4.7}$$

where V_{Lmax}, is the 12V DC supply voltage. The average current of the electromagnet, i_{Lavg}, can then be defined in terms of the average coil voltage, v_{Lavg}, as

$$v_{Lavg} = R_L i_{Lavg} + \frac{dL(y) i_{Lavg}}{dt}. \tag{4.8}$$

Substituting Equations 2.3 and 4.7 into Equation 4.8 and solving for di_L/dt yields

$$\frac{di_L}{dt} = \frac{(a+y)}{L_i(a+y) + aL_o)} \left[V_{Lmax} u - R_L i_{Lavg} + \frac{aL_o \dot{y}}{(a+y)^2} i_{Lavg} \right]. \tag{4.9}$$

A non-linear state-space model representation is obtained for both repulsive and attractive modes by using the state variables $x_1 = y$, $x_2 = \dot{y}$, and $x_3 = i_{Lavg}$ to define the state-space equations. The non-linear repulsive state-space equations are defined as

$$\dot{x}_1 = f_1(x_1, x_2, x_3, u) = x_2 \tag{4.10}$$

$$\dot{x}_2 = f_2(x_1, x_2, x_3, u) = -g + \frac{x_3 k}{M(a+x_1)^N} - \frac{c}{M} x_2 \tag{4.11}$$

$$\dot{x}_3 = f_3(x_1, x_2, x_3, u) = \frac{(a+x_1)}{L_i(a+x_1) + aL_o)} \left[V_{Lmax} u - R_L x_3 + \frac{aL_o x_2}{(a+x_1)^2} x_3 \right] \tag{4.12}$$

$$y = g(x_1, x_2, x_3, u) \ = x_1. \tag{4.13}$$

For a constant input, u_e, the static equilibrium state satisfies

$$f_1(x_1^e, x_2^e, x_3^e, u_e) = x_2^e = 0 \tag{4.14}$$

$$f_2(x_1^e, x_2^e, x_3^e, u_e) = -g + \frac{x_3^e k}{M(a + x_1^e)^N} - \frac{c}{M} x_2^e = 0 \tag{4.15}$$

$$f_3(x_1^e, x_2^e, x_3^e, u_e) = \frac{(a + x_1^e)}{L_i(a + x_1^e) + aL_o)} \left[V_{Lmax} u_e - R_L x_3^e + \frac{aL_o x_2^e}{(a + x_1^e)^2} x_3^e \right] = 0. \tag{4.16}$$

The non-linear attractive state-space equations are defined as

$$\dot{x}_1 = f_1(x_1, x_2, x_3, u) = x_2 \tag{4.17}$$

$$\dot{x}_2 = f_2(x_1, x_2, x_3, u) = g - \frac{x_3 k}{M(a + x_1)^N} - \frac{c}{M} x_2 \tag{4.18}$$

$$\dot{x}_3 = f_3(x_1, x_2, x_3, u) = \frac{(a + x_1)}{L_i(a + x_1) + aL_o)} \left[V_{Lmax} u - R_L x_3 + \frac{aL_o x_2}{(a + x_1)^2} x_3 \right] \tag{4.19}$$

$$y = g(x_1, x_2, x_3, u) \ = x_1. \tag{4.20}$$

For a constant input, u_e, the static equilibrium state satisfies

$$f_1(x_1^e, x_2^e, x_3^e, u_e) = x_2^e = 0 \tag{4.21}$$

$$f_2(x_1^e, x_2^e, x_3^e, u_e) = g - \frac{x_3^e k}{M(a + x_1^e)^N} - \frac{c}{M} x_2^e = 0 \tag{4.22}$$

$$f_3(x_1^e, x_2^e, x_3^e, u_e) = \frac{(a + x_1^e)}{L_i(a + x_1^e) + aL_o)} \left[V_{Lmax} u_e - R_L x_3^e + \frac{aL_o x_2^e}{(a + x_1^e)^2} x_3^e \right] = 0. \tag{4.23}$$

Solving for the static equilibrium state for both sets of equations leads to the same linear relationship between x_1^e, x_3^e, and u_e. These relationships are simplified based on the restriction that the static equilibrium position, x_1^e, must be non-negative. The solutions for the equilibrium state values for both systems are

$$x_1^e = \left[\frac{V_{Lmax}}{R_L} \frac{k}{Mg} u_e \right]^{\frac{1}{N}} - a \tag{4.24}$$

$$x_2^e = 0 \tag{4.25}$$

$$x_3^e = \frac{Mg}{k}(a + x_1^e)^N = \frac{V_{Lmax}}{R_L} u_e. \tag{4.26}$$

The value of the equilibrium input, u_e, can be defined in terms of the value of the equilibrium position, x_1^e, as

$$u_e = \frac{Mg}{k}\frac{R_L}{V_{Lmax}}(a + x_1^e)^N. \tag{4.27}$$

It is also convenient to restate the inductance of the electromagnet when the permanent magnet is located at the equilibrium position,

$$L_e = \frac{L_i(a + x_1^e) + aL_o}{(a + x_1^e)}. \tag{4.28}$$

The linearized state-space A-matrix is found by taking the Jacobian of the state equations with respect to the state variables and evaluating the result with the static equilibrium states. Similarly, taking the Jacobian of the state equations with respect to the actuator input, u, leads to the B-matrix. The resulting linearized state space model are listed. The repulsive system linearized state-space model is

$$\begin{bmatrix} \delta\dot{x}_1 \\ \delta\dot{x}_2 \\ \delta\dot{x}_3 \end{bmatrix} = \begin{bmatrix} 0 & 1 & 0 \\ -\dfrac{kNx_3^e}{M(a + x_1^e)^{N+1}} & -\dfrac{c}{M} & \dfrac{k}{M(a + x_1^e)^N} \\ 0 & \dfrac{aL_o x_3^e}{(a + x_1^e)^2 L_e} & -\dfrac{R_L}{L_e} \end{bmatrix} \begin{bmatrix} \delta x_1 \\ \delta x_2 \\ \delta x_3 \end{bmatrix} + \begin{bmatrix} 0 \\ 0 \\ \dfrac{V_{Lmax}}{L_e} \end{bmatrix} \delta u \tag{4.29}$$

$$\delta y = \begin{bmatrix} 1 & 0 & 0 \end{bmatrix} \begin{bmatrix} \delta x_1 \\ \delta x_2 \\ \delta x_3 \end{bmatrix}. \tag{4.30}$$

The linearized attractive state-space model is

$$\begin{bmatrix} \delta\dot{x}_1 \\ \delta\dot{x}_2 \\ \delta\dot{x}_3 \end{bmatrix} = \begin{bmatrix} 0 & 1 & 0 \\ \dfrac{kNx_3^e}{M(a + x_1^e)^{N+1}} & -\dfrac{c}{M} & -\dfrac{k}{M(a + x_1^e)^N} \\ 0 & \dfrac{aL_o x_3^e}{(a + x_1^e)^2 L_e} & -\dfrac{R_L}{L_e} \end{bmatrix} \begin{bmatrix} \delta x_1 \\ \delta x_2 \\ \delta x_3 \end{bmatrix} + \begin{bmatrix} 0 \\ 0 \\ \dfrac{V_{Lmax}}{L_e} \end{bmatrix} \delta u \tag{4.31}$$

$$\delta y = \begin{bmatrix} 1 & 0 & 0 \end{bmatrix} \begin{bmatrix} \delta x_1 \\ \delta x_2 \\ \delta x_3 \end{bmatrix}, \tag{4.32}$$

where the following definitions hold true for both systems,

$$x_i(t) = x_i^e + \delta x_i \quad i = 1, 2, 3 \tag{4.33}$$

$$y(t) = y^e + \delta y \tag{4.34}$$

$$u(t) = u_e + \delta u. \tag{4.35}$$

$$\tag{4.36}$$

4.3 Repulsive Suspension

In this section, the repulsive suspension configuration of the designed magnetic levitation system is further analyzed. In Section 4.3.1, the transfer function representation of the linearized state-space model is developed for the test-bed when it is operating in the repulsive mode. The pole locations are determined in terms of the system parameters and a discussion is held over their change in location due to a change in the equilibrium position, x_1^e. Section 4.3.2 discusses a open-loop system identification experiment that is used to identify the black-box model of the system found in Section 4.2. The identified black-box model is compared to the general transfer function model in Section 4.3.1. Finally, in Section 4.3.3 a controller design is discussed and implemented. The experimental results of the controller implementation are then presented to verify the black-box plant model and controller design.

4.3.1 Repulsive Transfer Function Analysis

In this section, a transfer function representation of the magnetic levitation system operating in the repulsive mode is developed from the linearized state-space model in terms of the system parameters. An approximation is made that allows a direct decomposition of the denominator of the transfer function to that of a characteristic polynomial with three left-hand plane poles. The general location of these poles are developed and movement of the mechanical pole locations with respect to a change in equilibrium position is discussed.

A transfer function representation from the small-signal input, δu, to the small-signal

signal displacement, δy, is developed from Equations 4.29 and 4.30 as

$$G_{p\ rep}(s) = \frac{\frac{k}{M(a+x_1^e)^N}\frac{V_{Lmax}}{L_e}}{s^3 + \left(\frac{R_L}{L_e} + \frac{c}{M}\right)s^2 + \left(\frac{R_L}{L_e}\frac{c}{M} + \frac{kNx_3^e}{M(a+x_1^e)^{N+1}}\left(1 - \frac{aL_o}{N(a+x_1^e)L_e}\right)\right)s + \left(\frac{R_L}{L_e}\frac{kNx_3^e}{M(a+x_1^e)^{N+1}}\right)}. \tag{4.37}$$

The characteristic polynomial of the system has the form,

$$D(s) = s^3 + a_2 s^2 + a_1 s + a_0 \tag{4.38}$$

where the subscripts of the coefficients refer to the power of the s-term in which they describe.

It is assumed that the characteristic polynomial can be factored into three roots, two of which, p_{m1} and p_{m2}, are determined by mechanical dynamics of the system, and a third, p_e, that is dependent on the electrical dynamics. Furthermore from experimental observations, since the system always achieves a stable equilibrium point regardless of the value of u and y, it is clear that all three poles are in the left-hand plane. Under this assumption and observation, the characteristic polynomial factors as

$$\begin{aligned} D(s) &= (s + p_e)(s + p_{m1})(s + p_{m2}) \\ &= s^3 + (p_e + (p_{m1} + p_{m2}))s^2 + (p_e(p_{m1} + p_{m2}) + p_{m1}p_{m2})s + p_e p_{m1} p_{m2}. \end{aligned} \tag{4.39}$$

Comparing the theoretical transfer function in Equation 4.37 to the expected characteristic polynomial in Equation 4.39 leads to an expression for the electrical and mechanical pole locations in terms of the values of the static equilibrium states and associated system parameters. The electrical term is determined from the s^2 and s^1 terms as,

$$p_e = \frac{R_L}{L_e}. \tag{4.40}$$

The summation term, $p_{m1} + p_{m2}$, is found from the s^2 term and the s^1 term after factoring out the electrical pole as

$$p_{m1} + p_{m2} = \frac{c}{M}. \tag{4.41}$$

The multiplicative term, $p_{m1}p_{m2}$, is found from the s^1 term as

$$p_{m1}p_{m2} = \frac{kNx_3^e}{M(a+x_1^e)^{N+1}}\left(1 - \frac{aL_o}{N(a+x_1^e)L_e}\right) \tag{4.42}$$

and from the s^0 term as

$$p_{m1}p_{m2} = \frac{kNx_3^e}{M(a+x_1^e)^{N+1}}. \tag{4.43}$$

The fact that Equations 4.42 and 4.43 do not yield identical expressions for the multiplicative term, $p_{m1}p_{m2}$, shows that the decomposition in Equation 4.39 is not exact. However, it is now shown that Equations 4.42 and 4.43 are approximately equal. Substitute Equation 4.28 into Equation 4.42 shows,

$$\frac{kNx_3^e}{M(a+x_1^e)^{N+1}}\left(1 - \frac{aL_o}{N(L_i(a+x_1^e)+aL_o)}\right) \tag{4.44}$$

As $N(L_i(a+x_1^e)+aL_o) \gg aL_o$,

$$1 - \frac{aL_o}{N(L_i(a+x_1^e)+aL_o)} \approx 1. \tag{4.45}$$

Therefore it is appropriate to approximate the multiplicative term, $p_{m1}p_{m2}$, as

$$p_{m1}p_{m2} = \frac{kNx_3^e}{M(a+x_1^e)^{N+1}}. \tag{4.46}$$

This approximation is consistent with that observed for the optical attractive levitation system discussed in Chapter 2.

Solving for the mechanical terms, p_{m1} and p_{m2}, using Equations 4.41 and 4.46 gives

$$p_{m1,2} = \frac{c}{2M} \pm \frac{1}{2}\sqrt{\left(\frac{c}{M}\right)^2 - \frac{4kNx_3^e}{M(a+x_1^e)^{N+1}}}. \tag{4.47}$$

Substituting Equation 4.26 into Equation 4.47 gives

$$p_{m1,2} = \frac{c}{2M} \pm \frac{1}{2}\sqrt{\left(\frac{c}{M}\right)^2 - \frac{4Ng}{(a+x_1^e)}}. \tag{4.48}$$

Using these results, the pole locations are approximated as

$$p_e = -\frac{R_L}{L_e} \tag{4.49}$$

$$p_{m1,2} = -\frac{c}{2M} \pm \frac{1}{2}\sqrt{\left(\frac{c}{M}\right)^2 - \frac{4Ng}{(a + x_1^e)}}. \tag{4.50}$$

When $(4Ng)/a > (c/M)^2$, it can be shown that the mechanical poles are complex when the equilibrium position, x_1^e, is between 0 and $(4NgM^2)/c^2 - a$. The mechanical poles will both be located at $p_{m1,2} = -c/(2M)$ when $x_1^e = (4NgM^2)/c^2 - a$. When $x_1^e > (4NgM^2)/c^2 - a$ the mechanical pole locations travel towards $-c/M$ and 0[rad/sec]. If $(4Ng)/a < (c/M)^2$ then the mechanical pole locations will be reflected at some position around $-c/(2M)$ for $x_1^e = 0$ and will travel towards $-c/M$ and 0[rad/sec] as x_1^e increases.

4.3.2 Open-Loop Identification Experiments

This section describes two open-loop system identification experiments used to determine the black-box model for the repulsive mode of the magnetic levitation system. These measurements are necessary for two reasons. First, the results of this system identification experiment will be used to verify the transfer function model obtained in Section 4.3.1. Second, the identified model determines the proper controller structure that is used in Section 4.3.3. No attempt is made to estimate the value of the parameters a, L_i, L_o, k, c, N, or M from the black-box model parameter values.

A series of two open-loop system identification experiments were performed. In the first experiment, a small square-wave excitation signal, δu, was directly superimposed on the actuator input, u_e. System identification techniques were used to identify the plant model which is defined between the small-signal actuator input δu and the small-signal estimate of the position of the permanent magnet, $\delta\bar{y}$. It was observed that the abrupt transitions of the excitation signal, δu, allowed frictional forces to bind the permanent magnet in place. The permanent magnet would tend not to move until the excitation signal transitioned again. System identification techniques were only able to identify first-order systems due to their algorithms trying to minimize the error over the full period. For example, using a square wave excitation signal produces a response that yields an identified model that is first order.

Figure 4.10 shows that the experimental and identified response do not agree. For this reason, a square wave input was not used.

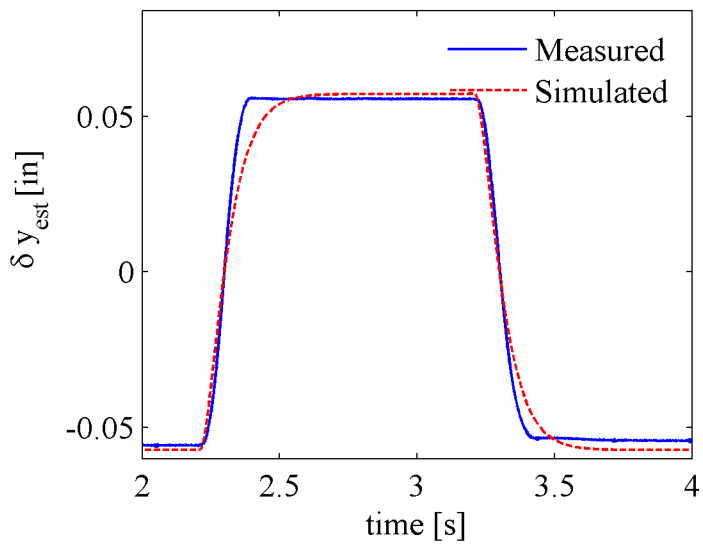

Figure 4.10. Simulated Response of a Mis-identified Plant Model Versus Actual Response Using a Square Wave Input

A second experiment was performed that first applied a square wave excitation signal to a first order system to increase the rise and fall times. It was thought that removing the abrupt transitions of a square-wave with a low-pass filter would keep the system response from binding as discussed earlier. An equilibrium actuator value $u_e = -0.3$ was used to initially set the estimated equilibrium position at $\bar{y}_e = 0.5$in. A 0.5Hz square-wave with an amplitude of $\delta u = \pm 0.04$ was used as the input to a low-pass filter with DC gain of 1 and cut-off frequency of 20[rad/sec]. This increased the 10% to 90% rise and fall times to approximately 0.11 seconds. The sampling frequency of the system was set at 15kHz and the PWM frequency was set at 5kHz. Figure 4.11 shows the filtered excitation signal used during the second system identification experiment.

MATLAB's pem function was used to best fit the model as

$$G_{Prep} = \frac{11.16s - 1155}{s^2 + 11.28s + 766.1}. \tag{4.51}$$

The electrical dynamics were likely fast in comparison to the mechanical dynamics, therefore only the two mechanical poles at $-5.64 \pm j27.0$ [rad/sec] were identified. An unexpected zero

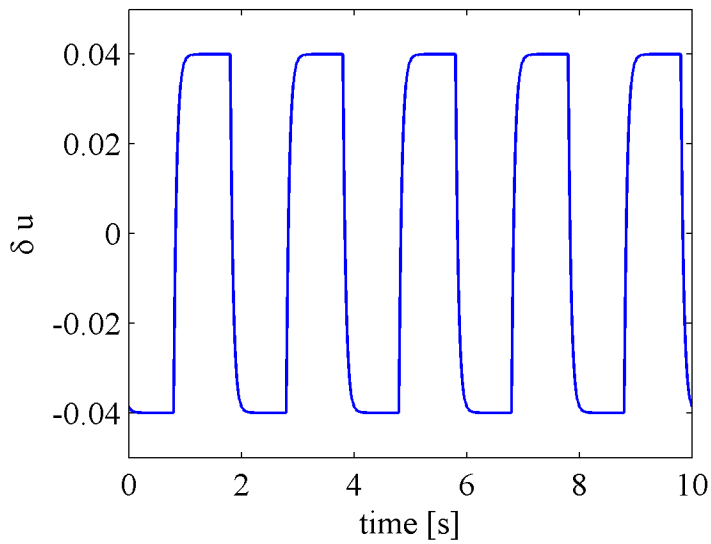

Figure 4.11. Filtered Square Wave Input Used During Open-Loop System Identification

was identified at +103.5[rad/sec]. Simulation of the identified plant using the same input was used to determine if the non-minimum phase zero was actually present and to verify the pole locations. Figure 4.12 shows that the simulated response is close to the actual response, up to when frictional forces cause the permanent magnet to bind. The mechanical poles found from system identification experiment 2 are complex in the left-hand plane, which do match the possible pole locations determined in Section 4.3.1.

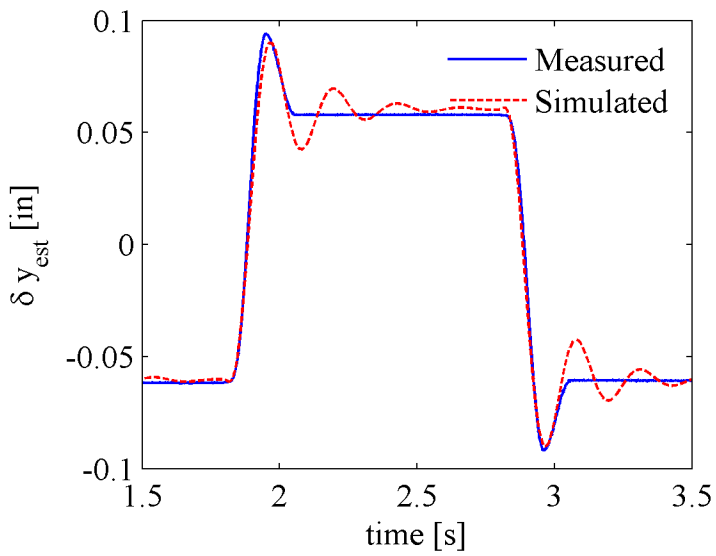

Figure 4.12. Simulated Response of the Identified Plant Model Versus Actual Response Using a Filtered Square Wave Input

4.3.3 Controller Design and Experimental Verification

Given the identified small-signal model from Section 4.3.2, a digital controller is now synthesized for a third experiment. Comparing the predicted and measured response of the closed-loop system will confirm the identified system model. The non-minimum phase zero in the identified plant model causes a complementary response to a typical root-locus design. Therefore, a continuous phase-lead controller is designed instead of a phase-lag.

The continuous controller is designed as

$$G_{Crep}(s) = 0.2\frac{s+50}{s+100}. \tag{4.52}$$

The controller's zero-order hold discrete-time equivalent model at a sampling frequency of 15kHz is

$$G_{Crep}(z) = 0.2\frac{z-0.9965}{z-0.9934} \quad T_S = 66.6\mu s. \tag{4.53}$$

Experiment 3 uses the same system settings as experiment 2. The feedback loop is closed using the designed controller in Equation 4.52 and superimposes the excitation signal on the reference position signal, $y_{ref} = 0.5in$. The excitation signal was set as a 0.5Hz square wave with amplitude of $\delta y_{ref} = \pm 0.2in$. Figure 4.13 shows the simulated versus the actual response of the system. A comparison of the two signals suggests that the poles of the plant model given in Equation 4.51 are approximately correct.

It should be pointed out that there is a discrepancy in the system response that shows up when the reference signal is transitioning from one steady-state value to another. If there is only one non-minimum phase zero present in the closed-loop system, then the response to a rise or fall transition will first show movement in the opposite direction of what is being commanded before turning around and following the correct trajectory [30]. If there are two non-minimum phase zeros present in the closed-loop system, then the response to a rise or fall transition will immediately follow the commanded direction, turn away, then return to the initial trajectory [30]. The simulated closed-loop response shows the system settling towards steady state then acting as it is expected for one non-minimum phase zero. The measured closed-loop system response is already at steady state, then responding as if two

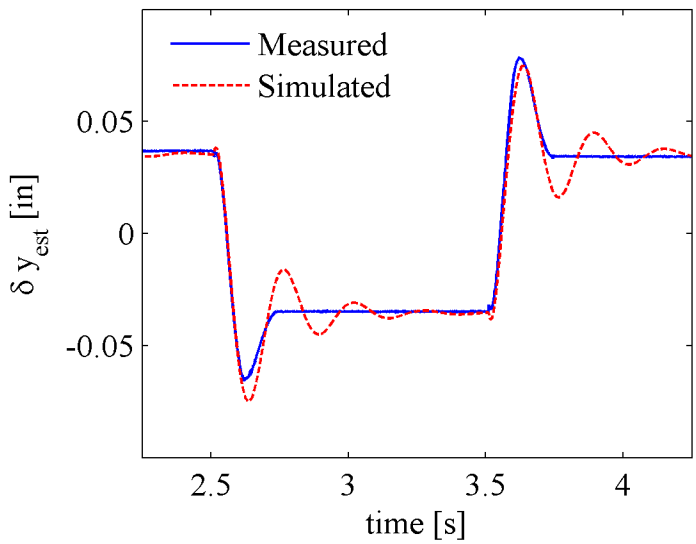

Figure 4.13. Simulated Response of the Expected Closed-Loop System Versus Actual Response Using a Filtered Square Wave Input

non-minimum phase zeros are present. Figures 4.14 and 4.15 show this response in detail. It is clear that there are missing and incorrect dynamics in the open-loop model. The fact that the simulation is not in steady state when the measured is in steady state can be attributed to the frictional forces but may also indicate that the damping of the open-loop system dynamics are incorrect. The mechanism for the identified and suggested non-minimum phase zeros is unknown at this time. They may be an effect caused by the frictional forces, some unmodeled electromechanical dynamic, or possibly an artifact from the position sensing subsystem.

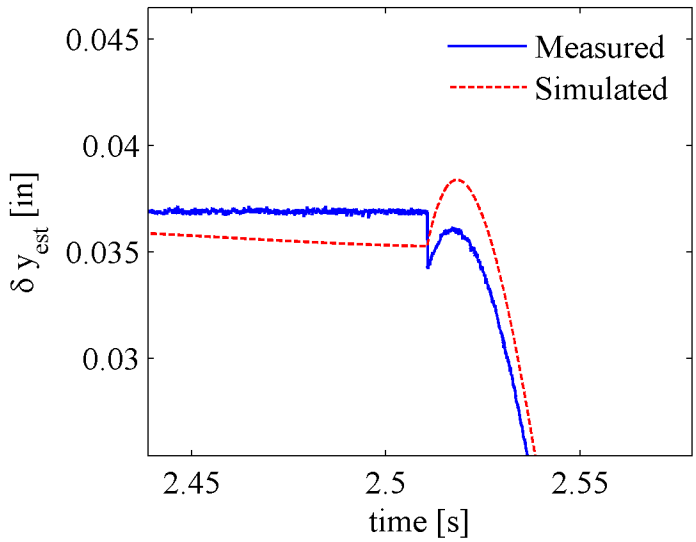

Figure 4.14. Close-Up View of the Fall Transition of the Closed-Loop Response of the Repulsive System

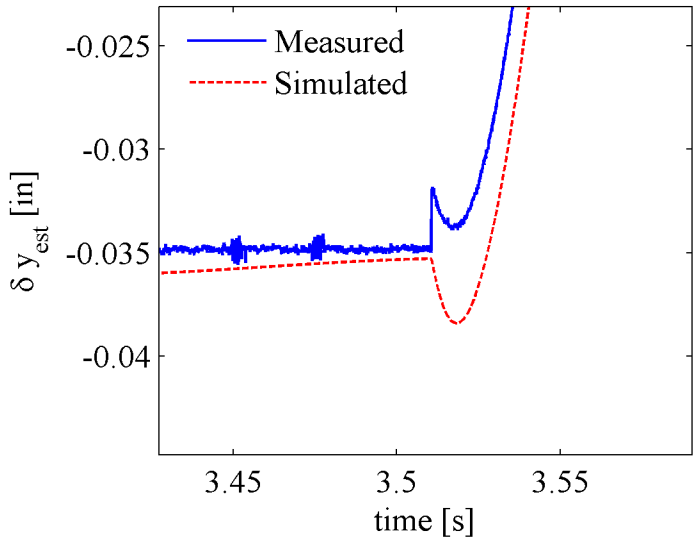

Figure 4.15. Close-Up View of the Rise Transition of the Closed-Loop Response of the Repulsive System

4.4 Attractive Suspension

In this section, the attractive suspension configuration of the designed magnetic levitation system is further analyzed. In Section 4.4.1, the transfer function representation of the linearized state-space model is developed for the test-bed when it is operating in the attractive mode. The pole locations are identified in terms of the system parameters and a discussion is held over their change in location due to a change in the equilibrium position, x_1^e. Section 4.4.2 discusses a closed-loop system identification experiment that is used to identify a black-box model of the system in Section 4.4. The identified black-box model is compared to the general transfer function model in Section 4.4.1. Finally, in Section 4.4.3 a controller design is discussed and implemented. The experimental results of the controller implementation are then presented to verify the black-box plant model and controller design.

4.4.1 Attractive Transfer Function Analysis

In this section, a transfer function representation of the magnetic levitation system operating in the attractive mode is developed from the linearized state-space model in terms of the system parameters. An approximation is made that allows a direct decomposition of the denominator of the transfer function to that of a characteristic polynomial with two left-hand plane poles and one right-hand plane pole. The general location of these poles are developed and movement of the mechanical pole locations with respect to a change in equilibrium position is discussed.

A transfer function representation from the small-signal input, δu, to the small-signal signal displacement, δy, is developed from Equations 4.31 and 4.32 as

$$G_{p\ att}(s) = \frac{-\frac{k}{M(a+x_1^e)^N}\frac{V_{Lmax}}{L_e}}{s^3 + \left(\frac{R_L}{L_e} + \frac{c}{M}\right)s^2 + \left(\frac{R_L}{L_e}\frac{c}{M} - \frac{kNx_3^e}{M(a+x_1^e)^{N+1}}\left(1 - \frac{aL_o}{N(a+x_1^e)L_e}\right)\right)s - \left(\frac{R_L}{L_e}\frac{kNx_3^e}{M(a+x_1^e)^{N+1}}\right)}. \tag{4.54}$$

As in Section 4.3.1, the characteristic polynomial of the system has the form

$$D(s) = s^3 + a_2 s^2 + a_1 s + a_0, \tag{4.55}$$

where the subscripts of the coefficients refer to the power of the s-term in which they describe.

It is assumed that the characteristic polynomial can be factored into three roots, two of which, p_{m1} and p_{m2}, are determined by mechanical dynamics of the system, one in the left-hand plane, p_{m1}, and the other in the right-hand plane, p_{m2}, and a third, p_e, that is dependent on the electrical dynamics. Under this assumption, the characteristic polynomial factors as

$$\begin{aligned} D(s) &= (s+p_e)(s+p_{m1})(s-p_{m2}) \\ &= s^3 + (p_e + (p_{m1} - p_{m2}))s^2 + (p_e(p_{m1} - p_{m2}) - p_{m1}p_{m2})s - p_e p_{m1} p_{m2}. \end{aligned} \tag{4.56}$$

Comparing the theoretical transfer function in Equation 4.54 to the expected characteristic polynomial in Equation 4.56 leads to an expression for the electrical and mechanical pole locations in terms of the values of the static equilibrium states and associated system parameters. The electrical term is determined from the s^2 and s^1 terms as,

$$p_e = \frac{R_L}{L_e}. \tag{4.57}$$

The subtractive term, $p_{m1} - p_{m2}$, is found from the s^2 term and the s^1 term after factoring out the electrical pole as

$$p_{m1} - p_{m2} = \frac{c}{M}. \tag{4.58}$$

The multiplicative term, $p_{m1}p_{m2}$, is found from the s^1 term as

$$p_{m1}p_{m2} = -\frac{kNx_3^e}{M(a+x_1^e)^{N+1}}\left(1 - \frac{aL_o}{N(a+x_1^e)L_e}\right) \tag{4.59}$$

and from the s^0 term as

$$p_{m1}p_{m2} = -\frac{kNx_3^e}{M(a+x_1^e)^{N+1}}. \tag{4.60}$$

Equation 4.60 indicates that the initial assumption of the mechanical pole locations are correct as only real valued poles, one in the left-hand plane and the other in the right-hand plane, would be able to make this term negative. Multiplication of complex conjugate poles

either in the left-hand or right-hand plane, two real left-hand plane, or two real right-hand plane mechanical poles would lead to a positive multiplicative term.

The fact that Equations 4.42 and 4.43 do not yield identical expressions for the multiplicative term, $p_{m1}p_{m2}$, shows that the decomposition in Equation 4.39 is not exact. However, it is now shown that Equations 4.59 and 4.60 are approximately equal. Substitute Equation 4.28 into Equation 4.59 shows,

$$-\frac{kNx_3^e}{M(a+x_1^e)^{N+1}}\left(1-\frac{aL_o}{N(L_i(a+x_1^e)+aL_o)}\right) \tag{4.61}$$

As $N(L_i(a+x_1^e)+aL_o) \gg aL_o$,

$$1-\frac{aL_o}{N(L_i(a+x_1^e)+aL_o)} \approx 1. \tag{4.62}$$

Therefore it is appropriate to approximate the multiplicative term, $p_{m1}p_{m2}$, as

$$p_{m1}p_{m2} = -\frac{kNx_3^e}{M(a+x_1^e)^{N+1}}. \tag{4.63}$$

Solving for the mechanical terms, p_{m1} and p_{m2}, using Equations 4.58 and 4.63 gives

$$p_{m1} = \frac{c}{2M} \pm \frac{1}{2}\sqrt{\left(\frac{c}{M}\right)^2 - \frac{4kNx_3^e}{M(a+x_1^e)^{N+1}}}. \tag{4.64}$$

Substituting Equation 4.26 into Equation 4.64 gives

$$p_{m1} = \frac{c}{2M} \pm \frac{1}{2}\sqrt{\left(\frac{c}{M}\right)^2 - \frac{4Ng}{(a+x_1^e)}}. \tag{4.65}$$

Therefore, p_{m2} is defined as

$$p_{m2} = -\frac{c}{2M} \pm \frac{1}{2}\sqrt{\left(\frac{c}{M}\right)^2 - \frac{4Ng}{(a+x_1^e)}}. \tag{4.66}$$

Using these results, the pole locations are approximated as

$$p_e = -\frac{R_L}{L_e} \tag{4.67}$$

$$p_{m1} = -\frac{c}{2M} \pm \frac{1}{2}\sqrt{\left(\frac{c}{M}\right)^2 - \frac{4Ng}{(a + x_1^e)}}. \tag{4.68}$$

$$p_{m2} = \frac{c}{2M} \pm \frac{1}{2}\sqrt{\left(\frac{c}{M}\right)^2 - \frac{4Ng}{(a + x_1^e)}}. \tag{4.69}$$

When $(4Ng)/a > (c/M)^2$, it can be shown that the mechanical poles are both complex when the equilibrium position, x_1^e, is between 0 and $(4NgM^2)/c^2 - a$. As the mechanical poles lie in separate planes, this suggests that the approximation breaks down for this case and the exact decomposition should be used at small values of x_1^e. When $x_1^e = (4NgM^2)/c^2 - a$, the mechanical poles are reflected about the imaginary axis at $\pm c/(2M)$[rad/sec]. As Equation 4.58 bounds the location of the mechanical poles with respect to each other, such that there must always be a distance of c/M between the two poles. To satisfy this condition, the square root terms, shown in Equations 4.68 and 4.69, are either both added or both subtracted. This shows that the mechanical poles either shift in step towards the left-hand plane or towards the right-hand plane with an increase in the equilibrium position, x_1^e. It is uncertain which case is correct.

4.4.2 Closed-Loop Identification Experiments

This section describes a closed-loop system identification experiment used to determine the black-box model for the attractive mode of the magnetic levitation system. These measurements are necessary for two reasons. First, the results of this system identification experiment will be used to verify the transfer function model obtained in Section 4.4.1. Second, the identified model determines the compensator design that is used in Section 4.4.3.

The system identification experiment was performed in two parts. First, a controller was hand-tuned, such that the system stabilized at an equilibrium position, $y_e = 0.6$in with $u_e = 0.6$. Both the sampling frequency of the system and the frequency of the PWM were

set at 5kHz. The hand-tuned continuous controller is a phase-lead compensator designed as

$$G_{Catt}(s) = -8\frac{s+50}{s+100}. \tag{4.70}$$

The controller's zero-order hold discrete-time equivalent model at a sampling frequency of 5kHz is

$$G_{Catt}(z) = -8\frac{z-0.9901}{z-0.9802} \quad T_S = 200\mu s. \tag{4.71}$$

It should be noted that this compensator has a negative gain term, therefore traditional root locus design techniques are traded for their complementary counterparts. This suggests that the plant model for the attractive mode also has a non-minimum phase zero.

Second, a excitation signal was applied and the system response was recorded. It was immediately decided to pre-filter the excitation signal based on the results of the system identification experiments in Section 4.3.2. A small square-wave excitation signal, δy_{ref}, was first pre-filtered and superimposed on the equilibrium reference position, y_{ref}. a 0.25Hz square-wave with an amplitude of $\delta y_{ref} = \pm 0.002$ was used as the input to a low-pass filter with DC gain of 1 and cut-off frequency set to 303[rad/sec]. This increased the 10% to 90% rise and fall times to approximately 7.3ms. Figure 4.16 shows the filtered excitation signal used during the system identification experiment.

MATLAB's pem function was used to best fit the closed-loop model, defined between its small-signal input δy_{ref} and its small-signal output δy_{est}, as

$$G_{CLatt} = \frac{-32.75(s-175.5)}{(s^2+10.4s+4571)}. \tag{4.72}$$

While the electrical dynamics are likely fast in comparison to the mechanical dynamics, it was expected that the addition of the dynamics from the controller would have been seen in the closed-loop system. Simulation of the identified closed-loop system using the same input was used to verify the closed-loop model given in Equation 4.72. Figure 4.17 shows that the simulated response is close to the actual response, up to when frictional forces cause the permanent magnet to bind.

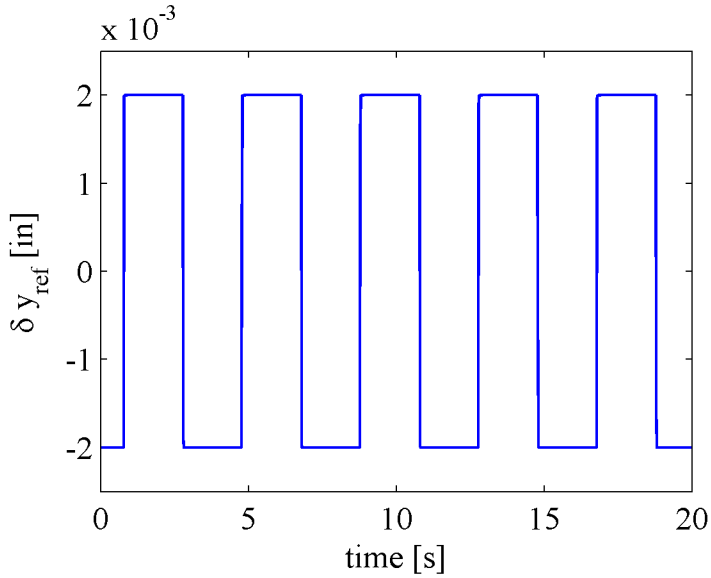

Figure 4.16. Filtered Square Wave Input Used During Closed-Loop System Identification

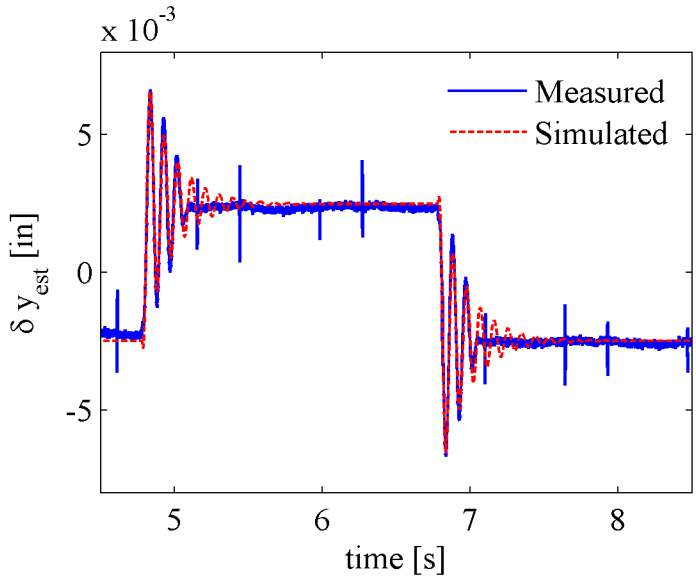

Figure 4.17. Closed-Loop Response of the Attractive System Using a Hand-Tuned Controller

The closed-loop model is written in terms of its subsystems as

$$G_{CL(att)} = \frac{G_{P(att)}G_{C(att)}}{1 + G_{P(att)}G_{C(att)}}. \tag{4.73}$$

The plant model, G_{Patt}, is identified by manipulating Equation 4.73 as

$$G_{P(att)} = \frac{1}{G_{c(att)}} \frac{G_{CL(att)}}{1 - G_{CL(att)}}. \tag{4.74}$$

Equation 4.74 is evaluated as,

$$G_{P(att)} = \frac{4.09(s - 173.5)(s + 100)}{(s + 61.32)(s + 50)(s - 18.11)}. \tag{4.75}$$

While this plant model contains three poles, it is unlikely that the value of the electrical pole happened to be close in value to the controller zero. Because the controller dynamics were not represented in the closed-loop model, they did not cancel when evaluating Equation 4.73. The poles located at -61.32 and +18.11 are likely the mechanical pole locations, and are consistent with the analysis in Section 4.4.1. This model also contains a non-minimum phase zero located at +173.5[rad/sec]. This result confirms that there are unmodeled dynamics in the system as both the repulsive and attractive small-system black-box models contain non-minimum phase zeros.

4.4.3 Controller Design and Experimental Verification

Given the identified small-signal model from Section 4.4.2, a digital controller is now synthesized for a second experiment. Comparing the predicted and measured response of the closed-loop system will confirm the identified system model. While the non-minimum phase zero in the identified plant model causes a complementary response to a typical root-locus design, the hand-tuned phase-lead controller that was implemented in Section 4.4.2 proved to be reliable enough to perform system identification experiments. A continuous phase lead-lag controller is designed to stabilize the system and to reduce steady state error. The phase-lead component was based on the hand-tuned controller while the phase-lag was placed close to the origin to minimize effects on the root locus.

The continuous controller is designed as

$$G_{Catt}(s) = -16 \frac{s + 20}{s + 100} \frac{s + 0.5}{s + 0.001}. \tag{4.76}$$

The controller's zero-order hold discrete-time equivalent model at a sampling frequency of 5kHz is

$$G_{Catt}(z) = \frac{-16z^2 + 31.94z - 15.94}{z^2 - 1.98z + 0.9802} \quad T_S = 200\mu s. \tag{4.77}$$

Experiment 2 uses the same system settings as in experiment 1. The feedback loop is closed using the designed controller in Equation 4.76 and superimposes the excitation signal on the reference position signal, $y_{ref} = 0.6in$ with $u_e = 0.6$. The excitation signal was set as a 1Hz ramp wave with amplitude of $\delta y_{ref} = \pm 0.001in$. Figure 4.18 shows the simulated and actual response of the system versus the ramp reference signal.

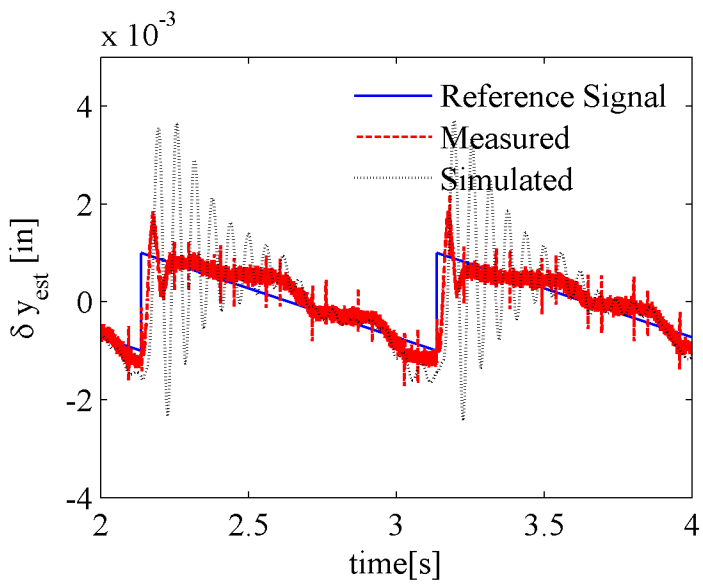

Figure 4.18. Closed-Loop Response of the Attractive System Following a Saw Tooth Signal

A comparison of the two signals suggests that the frequency of the poles of the plant model given in Equation 4.51 are approximately correct, but the their damping ratio is incorrect. It is seen that the measured data follows the ramp quite well, while the simulation is seen to oscillate. The plant model was identified using an excitation signal that had an amplitude that is twice as large as the one used to create the ramp. The effects of friction were less apparent when the plant was identified. The system did not oscillate as expected because the frictional forces affect the system more when the reference signal's amplitude is decreased. Even so, this model is a good basis in which to design a controller for further system identification experiments.

Chapter 5

Discussion and Recommendations

This chapter discusses the analysis of the magnetic levitation system that was preformed in Chapter 4 and provides several recommendations for future work. Section 5.1 discusses discrepancies between the theoretical and black-box models and discusses issues with identifications techniques. This section also includes a discussion on controller design constraints for non-minimum phase zeros and how these constraints affect the system response. Section 5.2 compares the system to the design objectives and presents recommendations for future work.

5.1 Discussion and Limitations

This section discusses three topics pertaining to the analysis of the magnetic levitation system performed in Chapter 4. First, the presence of non-minimum phase zeros in the experimental models are discussed in light that they were not predicted by the theoretical model. Probable sources of the non-minimum phase zeros are addressed. Second, mis-identification of the plant dynamics are attributed primarily to the non-viscous friction present in the system. An alteration to the identification process is proposed to decrease the error in the identified model. Third, the limitations and constraints of control design for non-minimum phase systems and the trade-offs between the closed-loop transient response are discussed.

First, the theoretical models identified in Chapter 4 do not fully explain the dynamics found through system identification in Sections 4.3.2 and 4.4.2. While the mechanical poles

were thought to have been identified properly, the theoretical model does not include the potential for the system to have zeros. Empirical evidence suggest that even the black-box model is incorrect due to the transient response associated with the presence of two non-minimum phase zeros. These dissimilarities likely arises from one or more the following four assumptions being incorrect.

The first assumption is that the equation for the force of electric origin, $f^e(y, i_L)$, is the same as for the ECP Model 730 MagLev Apparatus which uses a disk magnet and a pancake coil. The second assumption is that the equation defining the inductance of the electromagnet due to the position of a permanent magnet, $L(y)$, is the same as for a ferromagnetic mass. The third assumption is that the force between the permanent magnet and the core of the electromagnet, f_{mc}, is negligible. The fourth assumption is that the unmodeled non-viscous frictional forces can be neglected.

Second, it is not clear if the system identification techniques properly identified the dynamics of the system. The system identification techniques used in this thesis use a cost function that minimizes the error over the entire waveform. This leads to mis-identification of the pole characteristics due to the unmodeled frictional forces prematurely damping the response of the system. An identification can be made with more accuracy if a weighting scheme is added to the cost function. A heavy emphasis on the initial overshoot and the transient response seen directly during the rise and fall times would be ideal.

Third, the presence of non-minimum phase zeros in the plant model restricts the type of control that can be used. Depending on the model, it may be found that complementary root locus techniques may be needed. Despite the challenges associated with controller topology, the primary issue associated with systems that have non-minimum phase zeros is that there will be trade-offs to the transient response. A fast rise-time may also accrue a large overshoot. A fast rise-time and a small overshoot may cause a large undershoot with a long settling time [31, 32, 33]. Thus, it should be understood prior to the design what criteria is pertinent to the control of that particular non-minimum phase system.

5.2 Design Objectives and Recommendations

The first design objective of this thesis was to design a magnetic levitation system that provides the three advantages offered by Marsden's design, without the three disadvantages observed by the honors students. This magnetic levitation system uses a permanent magnet to reduce the current required to achieve a given levitation position. A PWM subsystem is used to drive the current of the electromagnet to significantly reduce the power dissipated in the semiconductor device. This system also uses a Hall effect sensor to measure the position of the levitation mass over a greater range than the optical system in Chapter 2. The PWM chip that was not functioning correctly was removed and replaced with a more stable system from within the dSPACE DAQ. The dynamic oscillations that were observed in Marsden's system are not present in this system when controlled with a properly designed compensator. It can be readily observed that first design goal has been achieved.

The second design objective of this thesis is to be able to levitate the permanent magnetic in both the attractive and repulsive configurations. While this has objective has been accomplished, as shown in Chapter 4, accurate and consistent modeling of the system has yet to be achieved. The recommendations that will be given, will remedy the issues with modeling and identification of this magnetic levitation system.

The overall objective of this thesis is to develop a low-cost test-bed for control system courses that can be used to demonstrate concepts of linear control systems applied to stable and unstable equilibrium points of a non-linear system. Based on the difficulty of analysis and controller design, this system is currently best used as a test-bed for graduate studies of control systems. Several recommendations are made that will reduce the complexity of the control design to a level that is reasonable for undergraduate studies.

First, an investigation should be undertaken to properly identify the force of electric origin, $f^e(y, i_L)$, coupling the electromagnet and permanent magnet. Second, an investigation should be undertaken to properly identify the relationship between the position of the permanent magnet and the inductance of the electromagnet. Third, an investigation should be undertaken to understand the effects of the interaction between the permanent magnet and the core of the electromagnet. Fourth, the origin of the non-minimum phase zeros should be identified. Fifth, the circuit board should be updated and the guide rail should be machined to reduce non-viscous friction encountered in experimentation. These recommendations will

enable the students to properly identify the model structure and to design an appropriate controller.

Appendix: Sample MATLAB Code

Determining Inductance Parameters of the LNS System

```
%%%!!!!!!!!!!!!!!!!!!!!!!!!!!!!!!!!!!!!!!!!!!!!!!!!!!!!!!!!!!!!!!!!!!!!!!!!
%%% Find the Inductance parameters of the LNS Optical Levitation System
%%% L(y) = Li + Lo/(1 + y/a)
%%%!!!!!!!!!!!!!!!!!!!!!!!!!!!!!!!!!!!!!!!!!!!!!!!!!!!!!!!!!!!!!!!!!!!!!!!!

%% An experiment was performed to find the internal resistance of the function
%% generator used in the rise time experiments. This was necessary in order
%% properly determine the series resistance of the circuit. 2 resistors
%% were attached, one at a time, to the output. The voltage across each
%% resistor was measured. The theoretical internal series resistance was
%% solved for.

    % Measured resistance of the actual resistors used in the experiment.
    R1 = 50.93;
    R2 = 238.9;

    % Measured Voltage across the series resistors.
    Vout1 = 3.031;
    Vout2 = 5.031;

    % Solving for the internal series resistance.
```

```
    Rs1 = R1*R2*(Vout2-Vout1)/(R2*Vout1-R1*Vout2);

%% Inductance Experimental Measurements

    % Measured distance between the mass and the coil for each experiment.
    y_in = [0,.096,.16,.224,.288,inf]; % in inches
    y_m = y_in*0.0254;% in meters

    % Measured rise time of each experiment
    rise_time = [2.87,1.67,1.63,1.62,1.58,1.58]*10^-3;

    % Measured load resistor and DC resistance of the coil
    RLoad = 50.93;
    RL = 32.58;

    % Total DC resistance of the experiment
    Rtotal = RL+RLoad+Rs1;

%% Inductance Calculations

    % Calculated Inductance of each experiment
    L = (Rtotal/2.2)*rise_time;

    % Li is the inductance of the system without the mass: i.e. y = inf
    Li = L(end)

    % Lo+Li is the inductance of the system when the mass is at y = 0
    Lo = L(1)-Li

    % Subtract out Li from the inductance values should leave L_bar =
    % Lo/(1+y/a)
    L_bar = L - Li;

    % L_bar_inv = Lo./L_bar = 1 + (1/a)y
    L_bar_inv = Lo./L_bar;

    % Use the polyfit command to fit a 1st order equation to the data. The
    % last 2 data points are not included as L_bar_inv = inf at those
    % points and would cause problems with the proper evaluation of the
    % polyfit function.
```

```
    P1 = polyfit(y_m(1:4),L_bar_inv(1:4),1)

    % Evaluate the polynomial coeficients for accuracy, by evaluating the
    % function in terms of the position variables.
    data1 = polyval(P1,y_m(1:4));

    % Plot the data to verify accuracy of the polynomials.
    figure(1)
    plot(y_m(1:4),L_bar_inv(1:4),'ob',y_m(1:4),data1,'xr')

    % Determine the value of the parameter 'a'
    a = 1/P1(1);

%% Perform verification of the parameters Lo, Li, and a

    % Create a vector of mass positions in meters
    Y = [0:1/10000:y_m(5)];

    % Evaluate the Inductance equation for the found parameters values
    L_test = Li+Lo./(1+Y./a);

    save coilparameters Lo Li a
```

Symbolic Solution for the LNS Plant Model

```
%%%!!!!!!!!!!!!!!!!!!!!!!!!!!!!!!!!!!!!!!!!!!!!!!!!!!!!!!!!!!!!!!!!!!!
%%% Evaluate the theoretical model based upon measured parameters
%%%!!!!!!!!!!!!!!!!!!!!!!!!!!!!!!!!!!!!!!!!!!!!!!!!!!!!!!!!!!!!!!!!!!!

Li = 97.328*10^-3;
Lo = 79.464*10^-3;
a = 177.4*10^-6;
g = 9.8;% m/s^2
M = 3.246*10^-3;%kg
Again = 361;
RL = 32.58;

syms x1e s
```

```
Le = (Li*(a+x1e) + a*Lo)/(a + x1e);

% The linearized state space model for the plant
A = [0 1 0;...
    2*g/(a+x1e) 0 -sqrt(2*g/M)*sqrt(a*Lo)/(a + x1e);...
    0 sqrt(2*a*Lo*M*g)/((a+x1e)*Le) -RL/Le];
B = [0; 0; Again/Le];
C = [1 0 0];

% Create a transfer function representation of the state space model
Gp = C*inv(s*eye(3)-A)*B;

% Create a function representing the equilibrium current due to
% equilibrium position.
ue = sqrt(2*M*g/(a*Lo))*(a+x1e);

% Define a range of possible equilibrium positions from 0-1/2
% inches from the coil
x1 = [1/1000:1/1000:0.5*.0254]; % in meters

% Evaluate the transfer function, pole locations, and equilibrium
% current for each of the defined equilibrium positions
for i = 1:length(x1)
    Gp_eval = subs(Gp,'x1e',x1(i));
    Gp_eval = simplify(Gp_eval);
    [num,den] = numden(Gp_eval);

    den = sym2poly(den);
    num = double(num)/den(1);
    den = den/den(1);

    G(i) = tf(num,den);
    P(:,i) = sort(roots(den));
    Le_eval = double(subs(Le,'x1e',x1(i)));
    Pest(:,i) = sort([-RL/Le_eval; -sqrt(2*g/(a+x1(i)));sqrt(2*g/(a+x1(i)))]);
    ue_(i) = double(subs(ue,'x1e',x1(i)));
end
```

Automated Data Collection Code

```
%%%!!!!!!!!!!!!!!!!!!!!!!!!!!!!!!!!!!!!!!!!!!!!!!!!!!!!!!!!!!!!!!!!!!!!!!
%%% Mass data collection utility for closed loop system identification of the
%%% LNS mag lev system. The user is asked for pertinent experimental
%%% parameters. Pressing enter without entering a value results in the
%%% default parameter being used.
%%%!!!!!!!!!!!!!!!!!!!!!!!!!!!!!!!!!!!!!!!!!!!!!!!!!!!!!!!!!!!!!!!!!!!!!!

% Get necessary data from the user
Runs = input('Input␣the␣number␣of␣Runs:␣');
display('␣');
Time = input('Input␣the␣time␣of␣each␣Run:␣');
display('␣');
SigFreq = input('Input␣the␣Frequency␣of␣the␣Perturbation␣Signal:␣');
display('␣');
Amplitude = input('Input␣the␣Amplitude␣of␣the␣Perturbation␣Signal:␣');
display('␣');
Filename = input(['Input␣the␣name␣of␣the␣MAT␣file␣that␣this␣data',...
                                                'will␣be␣saved␣under:␣']);
display('␣');

% Declare Defaults if not set by the user
if isempty(Time),Time = 10;end
if isempty(Runs),Runs = 10;end
if isempty(SigFreq),SigFreq = 0.5;end
if isempty(Amplitude),Amplitude = 0.001;end
if isempty(Filename),Filename = 'ContRun1';end

% Sampling period of the DAQ. This is also set in the simulink model file.
% Changes in one should reflect changes in the other
Ts = 0.0001;

% Delay between data runs
Delay = 0.1;



% Build the simulink model file
rtwbuild('IDContinuous')
```

```
% Tell Matlab that pauses will be used
pause on

% Select processor board 'ds1104'
mlib('SelectBoard','ds1104');

% Select variables to be traced and obtain their descriptors
var_names = {'simState';...
             'Model_Root/rref';...
             'Model_Root/ysensor';...
             'currentTime'};

% Get the addresses of the trace variables
var = mlib('GetTrcVar',var_names);

% Get the address of the excitation signals' frequency variable
Freq_path = mlib('GetTrcVar',{'Model_Root/Signal\nGenerator/Frequency'});

% Get the address of the excitation signals' amplitude variable
Amp_path = mlib('GetTrcVar',{'Model_Root/Signal\nGenerator/Amplitude'});

% Stop the processor by setting simState to 0
mlib('Write',var(1),'Data',0);

% Set up the excitation signal
mlib('Write', Freq_path, 'Data',{SigFreq});
mlib('Write', Amp_path, 'Data',{Amplitude});

% Set up the DAQ parameters
mlib('Set','TraceVars', var,...
           'StepSize',Ts,...
           'Start',Delay,...
           'Stop',Time+Delay);

% Start the processor by setting simState to 2
mlib('Write', var(1),'Data',2);

% Make sure that a capture is not taking place
mlib('StopCapture')
```

```
% Prompt the user to set the mass
Dummy = input('Place the Ball');
display(' ');

% Loop until all of the data runs have been succesfully completed
for i = 1:Runs
   n = 1; % Control Variable for the while loop

   % Loop until the data run is succesful
   while n == 1

        % Start capture on DS1104
        mlib('StartCapture');
        while mlib('CaptureState')~=0, end

        % Collect the Experimental Data from the DAQ
        out_data = mlib('FetchData');

        % Save the Data from the run in a structure
        Ref{i} = out_data(2,:)';
        Sensor{i} = detrend(out_data(3,:)','constant');

        % Plot the captured data to verify that it was succesffully captured
        % without disturbances that could distort the analysis
        figure(1)
        plot(Sensor{i})
        title(['Range of data = ',num2str(range(Sensor{i}))])

        % Prompt the user if they weant to keep the data.
        Keep = input('Keep this data: yes = 1, no = 0: ');

        % Pressing enter without entering data causes the data to be saved
        if isempty(Keep); Keep = 1; end

        if Keep == 1
            n = 0;% break the while loop to increment to the next run
            % Update User as to the completion of the experiment
            display(['Run # ', num2str(i),' Completed']);
            display(' ');
        end
```

```
    end
end

% Stop the processor by setting simState to 0
mlib('Write', var(1),'Data',0);

% Prompt the user to unplug the system
display('Unplug␣the␣Optical␣Electromagnetic␣Levitator');
display('␣');

%% Save all of the data in a .mat file
save(Filename,'Ref','Sensor','Ts')
```

Run Averaging Code

```
%%%!!!!!!!!!!!!!!!!!!!!!!!!!!!!!!!!!!!!!!!!!!!!!!!!!!!!!!!!!!!!!!!!!!!!!!!
%%% Load the experimental data and average the runs together to remove
%%% noise from the experimental data.
%%%!!!!!!!!!!!!!!!!!!!!!!!!!!!!!!!!!!!!!!!!!!!!!!!!!!!!!!!!!!!!!!!!!!!!!!!

% Get necessary data from the .mat file
Filename = 'ContRun2d';
load(Filename)

% Find the number of runs from the saved data file
L = length(Ref);

% Find the initial Index of each Input/Output set so that they will all line
% up. Line them up by the start of the first rise time of the reference
% signal.
for i = 1:L
    % Set norm = ref so we can manipulate without disturbing original data
        Norm_In = Ref{i};
    % Set Index = 0 for start of operation.
        Index1 = 0;
    % Is the input already high?
        if (Norm_In(1) > 0)
            % If so...find the first index where it is low.
            Index1 = find(Norm_In < 0,1,'first');
```

```
            % Truncate all of the data point where it was initially high.
            Norm_In = Norm_In(Index1:end);
        end
    % Find the first index where it is high.
        Index2 = find(Norm_In > 0,1,'first');
    % This gives the true index we use with the ref data
        Index = Index1 + Index2;
    % Resave the Ref data starting at Index
        Ref{i} = Ref{i}(Index:end);
    % Resave the Output data starting at Index
        Sensor{i} = Sensor{i}(Index:end);
    % Save the length of the vector of the data for later reference
        L2(i) = length(Ref{i});
end

minL = min(L2);

% Review Data for obvious disturbances
keep = zeros(1,L);
for i = 1:L
    plot(Sensor{i}(1:minL))
    title(['Runs = ',num2str(i)])
    k = input(['Keep Data? Press Enter to Keep,'...
               'enter a value and Enter to remove :'])
    if isempty(k); keep(i) = 1; end
end

% Find the min length data vector from all of the runs and truncate all data
% sets to this value and save the data in a matrix of row vectors so that
% we can run average easily.
Index = find(keep == 1);
numRuns = sum(keep);

for i = 1:numRuns
    Sensor_Matrix(Index(i),1:minL) = Sensor{Index(i)}(1:minL);
    Ref_Matrix(Index(i),1:minL) = Ref{Index(i)}(1:minL);
end

% Average all Output Data sets. Input sets should be exactly the same but
% are averaged just the same. The mean function will average each column of
```

```
% data leaving 1 row vector.
Avg_Sensor = mean(Sensor_Matrix);
Avg_Ref = mean(Ref_Matrix);

% Plot the results of the run averaging routines to verify that it is not
% distorted.
figure(1)
subplot(211)
plot(Avg_Sensor)
subplot(212)
plot(Avg_Ref)

% Save the run averaged data in a .mat file, appending the original file
% name with _Avg to denote the relationships between the files.
NewFileName = [Filename,'_Avg'];
save(NewFileName,'Avg_Sensor','Avg_Ref','Ts','numRuns')
```

Plant Identification Code

```
%%%!!!!!!!!!!!!!!!!!!!!!!!!!!!!!!!!!!!!!!!!!!!!!!!!!!!!!!!!!!!!!!!!!!!!!!!!!!
%%% Identification of the plant using pem and its' continuous process model
%%% option.
%%%!!!!!!!!!!!!!!!!!!!!!!!!!!!!!!!!!!!!!!!!!!!!!!!!!!!!!!!!!!!!!!!!!!!!!!!!!!

% Load the run averaged data
load ContRun2d_Avg

% Create iddata structure
data = iddata(Avg_Sensor',Avg_Ref',Ts);

% Identifies the closed loop model and transforms it into a TF
Gcl_1 = pem(data,'P3U');
Gcl_1 = tf(Gcl_1);
Gcl_1 = Gcl_1(1)

% Find the numerator, denominator, and dc gain values of the closed loop TF
Gcl_gain = dcgain(Gcl_1);
Gcl_num = Gcl_1.num{1};
Gcl_den = Gcl_1.den{1};
```

```
% Simulate the closed loop system with the actual input
t = [0:length(Avg_Sensor)-1]*Ts;
ysim = lsim(Gcl_1,Avg_Ref,t);

% Define the "expected" controller transfer function blocks
Gc1 = tf([1 30.3],[1 2278.97]);
Gc2 = tf(182.55,[1 2278.97]);

% Using appropriate transformations, determine the numerator and
% denominator of the plant model
num = conv(Gcl_num,[1 2278.97]);
den1 = Gcl_den*182.55;
den2 = conv([1 30.3],Gcl_num);

% Add zeros to the front end of the shortest data vector so that den1 can
% be added to den2
dL = length(den1) - length(den2);
if dL > 0
    den2 = [zeros(1,dL), den2];
elseif dL < 0
    den1 = [zeros(1,-dL),den1];
end
den = den1 + den2;

% Create the expected plant transfer function
Gp_1 = tf(num,den);
Gp_1 = minreal(Gp_1)

% WE are not expecting any zeros in the plant model so they will be taken
% out while keeping the same dc gain. The zero would most likely have been
% canceled out in the algebraic manipulation if we had identified the 4th
% pole.
den = Gp_1.den{1};
num = Gp_1.num{1};
Gp_2 = tf(num(end),den);
zpk(Gp_2)

%Using the estimated plant model and the controller models to resolve for
%the closed loop model
```

```
Gcl_2 = minreal(series(Gc2,feedback(Gp_2,Gc1,+1)))

% Simulate using this closed loop model to verify the solution found for
% the plant.
ysim2 = lsim(Gcl_2,Avg_Ref,t);
```

Symbolic Solution for the Designed System's Plant Model Operating in Attractive Mode

```
%%%!!!!!!!!!!!!!!!!!!!!!!!!!!!!!!!!!!!!!!!!!!!!!!!!!!!!!!!!!!!!!!!!
%%% Symbolically determine the theoretical model of the
%%% Hall Sensor System Operating in the Attractive Mode
%%%!!!!!!!!!!!!!!!!!!!!!!!!!!!!!!!!!!!!!!!!!!!!!!!!!!!!!!!!!!!!!!!!
syms x1 x2 x3 M g a Lo Li Rl N c k Vl u s

f1 = x2;
f2 = g -(x3*k)/(M*(a+x1)^N) - c*x2/M;
f3 = ((a + x1)/(Li*(a + x1) + a*Lo))*(Vl*u - x3*Rl + ((a*Lo*x2*x3)/(a+x1)^2));

a11 = diff(f1,x1)
a12 = diff(f1,x2)
a13 = diff(f1,x3)

a21 = diff(f2,x1);
display('a21␣=')
pretty(a21)

a22 = diff(f2,x2)
a23 = diff(f2,x3);
display('a23␣=')
pretty(a23)

a31 = diff(f3,x1);
a31 = subs(a31,x2,0);
display('a31␣=')
pretty(a31)

a32 = diff(f3,x2);
```

```
display('a32 =')
pretty(a32)

a33 = diff(f3,x3);
a33 = subs(a33,x2,0);
display('a33 =')
pretty(a33)

b1 = diff(f1,u);
b2 = diff(f2,u);
b3 = diff(f3,u);
b3 = subs(b3,x2,0);

A  =[a11 a12 a13; a21 a22 a23; 0 a32 a33];
B = [b1;b2;b3];
C = [1 0 0];

TF = C*inv(s*eye(3)-A)*B;
TF = simple(TF);
TF = collect(TF,s);

[num,den] = numden(TF);

den = collect(den,s);
den = fliplr(coeffs(den,s));
num = num/den(1);
num = simplify(num);
den = den./den(1);
den = simplify(den);

%%%%%%%%%%%%%%%%%%%%%%%%%%%%%%%%%%%% Numerator
display(' Numerator: ')
pretty(num)

%%%%%%%%%%%%%%%%%%%%%%%%%%%%%%%%%%%% s^3 term
display(' s^3 term: ')
pretty(den(1))

%%%%%%%%%%%%%%%%%%%%%%%%%%%%%%%%%%%% s^2 term
display(' s^2 term: ')
```

```
s2term = simple(collect(den(2),c));
pretty(s2term)

%%%%%%%%%%%%%%%%%%%%%%%%%%%%%%%%%%%% s^1 term
display(' s^1 term: ')
[nums1,dens1] = numden(den(3));
s1coeffs = coeffs(nums1,x3);
s1p1 = simple(s1coeffs(1)/dens1);
display(' s1 part1: ')
pretty(s1p1)
s1p2num = simple(s1coeffs(2)*(a + x1)^N); % Factoring out (a+x1)^N
s1p2 = simple(s1p2num/dens1);
s1p2 = collect(s1p2,N);
% Multiply the s1p2 term by x3/((a+x1)^N) to get the correct answer
s1p2 = s1p2*(x3/(a + x1)^N);
display(' s1 part2 : ')
pretty(s1p2)

%%%%%%%%%%%%%%%%%%%%%%%%%%%%%%%%%%%% s^0 term
display(' s^0 term: ')
pretty(den(4))
```

Bibliography

[1] B. Jayawant, "Electromagnetic suspension and levitation," *Physical Science, Measurement and Instrumentation, Management and Education - Reviews, IEE Proceedings A*, vol. 129, pp. 549–581, Nov. 1982.

[2] S. Earnshaw, "On the nature of the molecular forces which regulate the constitution of the luminiferous ether," *Trans. Camb. Phil. Soc.*, vol. 7, pp. 97–112, 1839.

[3] G. Marsden, "Levitation!," *Nuts and Volts Magazine*, vol. 24, p. 5861, Sept. 2003.

[4] E. Bachelet, "Levitating transmitting apparatus." U.S. Patent, 1912. Patent #: 1,020,942.

[5] E. Bachelet, "Emile Bachelet Collection, 1880s-1973." Smithsonian Institution Research Information System (SIRIS).

[6] G. Richards, "Magnetism on a roll," *Engineering Technology*, vol. 5, pp. 36–39, March 2010.

[7] P. Budig, "Magnetic bearings and some new applications," in *Electrical Machines (ICEM), 2010 XIX International Conference on*, pp. 1–7, Sept. 2010.

[8] Y. Guan, S. Liu, H. Li, Y. Fan, and Y. Zhang, "Study on magnetic bearings system in axial-flow blood pump," in *Mechanic Automation and Control Engineering (MACE), 2010 International Conference on*, pp. 3903–3907, June 2010.

[9] B. Jayawant, P. Sinha, A. Wheeler, R. Whorlow, and J. Willsher, "Development of 1-ton magnetically suspended vehicle using controlled d.c. electromagnets," *Electrical Engineers, Proceedings of the Institution of*, vol. 123, pp. 941–948, Sept. 1976.

[10] M. Goodyer, R. Henderson, and M. Judd, "The measurement of magnus force and moment using a magnetically suspended wind tunnel model," *Magnetics, IEEE Transactions on*, vol. 11, pp. 1514–1516, Sept. 1975.

[11] L. Guang, Z. Yu, Z. Ming, D. Guanghong, and M. Tomizuka, "Six-DOF maglev nano precision microstage development," in *Mechanic Automation and Control Engineering (MACE), 2010 International Conference on*, pp. 938–941, June 2010.

[12] S.-Y. Hsieh, C.-H. Jou, M.-Y. Chen, S.-C. Huang, C.-H. Lin, and L.-C. Fu, "Implementation of a 6-dof precision positioning platform for a injection molded part," in *Industrial Electronics Society, 2007. IECON 2007. 33rd Annual Conference of the IEEE*, pp. 2922–2927, Nov. 2007.

[13] B. Jayawant and D. Rea, "New electromagnetic suspension and its stabilisation," *Electrical Engineers, Proceedings of the Institution of*, vol. 115, pp. 549–554, April 1968.

[14] B. Jayawant, R. Whorlow, and B. Dawson, "New transducerless magnetic suspension system," *Science, Measurement and Technology, IEE Proceedings*, vol. 142, pp. 255–261, May 1995.

[15] W. Hurley and W. Wolfle, "Electromagnetic design of a magnetic suspension system," *Education, IEEE Transactions on*, vol. 40, pp. 124–130, May 1997.

[16] W. Hurley, M. Hynes, and W. Wolfle, "PWM control of a magnetic suspension system," *Education, IEEE Transactions on*, vol. 47, pp. 165–173, May 2004.

[17] J. Tsui, D. Iden, K. Strnat, and A. Evers, "The effect of intrinsic magnetic properties on permanent magnet repulsion," *Magnetics, IEEE Transactions on*, vol. 8, pp. 188–194, June 1972.

[18] P. Berkelman and M. Dzadovsky, "Single magnet levitation by repulsion using a planar coil array," in *Control Applications, 2008. CCA 2008. IEEE International Conference on*, pp. 108–113, Sept. 2008.

[19] P. Berkelman and M. Dzadovsky, "Novel design, characterization, and control method for large motion range magnetic levitation," *Magnetics Letters, IEEE*, vol. 1, Jan. 2010.

[20] T. H. Wong, "Design of a magnetic levitation control system an undergraduate project," *Education, IEEE Transactions on*, vol. E-29, Nov. 1986.

[21] J. Watkins and G. Piper, "An undergraduate course in active magnetic levitation: bridging the gap," in *System Theory, 2003. Proceedings of the 35th Southeastern Symposium on*, pp. 313–316, March 2003.

[22] K. Lilienkamp, "Low-cost magnetic levitation project kits for teaching feedback system design," in *American Control Conference, 2004. Proceedings of the 2004*, vol. 2, pp. 1308–1313, July 2004.

[23] K. Lundberg, K. Lilienkamp, and G. Marsden, "Low-cost magnetic levitation project kits," *Control Systems, IEEE*, vol. 24, pp. 65–69, Oct. 2004.

[24] J. Balchen, M. Handlykken, and A. Tysso, "The need for better laboratory experiments in control engineering education," *Computer Control Experiments in Education*, pp. 3363–3368,3381, 1981.

[25] ECP, "ECP Systems - Educational Control Products," *http://www.ecpsystems.com*, 2007.

[26] B. Hansen, "Levitation by LNS Technologies - Introduction," *http://www.coilgun.info/lev_lns/home.htm*, 2008.

[27] B. Hansen, "Levitation by LNS Technologies - LNS Schematic," *http://www.coilgun.info/lev_lns/schematic.htm*, 2008.

[28] H. Woodson and J. Melcher, *Electromechanical Dynamics*, vol. 1. Wiley, 1968.

[29] J. Sha, R. Cosgriff, and M. Hollander, "EE350H final report," Dec. 2007.

[30] J. Hoagg and D. Bernstein, "Nonminimum-phase zeros much to do about nothing," *IEEE Contr. Sys. Mag.*, June 2007.

[31] J. Fruedenberg and D. Looze, "Right half plane poles and zeros and design tradeoffs in feedback systems," *Automatic Control, IEEE Transactions on*, vol. AC-30, June 1985.

[32] D. Looze and J. Fruedenberg, "Limitations of feedback properties imposed by open-loop right half plane poles," *Automatic Control, IEEE Transactions on*, vol. 36, June 1991.

[33] L. Qiu and E. Davison, "Performance limitations of non-minimum phase systems in the servomechanism problem," *Automatica*, vol. 29, 1993.